

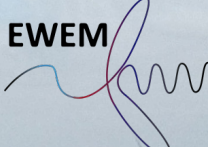
Auralisation of Modelled Wind Turbine Noise for Psychoacoustic Listening Experiments

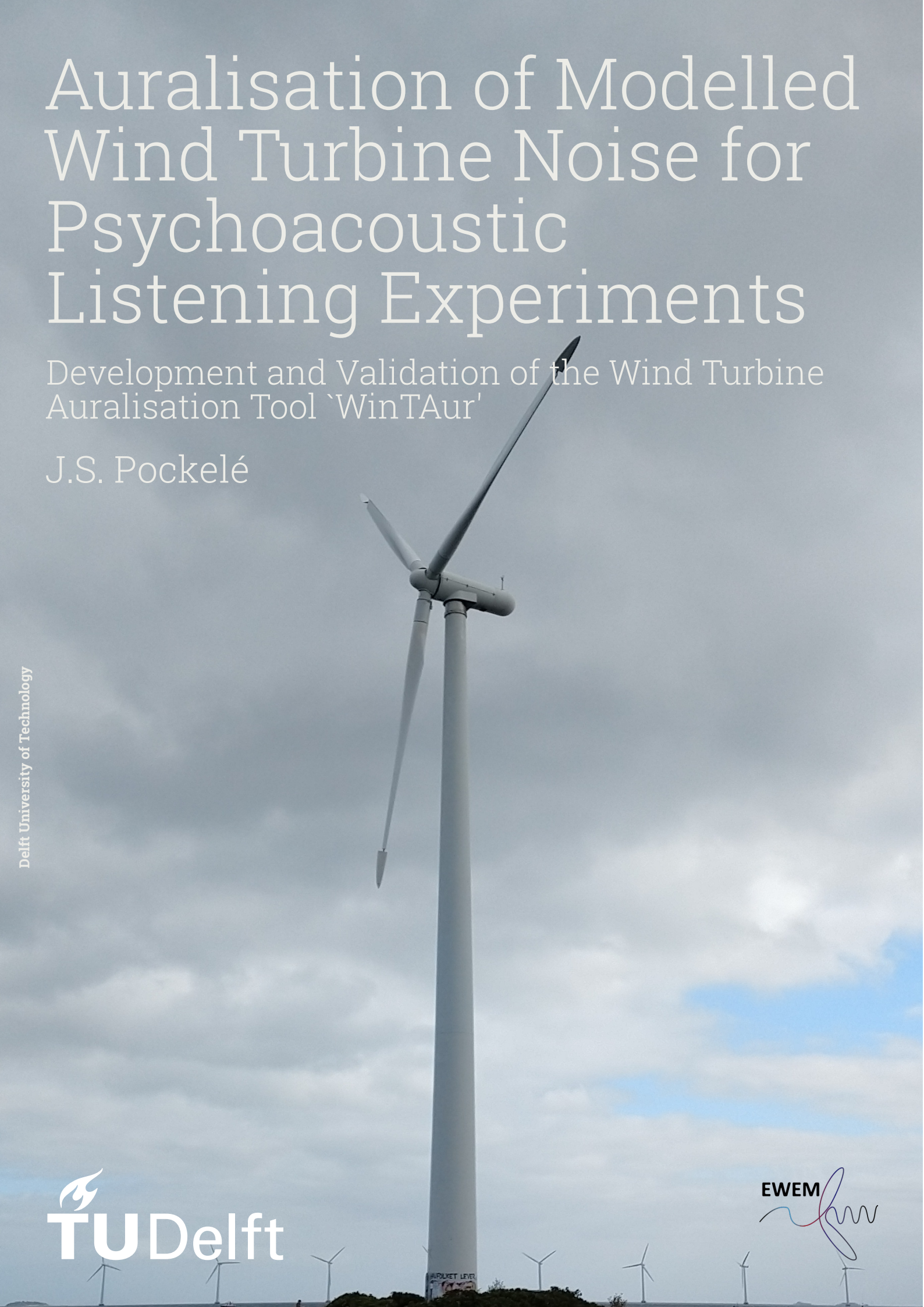
Development and Validation of the Wind Turbine
Auralisation Tool 'WinTAur'

J.S. Pockelé

Delft University of Technology


TU Delft

EWEM




Auralisation of Modelled Wind Turbine Noise for Psychoacoustic Listening Experiments

Development and Validation of the Wind Turbine
Auralisation Tool 'WinTAur'

by

Josephine Siebert Pockelé

October 22, 2023

to obtain the degree of Master of Science in Aerospace Engineering at Delft University of Technology,
and Master of Science in Engineering (European Wind Energy) at the Technical University of Denmark,
to be defended publicly on Wednesday, November 8, 2023 at 13:00.

Daily Supervisor:	Dr. R. Merino-Martínez	Assistant Professor, TU Delft
Co-Supervisors:	Dr. F. Bertagnolio	Senior Researcher, DTU
	Dr. A. W. Fischer	Senior Researcher, DTU
Committee Chair:	Dr. D. Ragni	Associate Professor, TU Delft
Examiner:	Dr.-Ing. R. Schmehl	Associate Professor, TU Delft

Cover: Wind turbine in the Lynetten wind farm, Copenhagen, Denmark.
Style: Modified version of Daan Zwaneveld's TU Delft Report Style.

An electronic version of this thesis is available at: <http://repository.tudelft.nl/>.



Preface

This thesis, “*Auralisation of modelled wind turbine noise for psychoacoustic listening experiments*”, concludes my time in the European Wind Energy master and as a university student. This work combined my interests in wind energy and engineering acoustics to investigate a new methodology for generating wind turbine noise signals for psychoacoustic experiments. During this project, I implemented a fully modelled auralisation toolchain. This research report targets readers interested in the socio-technical investigation of wind turbine noise. I hope that this project sparks efforts to understand better and communicate about the noise of future wind farm projects.

I want to include the following quote from NASA astronaut Sally Ride, which perfectly encapsulates my love for science, which drives my continuous enjoyment of my studies and further research endeavours:

“Science is fun. Science is curiosity. We all have natural curiosity. Science is a process of investigating. It’s posing questions and coming up with a method. It’s delving in.”

This project has been really enjoyable to execute, and kept piquing my curiosity every step of the way. It truly made me wish I could keep adding analyses and implementing more numerical models. It is with great pleasure that I will continue this work into a four-year PhD.

I want to thank my supervision team for assisting me in delivering the best work I could produce. In particular, I want to thank my daily supervisor, Roberto Merino-Martinez, for his unwavering support and endless encouragement throughout the project. He was instrumental in setting up the listening experiment and in providing me with valuable feedback during our weekly meetings. His attitude and passion have continuously fuelled my enjoyment of academic research. I also want to thank my DTU co-supervisors, Franck Bertagnolio and Andreas Fischer, for assisting me with setting up the validation and helping me understand *HAWC2* so I could get this project on rails. And lastly, I want to thank Daniele Ragni for his great feedback and insights at all project stages.

I also want to take time to thank my friends and family. Starting with Benno Riha for the fun Mondays working together at the faculty. His endless humour and sarcasm made me look forward to every visit to Delft and made coffee breaks much more enjoyable. A great thanks also goes to Kimberly van den Bogaard for the lengthy late-night calls where she supported and encouraged me through my hard times. The funny reels she sent were always well-timed to cheer me up and get me going again. My brothers, Ewout and Jorben, made me feel right back at home in Belgium. I thank them both for allowing me the enjoyment of annoying them from time to time. Our mutual venting about our days provided great relief after a stressful day.

This research would not have been feasible if it weren’t for these people, and I am endlessly grateful for their contributions.

I hope you enjoy reading this thesis as much as I enjoyed writing it.

Josephine Siebert Pockelē
Antwerpen, October 2023

Summary

Wind turbine noise is one of the grand challenges in the public acceptance of onshore wind farm projects. The field of psychoacoustics identifies the auralisation of wind turbine noise as a link between technical design and annoyance estimation. There is currently limited work on the auralisation of wind turbine noise, and none targets an application in psychoacoustic research.

This work investigates the auralisation of the aeroacoustics output of DTU's HAWC2 for use in annoyance estimation. A Gaussian beam tracing approach propagates the frequency domain output to observer locations. The resulting spectrograms are converted into sound signals by applying random phase and the inverse short-time Fourier transform. This work includes a binaural rendering module to enable future VR applications. The methodology's implementation results in the Wind Turbine Auralisation tool, WinTAur.

The noise signal output of WinTAur is validated using the HAWC2 model of a stall-controlled NTK 500/41 wind turbine and corresponding acoustic field measurements. Psychoacoustic sound quality metrics show significant differences between the auralised and measured noise. In the overall psychoacoustic annoyance metric, these differences mainly depend on the observer's position around the turbine. All metrics show this directionality dependence, while the loudness, sharpness and tonality metrics also indicate a dependence on wind speed. Differences in fluctuation strength show a minor dependence on the simulation case but are difficult to relate to a specific simulation parameter.

Spectral analysis of the simulation output samples reflects the limitations of HAWC2, demonstrating that it is the primary source of discrepancy. The analysis especially highlights the inaccurate prediction of the directionality and stall noise of the HAWC2 code. The choice of ground type is another probable source of discrepancy, as it does not accurately represent the measurement setup.

A subjective listening experiment demonstrates the significance of these discrepancies in human perception with generally high difference ratings between the simulated and recorded noise. The results illustrate a dependence on wind speed and the position around the turbine. These dependencies match well with the findings from the numerical validation.

Future work should focus on a sensitivity analysis of WinTAur since the case-independent parameters may be additional sources of discrepancy. Another recommendation is to investigate the unveiled errors in the underlying methodology. Lastly, better propagation modelling concerning the wind turbine wake and turbulence should be part of future wind turbine noise modelling.

Overall, using modelled wind turbine noise for the auralisation in psychoacoustic research has shown promising results. Validation with sound quality metrics provides good insights into the discrepancies found in subjective listening experiments. Eliminating the existing discrepancies through modelling improvements will allow this work to be applied in a fully modelled approach to estimate wind turbine noise annoyance.

Contents

Preface	iii
Summary	v
Nomenclature	xii
1 Introduction	1
2 Wind Turbine Noise Auralisation	3
2.1 Aerodynamic Noise Generation	3
2.2 Physics of Outdoor Sound Propagation	6
2.3 Signal Processing	8
2.4 Current Auralisation Methods	8
3 Source Model	11
3.1 HAWC2 Aeroacoustics Model	11
3.2 Sound Source Model	12
4 Propagation Model	17
4.1 Existing Numerical Methods	17
4.2 Beam Tracing Methodology	18
5 Binaural Rendering	25
5.1 Head-Related Transfer Functions	25
5.2 Interaural Time Difference	26
5.3 Methodology	27
6 Sound Reception and Signal Reconstruction	29
6.1 Phase Reconstruction Methods	29
6.2 Reconstruction Methodology	34
7 Implementation of WinTAur	37
7.1 Software Implementation	37
7.2 Verification	41
8 Numerical Validation	43
8.1 Case Study Setup	43
8.2 Sound Quality Assessment	46
8.3 Spectral Analysis	52
9 Listening Experiment	57
9.1 Test Setup	57
9.2 Participant Statistics	61
9.3 Experiment Results	63
10 Conclusion and Future Work	67
A Coordinate Systems	I
B Validation Data	III
C Numerical Validation PBL Plots	VII
References	XVII

Nomenclature

Abbreviations

BPF	Blade Pass Frequency
BPM	Airfoil self-noise model by Brooks, Pope and Marcolini
CAA	Computational Acoustic Analogy
CFD	Computational Fluid Dynamics
DNS	Direct Numerical Simulation
FFT	Fast Fourier Transform
FGLA	Fast Griffin and Lim Algorithm
GLA	Griffin and Lim Algorithm
HATS	Head And Torso Simulator
HAWC2	Horizontal Axis Wind turbine simulation Code 2nd generation
HRIR	Head-Related Impulse Response
HRTF	Head-Related Transfer Function
ISA	ISO Standard Atmosphere
ISO	International Organisation for Standardisation
iSTFT	Inverse Short-Time Fourier Transform
ITD	Interaural Time Difference
JND	Just Noticeable Difference
KEMAR	Knowles Electronics Manikin for Acoustic Research
LES	Large Eddy Simulation
NACA	National Advisory Committee for Aeronautics
PBL	Pressure Band Level
PGHI	Phase Gradient Heap Integration Algorithm
PSL	Pressure Spectral Level
RPM	Rotations Per Minute
RTISI	Real-Time Iterative Spectrogram Inversion
RTISI-LA	Real-Time Iterative Spectrogram Inversion with Look-Ahead
RTPGHI	Real-Time Phase Gradient Heap Integration Algorithm
SNR	Signal-To-Noise Ratio
STFT	Short-Time Fourier Transform

TI	Turbulence Intensity
WD	Wind Direction
WS	Wind Speed

Constants

γ	Heat capacity ratio of air at $20^{\circ}C$	1.4 [-]
j	Imaginary unit	$j^2 = -1$
p_{s0}	Reference atmospheric pressure	101,325 Pa
R_0	Specific gas constant of air	287 J/(kg K)
T_0	Reference atmospheric temperature	293.15 K
T_{01}	Triple-point isotherm temperature	273.16 K

Symbols

α	Atmospheric absorption coefficient	Np/m
α_g	Acceleration parameter in FGLA	
$\bar{\alpha}$	Logarithmic atmospheric absorption coefficient	dB
Δt	Time step	s
δ	Small difference	
$\delta\alpha$	Angular inter-ray distance	rad
ϵ	Width parameter of Gaussian beam method	
∇	Determinant of the intersection between a line and a sphere	m
ω	Angular frequency	rad/s
ϕ	Polar of spherical coordinates	rad
ϕ_d	Polar angle of Deserno algorithm	rad
$\phi_{f,t}$	Spectrogram of sound phase	rad / Hz
ψ	Azimuth in cylindrical coordinates	rad
$\rho_{x,y}$	Pearson correlation coefficient of variables x and y	
σ_e	Flow resistivity factor	[-]
θ	Azimuth of spherical coordinates	rad
θ_0	Azimuth offset of head-related spherical coordinates	rad
θ_d	Azimuth angle of Deserno algorithm	rad
$\theta_{grazing}$	Ground grazing angle	rad
a_d	Fractional area per ray on unit sphere	m^2
A_f	Amplitude of the Discrete Fourier Transform	Pa/Hz
$A_{f,t}$	Spectrogram of sound pressure amplitude	Pa/Hz
c	Speed of sound	m/s

d	Distance	m
d_d	Approximate inter-ray distance on unit sphere	m
$d_{azimuth}$	Inter-ray distance on azimuth circle	m
d_{polar}	Inter-ray distance on polar circle	m
f	Frequency	Hz
f_c	Octave band central frequency	Hz
f_l	Octave band lower frequency	Hz
F_s	Spherical wave correction factor	[-]
f_s	Sampling frequency	Hz
f_u	Octave band upper frequency	Hz
$f_{r,N}$	Gas resonance frequency of Nitrogen	Hz
$f_{r,O}$	Gas resonance frequency of Oxygen	Hz
H	Absolute humidity	%
h	Relative humidity	%
i	Indexing number	
k	Wave number	1/m
$M_{azimuth}$	Number of rays in azimuth circle	[-]
M_{polar}	Number of rays in polar circle	[-]
N	Number of discrete points	
n	Distance normal to sound ray	m
N_{ray}	Number of emitted rays	[-]
o	Discrete Fourier transform overlap parameter	
p_s	Atmospheric pressure	Pa
$P_{f,t}$	Spectrogram of sound pressure spectral densities	Pa ² /Hz
P_f	Spectrum of sound pressure spectral densities	Pa ² /Hz
p_{sat}	Water vapour saturation pressure	Pa
Q	Ground reflection coefficient	[-]
R	Turbine rotor radius	m
r	Radius	m
r_2	Radial distance of ground reflection	m
R_p	Wave reflection coefficient	[-]
S	Gaussian beam cross-sectional area	m ²
s	Distance along the ray path	m
s_0	Initial ray path length	m

s_w	Discrete Fourier transform window scaling factor	
T	Temperature	K
t	Time	s
v	Value of arbitrary parameter	
W	Discrete Fourier transform window	
w	Numerical distance for ground reflections	[-]
X_f	Discrete Fourier Transform	Pa/Hz
$X_{f,t}$	Short-Time Fourier Transform	Pa/Hz
Z	Sound impedance coefficient	[-]
z	Coordinate in Cartesian z-axis	m
z_0	Wind profile roughness height	m
z_{ref}	Wind profile reference height	m
Att	Sound attenuation level	dB
FS	Psychoacoustic fluctuation strength metric	vacil
K	Psychoacoustic tonality metric	t.u.
N	Psychoacoustic loudness metric	sone
PA	Psychoacoustic annoyance metric	
PBL	Pressure band level in one-third octave bands	dB
PSL	Pressure spectral level	dB/Hz
R	Psychoacoustic roughness metric	asper
S	Psychoacoustic sharpness metric	acum

Vector Symbols

$\vec{\nabla}$	Differential operator	
$\vec{\xi}$	Sound source position	
$\vec{\zeta}$	Sound receiver position	
\vec{B}	Cylindrical coordinate	
\vec{C}	Cartesian coordinate	
\vec{H}	Head-Related Spherical coordinate	
\vec{N}	Wavefront normal velocity	
\vec{n}	Normal vector defining a plane	
\vec{O}	Origin point for non-Cartesian coordinate	
\vec{p}	Point defining a plane	
\vec{S}	Spherical coordinate	
\vec{U}	Wind speed vector	
\vec{V}	Ray velocity	
\vec{x}	Position	

1

Introduction

To meet 2030 climate and energy goals, large amounts of wind turbines are being installed yearly. While the offshore wind energy sector is growing, onshore wind is still responsible for most of the growth in installed capacity [1], [2]. The biggest challenge facing the public acceptance of onshore wind turbine installations is noise [3]–[6]. While levels are typically lower than those of other sources of noise, such as aircraft [7], [8] or traffic noise [9], the number of annoyed people is found to be higher for similar exposure dosage [10]–[13]. While McCunney et al. [14] found no indications of health risks related to low-frequency sound, studies show a risk to sleep and cognitive performance caused by wind turbine noise [15]–[18].

In recent studies related to the annoyance and health risks of wind turbine noise, use is made of virtual reality setups [17], [19] or listening rooms [20], [21]. For these studies, sound obtained through recordings is used and sometimes combined with an auralisation toolchain. Despite the clear results of these studies, there are indications of specific situations where annoyance and health risks are higher [22]. Bolders Reedijk and Kamp [18] further indicate that their study regarding health risks is limited due to the limited number of people living close to wind turbines, highlighting the need for experiments in simulated settings. Public engagement regarding new wind farm projects using auralised wind turbine noise has been demonstrated by Butera et al. [23]. Their study shows a desire in the public for a more significant number of simulated situations. Public engagement regarding noise impact is shown to be very important in the acceptance of projects [22].

Kirkegaard et al. [24] indicate that a socio-technical lens is critical when solving the grand challenges of wind energy development. When it comes to noise, the field of psychoacoustics [25] provides such a socio-technical lens. Within psychoacoustics, there are indications that current parameters cannot explain differences in annoyance [26]. In an attempt to alleviate this limitation, Merino-Martinez et al. [20] propose the framework in Figure 1.1, which involves auralisation to allow for the modelling of turbine noise annoyance.

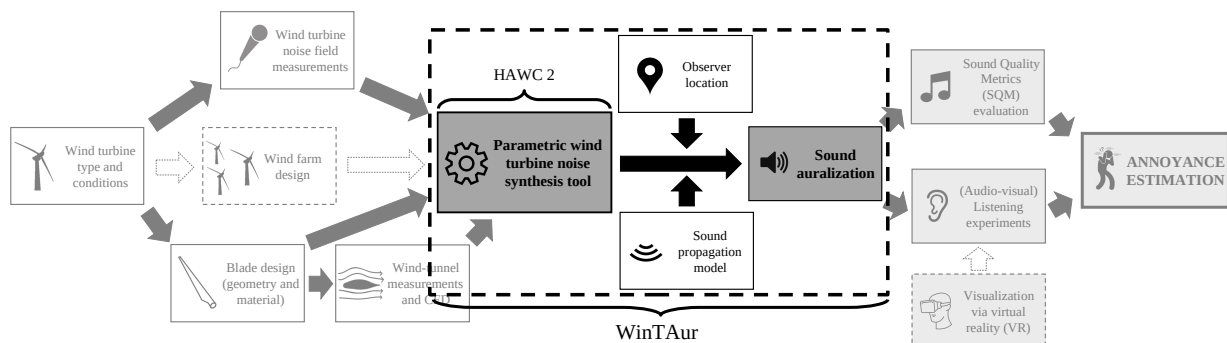


Figure 1.1: Concept framework for the estimation of wind turbine noise annoyance. The Wind Turbine Auralisation tool from this thesis (WinTAur) is highlighted. (Adapted from Merino-Martinez, Pieren and Schäffer [3, Fig. 1].)

The above information identifies a need for an auralisation tool for wind turbine noise. These tools exist [27]–[29], but are targeted at different fields of application and levels of fidelity. They implement their own noise source modelling, while there are wind turbine simulation codes with aeroacoustic modules available, such as SILANT [30], HAWC2 [31], and openFAST [32].

Considering all the above, the research objective statement for this work is formulated:

The objective of this Master Thesis is to investigate the use of the aeroacoustics module of HAWC2 in the auralisation of wind turbine noise. Specifically, this work focuses on auralisation for applications in psychoacoustics. This work aims to implement a fully modelled approach to close the wind turbine noise annoyance estimation framework.

This work's specific place in estimating wind turbine noise annoyance is highlighted in Figure 1.1. Within the research objective, the following additional questions are posed:

1. *What sources of discrepancy exist between the auralised wind turbine noise and experimental recordings?*
2. *In terms of psychoacoustic sound quality metrics, how large are the discrepancies between the auralised wind turbine noise and experimental recordings?*
3. *Which trends in the numerical discrepancies between auralised wind turbine noise and experimental recordings are reflected in subjective perception?*

Chapter 2 first covers essential topics in the field of wind turbine noise, which forms the basis of this work. Then, chapters 3, 4, 5 and 6 cover both literature and the chosen methodologies for the different parts of the auralisation toolchain. Chapter 7 discusses the overall implementation of these methodologies into one coherent code. This code is then validated numerically in chapter 8 and through a subjective listening experiment in chapter 9.

2

Wind Turbine Noise Auralisation

Vorländer [33, p. 100] defines auralisation as “the technique to create audible sound files from numerical (simulated, measured, synthesised) data.” The principle steps involved in auralisation are shown in Figure 2.1. Three distinct parts are present: sound generation, transmission or propagation, and processing and reproduction. Sound generation describes the sound emitted by either a sound power and directivity of extended or distributed sources, a blocked force output, or the free velocity of a vibrating source. The propagation contains all elements that describe the path from source to observer and how this path affects the source input. Lastly, processing and reproduction is the step where the received signal is made into a sound file that can be played to a listener.

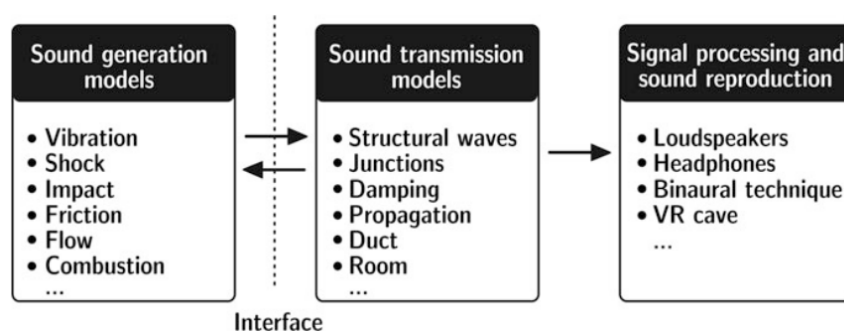


Figure 2.1: “Principle of auralization” [33, Fig. 7.1]

The physics behind the first two steps, when applied to wind turbine noise, are explored in this chapter. The noise generation is described in section 2.1 and the propagation in section 2.2. The signal processing methods used in this report are covered in section 2.3, so results may be more easily reproduced. Lastly, existing methods of auralising wind turbine noise are reported in section 2.4 to illustrate the current state-of-the-art.

2.1. Aerodynamic Noise Generation

Glegg and Devenport [34, p. 5] describe the underlying phenomenon causing aerodynamic noise as follows: “When convected turbulence encounters a solid body, it generates rapid changes of pressure on the surface of the body that radiate as sound waves through the fluid.” The flow phenomena over a wind turbine blade, relevant to aerodynamic noise generation, are illustrated in Figure 2.2.

Since the shape of wind turbine blades is dominated by airfoils, the mechanisms of aerodynamic noise are all related to airfoil self-noise. Bertagnolio and Fischer [35] further describe that the complexity of the turbulent flow around wind turbines makes the prediction of these phenomena quite tricky. Nonetheless, the dominant airfoil self-noise mechanisms relevant to wind turbines are clearly defined. The four most relevant mechanisms and the current state of their prediction methods are summarised in this section, after the work by Brooks, Pope and Marcolini [36], and by Bertagnolio and Fischer [35].

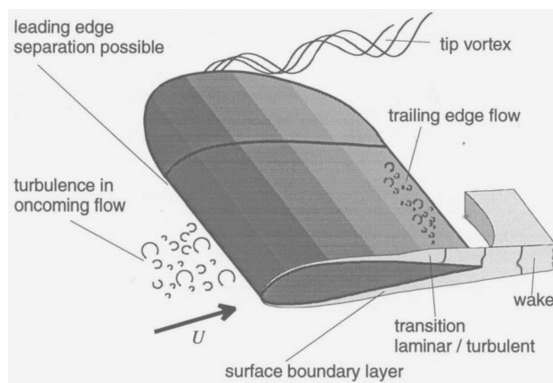


Figure 2.2: "Schematic of the flow around the outer part of the rotor blade" [37, Fig. 4.4].

2.1.1. Turbulent Inflow Noise

The first self-noise mechanism relevant to the turbulent flow around wind turbine blades is turbulent inflow noise. This noise source is evident when considering the above quote from Glegg and Devenport [34, p. 5]. The noise from this mechanism is caused by the impingement of a turbulent flow on an airfoil, which generates pressure fluctuations on the leading edge.

The analysis of this noise source is mainly inherited from the study of propeller and helicopter blade noise. The work by Amiet [38], which uses the Schwarzschild technique to solve the Helmholtz wave equation, is widely used as a prediction tool in the wind turbine industry and research communities, as it is heavily validated against experimental data. This theory has a few limitations, as it assumes the airfoil is a flat plate with zero angle of attack in turbulence described by the isotropic Von Kármán spectrum [39]. However, Bertagnolio, Madsen and Fischer [31] did not find substantial discrepancies when using Mann's model [40] for turbulence. Discrepancies between the model and measurements are driven by angle of attack [41] and airfoil leading edge thickness [42]. Moriarty, Guidati and Migliore [43] have developed empirical corrections for thick leading edges.

2.1.2. Turbulent Boundary Layer Trailing Edge Noise

The interaction of the top and bottom turbulent boundary layers with the airfoil's trailing edge is the basis for the second source of self-noise: turbulent boundary layer trailing edge noise. The physical mechanism is the sound emissions of turbulent eddies, amplified by scattering effects at the airfoil's trailing edge. This source is most dominant close to the blade's tip, as the inflow velocity and turbulence intensity are the largest. It is currently the dominant noise source in the audible range, enhancing its importance in analysing wind turbine noise.

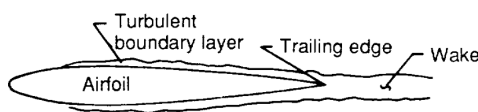


Figure 2.3: Aerodynamic flow responsible for turbulent trailing edge noise.
Adapted from Brooks, Pope and Marcolini [36, Fig. 1]

Due to its importance, many models exist for turbulent trailing edge noise prediction. Chase [44] proposes the first framework, which relates the surface pressure spectrum to the far field sound radiation through experimental results. Chandiramani [45] further developed this model, which Howe [46] then generalised. Amiet [47] proposes a similar model, which Roger and Moreau have improved [48], [49]. These models require expensive experimental pressure fluctuation measurements to predict trailing edge noise. Henceforth, Parchen [50] proposed a method to close the modelling loop, now known as the TNO model. The latter method related the pressure field to the velocity profile in the boundary layer through the work by Kraichnan [51], where the boundary layer could be simulated in XFOIL [52]. Kamruzzaman [53], and Fischer, Bertagnolio and Madsen [54] have made further developments of the TNO model as well. Similar to

Kamruzzaman, Goody [55], Rozenberg [56] and Lee [57] have also developed models for the wall pressure spectra, based on boundary layer parameters, which can be used in the Amiet or Chase models.

Brooks, Pope and Marcolini take a second modelling approach [36], now known as the BPM model. It is based on experimental work with a symmetric NACA 0012 airfoil at Reynolds numbers up to 1.5×10^6 . Noise emissions are related to the Reynolds number and the airfoil's angle of attack. An important parameter of the BPM model is the trailing edge boundary layer thickness, originally obtained from experiments on the NACA 0012 airfoil. Moriarty, Guidati and Migliore [42] generalised the BPM model by introducing the boundary layer thickness as a modelling parameter, which in turn can be modelled with tools like XFOIL [52].

Recent developments in computational capabilities have enabled the use of Direct Numerical Simulations (DNS) for predicting trailing edge noise. Sandberg, Sandham and Jones [58]–[60] conducted DNS computations of a flat plate, NACA 0006 and NACA 0012 airfoils at Reynolds number in the order of 10^4 to 10^5 . These low Reynolds numbers pose the current limitation of DNS due to the computational demands of higher Reynolds numbers. Since the Reynolds number close to the tip of a wind turbine blade is multiple orders of magnitude larger and due to its computational cost, DNS is not yet widely adopted in industry. Wang and Moin [61], and Wolf and Lele [62] have illustrated Large Eddy Simulations (LES) in combination with acoustic analogies. These studies are limited to Reynolds numbers in the order 4×10^5 .

On modern turbines, trailing edge serrations are frequently applied to minimise the turbulent noise close to the tip. Accurate attenuation prediction is currently only possible with high-fidelity CFD/CAA (Computational Fluid Dynamics, combined with Computational Acoustic Analogies) methods, limiting industrial noise analysis applications. Howe [63], and Lyu, Azarpeyvand and Sinayoko [64] have proposed analytical engineering models of noise attenuation by serrations. A recent development in reducing trailing edge noise is porous trailing edges [65], [66]. This technology and its associated numerical prediction methods are in the early stages of development and adaptation.

2.1.3. Separation and Stall Noise

Stall noise is an important source of airfoil noise at high angles of attack, as the flow over the airfoil is separated. Since the turbulent vortices in the separated flow region are large and convect slowly, stall noise is expected to generate low-frequency noise for dimensional reasons. According to measurements and modelling by Søndergaard [67] and Bertagnolio et al. [68], this is not necessarily true. Stall noise can be considered a combination of the previous two mechanisms, as it is dominated by large eddies interacting with the airfoil surface, combined with trailing edge scattering.

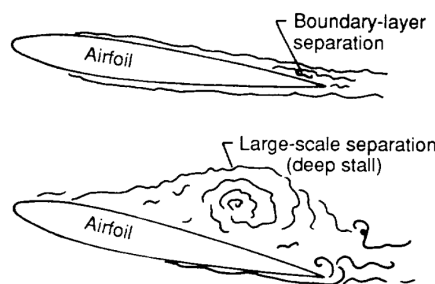


Figure 2.4: Aerodynamic flow responsible for separation and stall noise. Adapted from Brooks, Pope and Marcolini [36, Fig. 1]

There are two approaches in literature to predict stall noise over an airfoil. As a first approach, CFD/CAA methods have been attempted by Christophe, Anthoine and Moreau [69], Nagarajan, Hahn and Lele [70], and Kocheemoolayil, Wolf and Lele [71], but remain too computationally expensive for use in industry. The second approach consists of experiments in wind tunnels to determine the stall characteristics and associated noise. Brooks, Pope and Marcolini [36] considered stall noise during their experiments and derived a parametric model applicable to various airfoil profiles. Moreau, Roger and Christophe [72] derive a model from wind tunnel data of NACA 0012 and 65-1210 airfoils through the Curle acoustic analogy. Christophe, Anthoine and Moreau [69] further ran a wind tunnel campaign with a controlled diffusion airfoil to propose an LES-based model. Schuele and Rossignol [73], and Suryadi and Herr [74] propose a

model based on trailing edge theory, tuned for separated flow conditions. Bertagnolio and Fischer [68] propose a self-contained model based on Amiet's theory [47], scaled and fitted to data from wind tunnel and wind turbine measurement campaigns. The modelled prediction of stall noise heavily depends on the computational prediction of stall, which is a challenging task in itself. For this study, the modelling of stall noise can be considered the largest limiting factor in the final results.

2.1.4. Tip Noise

Large vortices are induced at the tip of a blade, which interact with the blade surfaces. This is the cause of the last relevant aerodynamic noise mechanism. The flow around a blade tip is very complex due to its three-dimensional nature, sharp velocity gradients, and the significant effect of the local blade geometry on the flow. The most accurate way to model this noise is thus by a CFD/CAA method, demonstrated by Arakawa et al. [75], and Schneider and Lucius [76]. Similar to the CFD-related methods above, tip noise prediction with CFD/CAA is limited in Reynolds number due to the computational cost. For industrial applications, engineering models, such as the one by George, Najjar and Kim [77], and the BPM model [36] with modifications by Moreau et al. [78] are widely applied.

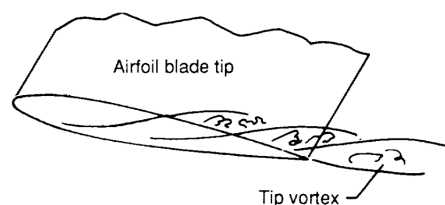


Figure 2.5: Aerodynamic flow responsible for tip noise. Adapted from Brooks, Pope and Marcolini [36, Fig. 1]

Outside of these four mechanisms, other airfoil self-noise mechanisms exist but are irrelevant for wind turbines due to the flow conditions on a blade. Blunt trailing edge noise may become more relevant with the emergence of flat back airfoils applied on the inboard section of large turbine blades for structural reasons [79]. Mechanical noise caused by the vibrations in the turbine structures and mechanics are usually dealt with by wind turbine designers by appropriate design and eigenfrequency analysis. These sources may become more relevant when rotor noise is reduced.

2.2. Physics of Outdoor Sound Propagation

The propagation of sound through the atmosphere is well described in literature. Typically, sound propagation is affected by the atmosphere, ground conditions, and obstacles. There are five phenomena at play when it comes to the effect on sound waves: reflection, absorption, refraction, diffraction and scattering. The different forms of these phenomena, as they occur in outdoor propagation, are illustrated in Figure 2.6 [80].

Reflections occur when sound waves encounter an acoustically solid boundary, such as the ground or obstacles, like buildings, vegetation, etc. The amount of energy that is reflected depends on the material and structure of the ground or obstacle and is measured by the acoustical impedance characterised by flow resistivity [81]. The energy that is not reflected is absorbed by the boundary. Sound reflections have been extensively studied and can be determined with models such as that of Embleton, Piercy and Daigle [81].

Two main absorption mechanisms occur in outdoor sound propagation: absorption at boundaries and absorption in the medium. In essence, sound waves are particles of a medium in cyclic motion. This motion, in turn, causes heat conduction, shear viscosity and molecular relaxation to occur, resulting in sound energy losses. The absorption at boundaries is usually covered by models of the reflection at such boundaries, as the two effects are intertwined. Empirical models of sound absorption in the atmosphere involve using the atmospheric conditions and models of the resonance frequencies of the most common elements in the atmosphere. Such a model of atmospheric losses is found in the work by Bass et al. [82], [83], which is integrated in the ISO 9613-1 standard [84].

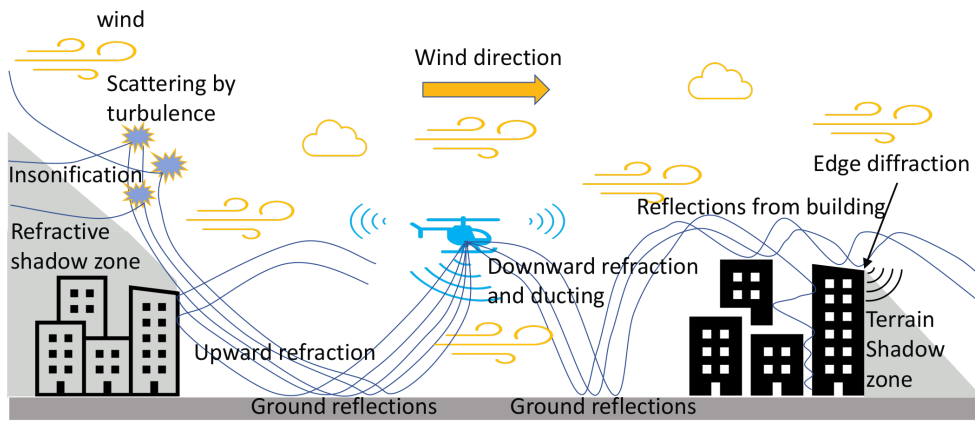


Figure 2.6: "An illustration of outdoor sound propagation." [85, Fig. 2.1]

Sound refraction is the deflection of the propagation path due to gradients in the properties of the medium. In the atmosphere, refraction is caused by gradients of wind speed and temperature [80], [86], which are well described in meteorological literature [87]. Depending on the nature of these gradients, sound can be refracted upwards or downwards, as illustrated in Figure 2.6. Refraction can also cause shadow zones and ducting in combination with topology and obstacles.

Diffraction is the spreading of waves away from the dominant propagation direction caused by the presence of acoustically sharp edges. In outdoor propagation, these edges occur at obstacles of which the characteristic length is comparable to or shorter than the sound wavelength. Diffraction can raise noise levels in the shadow zones [80].

When waves interact with local non-uniformities, the waves are deflected, which is a process called scattering. In the atmosphere, this scattering is usually caused by random fluctuations of wind speed and temperature in turbulence. Sound energy can be spread to shadow zones during scattering, which is called insonification. Usually, a loss of coherence in the propagated sound also occurs [85], [88].

One last phenomenon that occurs during the propagation of sound is the spreading of sound waves. This spreading causes the amplitude of the sound waves to decrease as energy is spread over a larger area. While often described as a loss, no energy is dissipated or lost to the environment in this process. Depending on the source's nature, the spreading pattern results in a specific sound attenuation, which is illustrated in Figure 2.7.

In this work; ground reflections, absorption, and refraction are accounted for, as well as spreading. Other effects are omitted as they either do not apply to the considered validation cases or their models are too complex for the scope of this thesis.

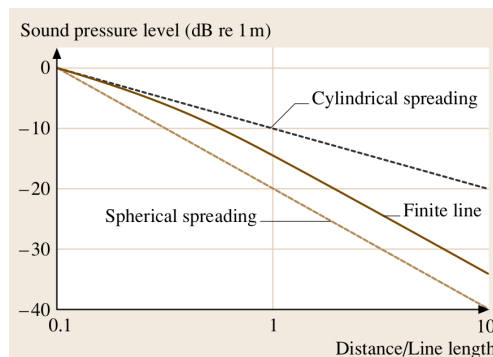


Figure 2.7: Spreading losses for point (spherical spreading), infinite line (cylindrical spreading) and finite line sources. [88, Fig. 4.1].

2.3. Signal Processing

This section establishes the conventions for signal processing used in this report. Firstly, the following symbolic convention is used to describe the short-time Fourier transform [89] of a sound pressure signal.

$$X_{f,t} = \text{STFT} \{p_t\} = A_{f,t} \exp(j \cdot \phi_{f,t}) \quad (2.1)$$

Sound spectra and spectrograms in aeroacoustic models are usually reported as pressure spectral densities ($P_{f,t}$ in Pa^2/Hz), while most attenuation models are defined in terms of spectral amplitude, the conversion is established as

$$A_{f,t} = \sqrt{P_{f,t}} \quad (2.2)$$

It is common practice for the analysis of sound to express sound spectra as logarithmic levels in decibels (dB). This report expresses sound spectra as Pressure Band Level (PBL) spectra in one-third octave bands. These are determined as follows:

$$\text{PBL}_{f_c} \text{ (dB)} = 10 \log_{10} \left(\frac{\sum_{f=f_l}^{f_u} P_f(f_u - f_l)}{(2 \times 10^{-5})^2} \right) \quad (2.3)$$

where the central, lower and upper frequencies (f_c, f_l, f_u ; respectively) of the one-third octave bands are:

$$\begin{aligned} f_c &= 10^3 \cdot 2^{i/3} \quad \forall i \in [-18, 13] \\ f_l &= f_c \cdot 2^{-1/6} \\ f_u &= f_c \cdot 2^{1/6} \end{aligned}$$

In the case of power spectral densities, it may be desired to express the density as a Pressure Spectral Level (PSL) in decibels per Hertz (dB/Hz), which is determined as:

$$\text{PSL}_f = 10 \log_{10} \left(\frac{P_f}{(2 \times 10^{-5})^2} \right) \quad (2.4)$$

For expressing attenuation spectra, such as those of atmospheric absorption, the ratios A/A_0 are expressed in decibels as well and determined as:

$$\text{Att} = 10 \log_{10} \left(\frac{A}{A_0} \right) \quad (2.5)$$

To determine the pressure spectral density of sound samples, this work uses Welch's method [90], as implemented in the *Python SciPy* module [91]. The inverse short-time Fourier transform implementation from the same module is used for the inversion of spectrograms. It should be noted that this implementation uses the methods described by Griffin and Lim [92], meaning they are not pure inverse fast Fourier transforms.

2.4. Current Auralisation Methods

A few auralisation methods for wind turbine noise are currently described in literature. An overview is provided in this section. Two fundamental paths are taken: a sample-based one or a simulation-based one. This thesis is based on aeroacoustic model outputs, so it falls somewhere between the two.

2.4.1. Sample-Based Methods

Sample-based auralisation is quite common in other fields of study and is frequently proposed for wind turbine noise [23], [93]–[95].

Pieren et al. [93], [94] have worked on a technique to auralise existing wind turbines in the context of research on the auralisation of environmental sound. Their technique synthesises the sound by spectral shaping to match the provided sound samples. They use several fixed monopole sources in the rotor disk to emit this synthesised sound with atmospheric absorption and ground effects as a filter. Source motion is also compensated for by appropriate frequency domain filtering.

Butera et al. [23] use a technique where the sound is measured at multiple stations and then played back from speakers in an identical configuration with necessary filtering to compensate for the microphone and speaker arrays. This technique is limited to reproducing what has been measured and is an edge case of the definition of auralisation.

Finne and Thysell [95] used a technique where sound is recorded at a known location from the source. This recording is then backpropagated to the source location through the propagation filter. The resulting virtual sound source is then propagated to the observer location through the same filter with different parameters.

These auralisation techniques are limited to representing wind turbine noise in the operational conditions at the time of recording the noise samples. Extensive measurement campaigns are required to study turbine noise in multiple conditions. The study by Butera et al. [23] indicates the desire from the public to be presented with wind turbine noise in various situations, which can be expensive in a sample-based approach.

2.4.2. Simulation-Based Methods

In simulation-based wind turbine auralisation, the number of current projects is limited. Two distinct types of simulation are under consideration.

The first type involves a blade element approach to the problem. Mascarenhas, Cotté and Duaré [27], [96] propose a method where a wind turbine blade is discretised. On these discrete elements, flow conditions are determined to be plugged into the models by Amiet [38], [47] with extensions by Roger and Moreau [97]. The method does not model any of the above-described effects on sound propagation.

Bresciani, Maillard and Santana [28] propose another blade-element-based method that uses Amiet's theory [38], [47] with Corcos' turbulence correlation length model [98] and Goody's wall pressure spectrum model [55]. The input parameters for the noise model are obtained through 2D incompressible RANS simulations, with *STAR-CCM+* software [99], of the airfoils at each blade section. Propagation is done through the *Harmonoise model for predicting environmental noise* [100].

In the presented blade-element-based methods, the rotor aerodynamics to determine the local flow conditions are highly simplified and identified as a potential point of improvement. Applying auralisation to industry tools, such as the Horizontal Axis Wind turbine simulation Code (*HAWC2*) [101], *SILANT* [30] or *OpenFAST* [32], may increase the inherent consideration of wind turbine noise annoyance in the rotor design while improving the flow modelling.

Van der Velden and Casalino [29], [102] propose a more computationally expensive, full CFD-CAA method for auralising wind turbine sound. Flow around the wind turbine is resolved using *SIMULIA PowerFLOW's* Lattice Boltzmann Method [103]. A frequency-domain Ffowcs-Williams and Hawking calculation [104] is used to compute the wall pressure fluctuations. Ground effects are taken into account through a source mirroring technique. This method is targeted at certification, and its high computational cost is identified as a limiting factor for application in a wind turbine rotors' highly iterative design process.

The current work aims to improve the current wind turbine noise auralisation methods by using *HAWC2* as the basis tool to determine the source noise while applying a more complete sound propagation model than most other methods. This allows the quick simulation of multiple operational conditions without requiring an extensive noise measurement campaign. This method can also limit the computational cost, encouraging broader industrial and research applications. This work is also targeted specifically at psychoacoustic research of wind turbine noise annoyance and is to be validated as such. Different ways of achieving audible sound signals and the binaural rendering of these signals are also explored.

3

Source Model

The first principle step described by Vorländer [33] is the source description. This chapter mainly consists of a description of the aeroacoustic model attached to DTU's aeroelastic code *HAWC2* [31], [101] and the methodology to implement it into the toolchain, since this is the focus of the current work.

3.1. HAWC2 Aeroacoustics Model

This section aims to describe the aeroacoustic model in *HAWC2* in the detail needed for this project. First, the aerodynamic source models are covered. Next, the coupling with the *HAWC2* aeroelastic code is described, after which some additional considerations are noted.

3.1.1. Aerodynamic Source Models

This section briefly overviews the noise source models used in the *HAWC2* aeroacoustics module as presented by Bertagnolio, Madsen and Fischer [31]. While more models are available in the code than described here [101], they are not described in the literature and thus not in this section.

First is the turbulent inflow model, which is based on Amiet's theory [38], [105]. This model makes use of a frozen turbulence hypothesis for the impinging flow on an airfoil. The shape of a flat plate is used to represent the airfoil, which is a good approximation so long the thickness is smaller than the noise-generating vortices. A model by Moriarty, Guidati, and Migliore [43] is implemented to account for discrepancies in experimental data caused by a thick leading edge [41], [106]. Amiet's theory uses the Van Kármán model for the turbulence spectral tensor. This model uses the assumption of isotropic turbulence, which does not hold for the anisotropic turbulence encountered in the atmosphere. Therefore, the Mann turbulence model [40] is implemented in the TI model as a substitute for isotropic turbulence.

The second modelled source is turbulent boundary layer trailing edge noise. A variant of the TNO model is used [50], which combines the boundary layer turbulence anisotropy approach by Bertagnolio et al. [107] with the trailing edge noise scattering model by Howe [46]. Directivity effects are modelled with the method described by Brooks, Pope and Marcolini [36]. The models require parameters describing the boundary layer under the simulated conditions, which are obtained through software such as XFOil [52] or CFD tools such as EllipSys2D [108]–[110]. Different hypotheses can be used to investigate these parameters [43], [107], [111].

Lastly, a stall noise model is included in the form described by Bertagnolio et al. [68]. The methodology is based on Amiet's theory, where the separation and stall noise are modelled from a set of standard input parameters and a separation location determined with tools like XFOil or a CFD solver. Due to the known inaccuracy of the latter tools in predicting the separation angle of attack, the resulting separation location is also assumed to be inaccurate. Bertagnolio and Fischer (F. Bertagnolio and A. W. Fischer, private communication, Oct. 6, 2023) consider the stall noise to be the biggest limitation in the noise predictions at high inflow velocities, especially for stall-controlled wind turbines.

3.1.2. Coupling with HAWC2 Aeroelastic Code

All the above models require a set of standard input parameters, which describe the local flow conditions over the blade elements. These are obtained from the standard outputs of the *HAWC2* aeroelastic simulations. The local boundary layer parameters are also required for some of the noise models. The procedure in *HAWC2* is to compute a table with these parameters per angle of attack and boundary layer beforehand, which the noise models can call on-the-fly. The data for these tables can be generated with airfoil flow simulations [31].

It is important to note that the above models are formulated in the frequency domain, while the *HAWC2* aeroelastic simulations take place in the time domain. The time scales involved in aerodynamic and aeroacoustic processes are considered large enough to assume the noise evaluation can be done under a steady-state assumption at each time step. This assumption holds as long as the time step is small enough compared to the lowest desired resolved sound frequency. A more in-depth explanation is provided by Bertagnolio et al. [31].

3.1.3. Other Considerations

The propagation in the *HAWC2* aeroacoustic predictions is limited to include only spherical spreading [101]. In a meeting with Bertagnolio (F. Bertagnolio, private communication, Mar. 14, 2023), it is clarified that the effects of source movements (such as Doppler frequency and time shifts, and convective amplification) are also included in the model, as this is considered inherent to moving source modelling. Only direct propagation to a list of given receiver locations is considered. No ground reflection or atmospheric diffraction is considered.

The output to be expected from *HAWC2* are sound spectra at set time steps (spectrogram). The spectra are given for each aerodynamic source and a combination of all sources. All these spectra are also given per individual blade and summed over all blades [31]. This opens up the possibility to consider each noise type separately in the auralisation and thus investigate the effect of reductions in each category. It also allows for source modelling per blade instead of considering the turbine as a single large sound source.

It is noted that other codes similar to the aeroacoustic module of *HAWC2* are available. These include SILANT by Boorsma and Schepers [30], and the module for openFAST by Bortolotti et al. [32]. The in- and outputs of both tools are similar enough to *HAWC2*, making it possible to adapt the current work to these tools rather easily.

3.2. Sound Source Model

There are a few ways to go about implementing the *HAWC2* code into an auralisation sound source. Ultimately, a method requiring more computations by *HAWC2* is chosen, which limits the number of assumptions imposed on the sound source directivity. It involves running *HAWC2* with a sphere of receiver points and propagating the sound from those. It does require an assumption of the location of a singular representative source on the wind turbine blade, which is based on acoustic imaging of a wind turbine. The full sound source model is presented in Figure 3.1.

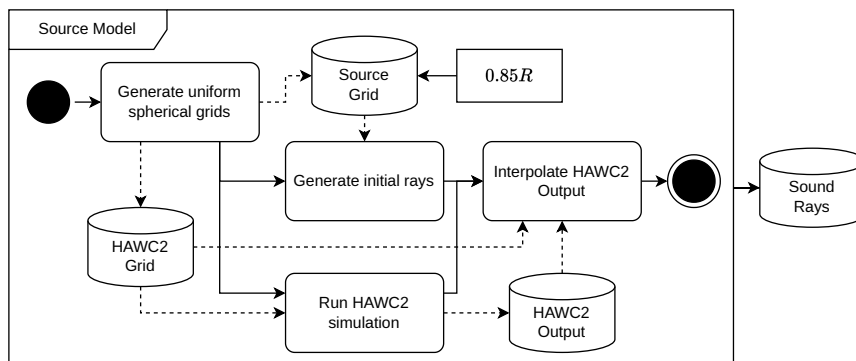


Figure 3.1: Flowchart of the sound source model. Solid arrows represent logical flow, dashed lines represent data flow.

The result from this source model is a large list of sound rays: one per blade, one per simulation time step, and one per point on the spherical grid. Hence, the compute time of the auralisation tool will scale linearly with both simulation time resolution and spatial resolution of the sound source model. The propagation of these sound rays is described in chapter 4. The details of the steps in the flowchart are described in the following subsections.

3.2.1. Generation of Uniformly Spaced Spherical Grid

As shown in Figure 3.1, uniformly spaced spherical grids are used at multiple points in the source model. The process for generating the grid points is based on a method by Deserno [112] and described in algorithm 1. The grid resulting from the algorithm represents a unit sphere around the origin of the coordinate systems. This sphere is thus to be scaled and offset for use in the different parts of the source model.

For the simulations in *HAWC2*, this unit sphere is adjusted to encompass the entire turbine rotor, as illustrated in Figure 3.2. It is then input as the observer points where the turbine noise is calculated. In order to ensure the rotor does not intersect with this sphere, the grid radius should always be larger than the rotor radius.

Algorithm 1: Deserno algorithm for generating a uniformly spaced spherical grid [112], rewritten with current nomenclature.

```

1 Set  $N_{ray} = 0$ ;
2 Set  $a_d = 4\pi/N$  and  $d_d = \sqrt{a_d}$ ;
3 Set  $M_{polar} = \text{round}(\pi/d)$ ;
4 Set  $d_{polar} = \pi/M_{polar}$  and  $d_{azimuth} = a_d/d_{polar}$ ;
5 for each  $m$  in  $0, 1, \dots, M_{polar} - 1$  do
6   Set  $\phi_d = \pi(m + 0.5)/M_{polar}$ ;
7   Set  $M_{azimuth} = \text{round}(2\pi \sin \phi_d/d_{azimuth})$ ;
8   for each  $n$  in  $0, 1, \dots, M_{azimuth} - 1$  do
9     Set  $\theta_d = 2\pi n/M_{azimuth}$ ;
10    Create point with polar coordinate  $\vec{S}(1, \theta_d, \phi_d)$ ;
11    Set  $N_{ray} \leftarrow N_{ray} + 1$ 
12  end
13 end

```

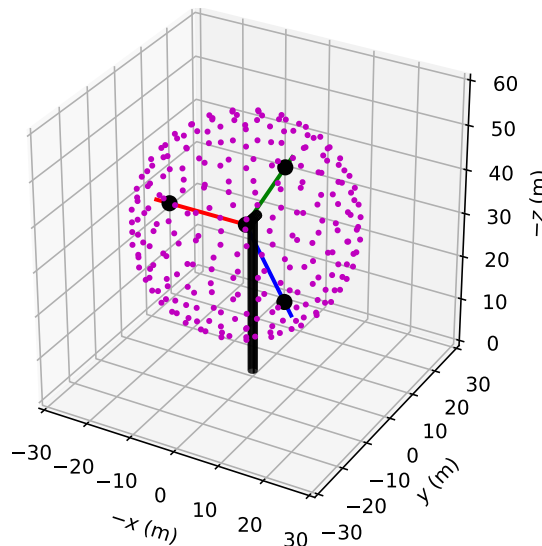


Figure 3.2: Uniform spherical grid, used as observer points in *HAWC2*. Illustrated with a representation of a wind turbine.

3.2.2. Sound Ray Initialisation

In order to give the sound rays an initial propagation velocity and wavefront direction, it is assumed to originate at a single point source per blade. This singular source is located at the location of most sound energy, as found through acoustic imaging. The studies by Oerlemans, Méndez López, and Sijtsma [113], [114] show an approximate location of most sound energy at approximately $r = 0.85R$ in Figure 3.3, which is also consistent when considering different surface treatments. Technically speaking, this location is turbine-specific. However, it works as a first estimation for validating the auralisation tool. It is left as an input parameter so it can be adjusted later.

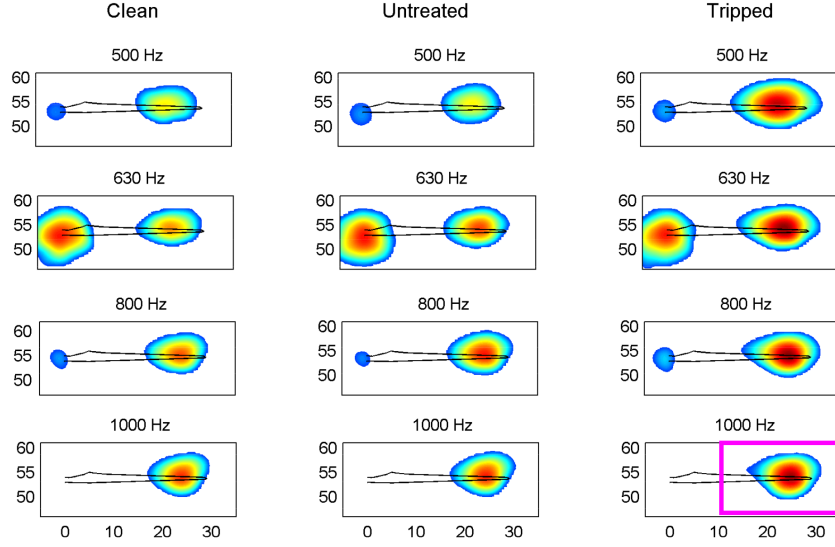


Figure 3.3: “Typical acoustic source plots showing the noise sources on the individual blades. The black line indicates the blade contour (leading edge on lower side). The range of the colour scale is 12 dB and the colour scale is the same for each row” [113, Fig. 7].

A secondary uniform spherical grid is set around the point at 85% of the blade radius, which is illustrated in Figure 3.4a. Lines are then determined through the source point $\vec{\xi}$ and each point on the secondary grid \vec{x}_{SG} , as shown in Figure 3.4b. These lines are then extended towards the sphere of *HAWC2* results, with centre point \vec{x}_{H2} and radius r_{H2} . This is shown in Figure 3.4c. The intersection of the initial lines and the sphere of *HAWC2* results is determined by solving Equation 3.1a and 3.1b:

$$\|\vec{x} - \vec{x}_{H2}\|^2 = r_{H2}^2 \quad (3.1a)$$

$$\vec{x} - \vec{\xi} = d \frac{\vec{x}_{SG} - \vec{\xi}}{\|\vec{x}_{SG} - \vec{\xi}\|} \quad (3.1b)$$

This results in a determinant ∇ and distance d , as given in Equation 3.2, considering the sphere around the source point is of unit radius. Due to the design of the source model, $\nabla > 0$ which indicates two intersection points. Only the intersection in the direction from source point $\vec{\xi}$ through unit sphere point \vec{x}_{SG} is used, which corresponds to the distance equation with the positive square root of the determinant in Equation 3.2b.

$$\nabla = \left[(\vec{x}_{SG} - \vec{\xi}) \circ (\vec{\xi} - \vec{x}_{H2}) \right]^2 - \left(\|\vec{\xi} - \vec{x}_{H2}\|^2 - r_{H2}^2 \right) \quad (3.2a)$$

$$d = - \left[(\vec{x}_{SG} - \vec{\xi}) \circ (\vec{\xi} - \vec{x}_{H2}) \right] \pm \sqrt{\nabla} \quad (3.2b)$$

After determining the initial lines and intersection, the initial sound rays are given a sound amplitude spectrum. This process is described in the following subsection.

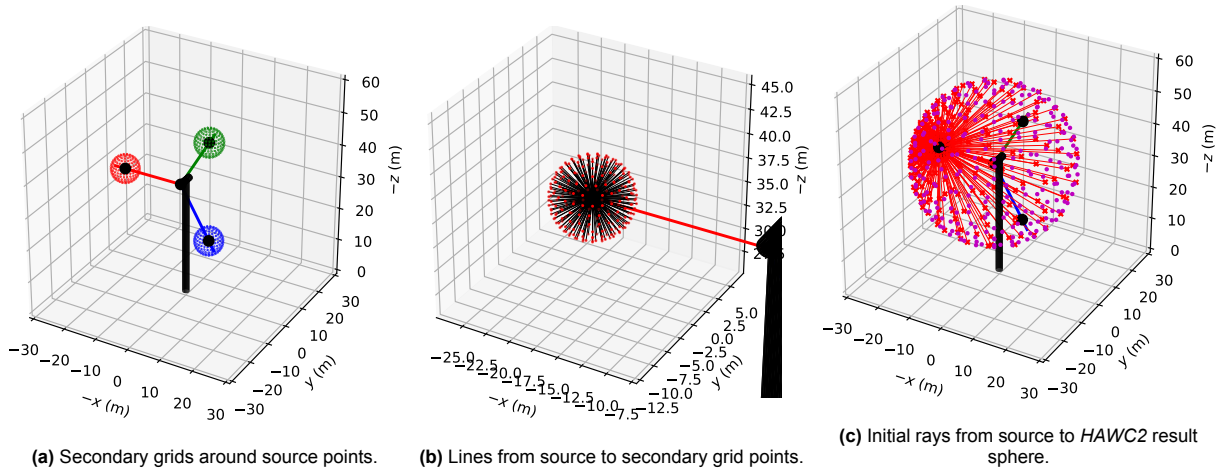


Figure 3.4: Visualisation of the initialisation of the sound rays in the source model.

3.2.3. Interpolation of HAWC2 results

Since the *HAWC2* aeroacoustic model is currently limited to 255 sound observer points [101, p. 68], a method is implemented to interpolate this limited number of points to the intersection points. Under the assumption that these points are approximately located in a plane defined by the three closest points of the *HAWC2* observations, a 2D triangular interpolation is done. This is described in Equation 3.3, where the numbered points \vec{x}_i are the locations of the *HAWC2* output v_i , as illustrated in Figure 3.5. v is the interpolated output at point \vec{x} .

$$v(\vec{x}) = \frac{\frac{v_1}{d_1} + \frac{v_2}{d_2} + \frac{v_3}{d_3}}{\frac{1}{d_1} + \frac{1}{d_2} + \frac{1}{d_3}} \quad d_i = \|\vec{x} - \vec{x}_i\| \quad (3.3)$$

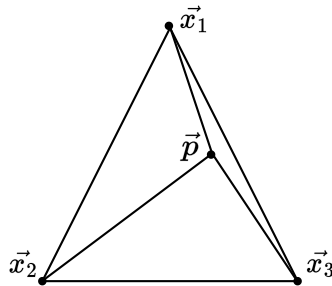


Figure 3.5: Visual representation of the interpolation triangle.

The *HAWC2* aeroacoustic simulations are run on larger time steps than the auralisation itself. For this reason, the *HAWC2* results are linearly interpolated to the smaller simulation time step of the propagation model. Since the sound spectra are expressed in Pa²/Hz, corresponding to the sound energy content, the *HAWC2* spectrograms are interpolated linearly to achieve continuous energy rather than pressure levels.

4

Propagation Model

The second large component of auralisation is propagation. Many numerical methods exist to describe the propagation of sound signals. These will be shortly presented based on the work by Vorländer [33] and Yunus [85]. The selected method for this work is further worked out in section 4.2.

4.1. Existing Numerical Methods

In order to simulate the physics of sound propagation, as described in section 2.2, an appropriate modelling approach is to be selected. There are two classes of methods that can be considered for outdoor propagation of sound: wave-based and geometrical acoustics [33], [85].

Wave-based methods solve the discretised wave equations on a spatial grid. Some of these methods are the finite-element method, boundary element method, and finite-difference time-domain method, which deal with the full wave equations. More simplified methods include the pseudo-spectral time domain methods, transmission line matrix, parabolic equation and the fast field program. Because these methods directly deal with the wave equations, they can provide insight into wave propagation behaviour. Most of these methods are described to have high computational costs [33], [85]. The complexity of implementing a meshing tool and differential equation solver and the fact that no solvers are available to the author at the time of writing rule out the use of these methods in this thesis.

The methods under consideration for this work fall under the geometrical acoustics methods. These methods hypothesise that the travel of sound and the associated energy flow can be depicted by lines called rays. Geometrical acoustics (ray acoustic methods) have been applied to many indoor and outdoor propagation problems. The most common methods are image source, ray tracing, and beam tracing [33], [85].

The simplest of these methods is the image source method, which is illustrated by Figure 4.1. In this method, one direct ray is considered, which is a straight line from source to receiver (r_1 in the Figure 4.1). Surface reflections are considered by mirroring the source around a surface and determining a second straight line from the mirror source to the receiver (r_2 in the Figure 4.1). The process of determining reflections is repeated for all combinations of sources and surfaces, where the following condition is met: *“If we run a specular ray tracing process and find a receiver hit by a ray, the corresponding image source must be audible”* [33, p. 204]. While the computational cost and complexity of the image source method are low, it cannot easily account for refraction and scattering of sound. Its computational cost increases exponentially with the number of polygonal surfaces, which is the biggest downside of the method [33], [85].

In complex environments, ray tracing is a popular approach. It was originally developed for geometrical optics. In this method, rays are considered as the propagation paths perpendicular to the wavefronts and are described by the eikonal equation [85], [86]. While the method is very popular in outdoor propagation, it is known to suffer from singularities at caustics and shadow boundaries [86], [115]. Ray tracing requires the computation of eigenrays connecting the source(s) and receiver(s), for which many methods exist [85].

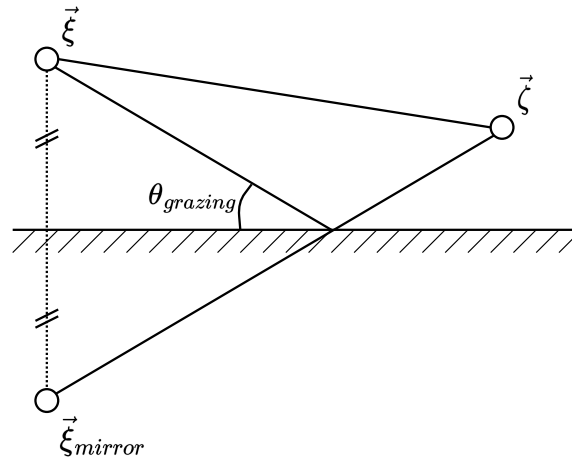


Figure 4.1: Illustration of the image source model .

Beam tracing is an extension of ray tracing, where the rays are considered as beams with a width. When considering multiple receivers over a vast area, which is a use case considered for the code in this thesis, beam tracing is preferred as it does not require the identification of eigenrays [116], [117]. Different variants of beam tracing exist, one of which is Gaussian Beam Tracing. This is the method chosen in this work for its relative robustness compared to other beam tracing methods[85].

4.2. Beam Tracing Methodology

The Gaussian beam tracing methodology in this work is presented in Figure 4.2. I can be roughly divided in three parts: the tracing of the central rays, the propagation effects and the Gaussian reception. Each part of the propagation model is discussed in a dedicated subsection. The generation of the ray geometry is described in subsection 4.2.1. The propagation effects, among which atmospheric absorption, are described in subsection 4.2.2 and the Gaussian reception is covered in subsection 4.2.3.

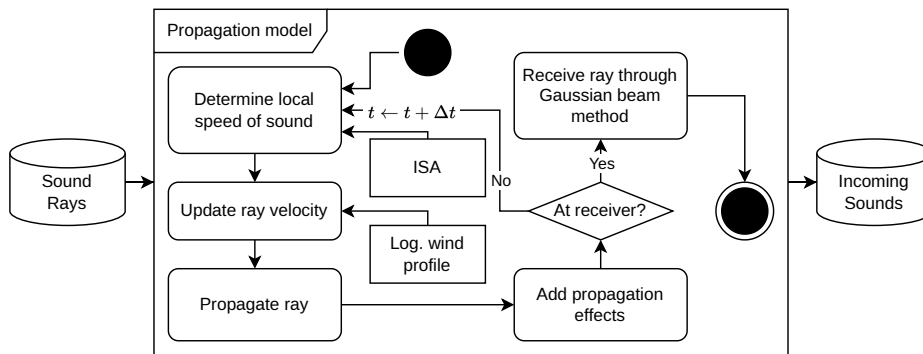


Figure 4.2: Flowchart of the sound propagation model.

4.2.1. Central ray tracing

For tracing the central ray of the Gaussian beams, the method described by Arntzen is followed, where two differential equations are solved: a ray position equation [86, Eq. 3.30], and a wavefront direction equation [86, Eq. 3.31]. For this work, these equations are solved numerically with a forward Euler scheme [118], [119]. The reference system used for the following ray tracing methodology is presented in Figure 4.3. Unless otherwise specified, all vectors are defined in the Cartesian coordinate system (see Figure A.1), where the turbine rotor is aligned with the x -axis.

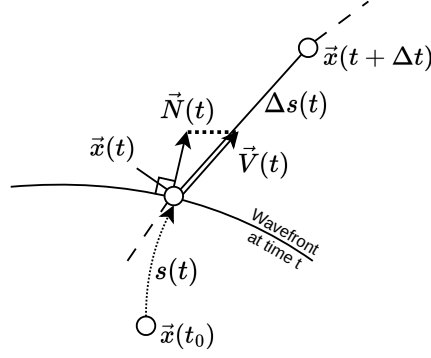


Figure 4.3: Reference system used for the ray tracing method in this work.

Equation 4.1a describes the change in wavefront direction at time t , where the forward Euler scheme to solve the wavefront direction is expressed in Equation 4.1b. Since only a stratified atmosphere is considered, the divergence of wind speed ($\vec{\nabla} \circ \vec{U}(t)$) is zero, and the speed of sound gradient only has a z-component.

$$\left. \frac{d\vec{N}}{dt} \right|_t = - \left\| \vec{N}(t - \Delta t) \right\| \cdot \vec{\nabla}_c(\vec{x}(t)) + \vec{\nabla} \circ \vec{U}(\vec{x}(t)) \quad (4.1a)$$

$$\vec{N}(t) = \vec{N}(t - \Delta t) + \left. \frac{d\vec{N}}{dt} \right|_t \Delta t \quad (4.1b)$$

When the wavefront direction is solved, the ray velocity vector can be updated according to Equation 4.2a to solve the ray position with Equation 4.2b.

$$\vec{V}(t) = \vec{U}(\vec{x}(t)) + c(\vec{x}(t)) \cdot \frac{\vec{N}(t)}{\left\| \vec{N}(t) \right\|} \quad (4.2a)$$

$$\vec{x}(t + \Delta t) = \vec{x}(t) + \vec{V}(t)\Delta t \quad (4.2b)$$

A logarithmic wind profile is used, where the wind speed magnitude $U = |\vec{U}|$ is defined by Equation 4.3a and 4.3b, based on a reference wind $U(z_{ref})$ at height z_{ref} . The reference for the wind speed profile is shown in Figure 4.4. The magnitude is applied to the unit vector in y-direction, $\vec{C}(0, 1, 0)$, to match the definition of the wind direction of *HAWC2*.

$$U(z) = U(z_0) \ln \left(\frac{z}{z_0} \right) \quad (4.3a)$$

$$U(z_0) = \frac{U(z_{ref})}{\ln \left(\frac{z_{ref}}{z_0} \right)} \quad (4.3b)$$

The sound speed profile is based on its defining equation [120, Eq. 8.25] with an atmospheric temperature profile applied in Equation 4.4. This temperature profile is to be obtained from the ISO Standard Atmosphere (ISA) [121].

$$c(t) = \sqrt{\gamma R_0 T(z(t))} \quad (4.4)$$

For the propagation effects described in the next section, it is important to track the propagation distance s , which is done through Equation 4.5a and 4.5b.

$$\Delta s(t) = \left| \vec{V}(t) \Delta t \right| \quad (4.5a)$$

$$s(t + \Delta t) = s(t) + \Delta s(t) \quad (4.5b)$$

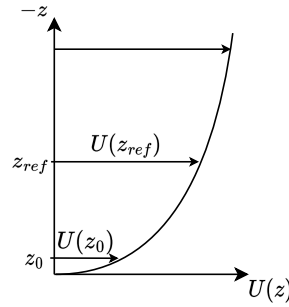


Figure 4.4: Reference frame for the logarithmic wind profile. Note the height is in negative z -direction to match the coordinate systems used in this thesis (see Appendix A).

4.2.2. Sound propagation effects

With the basic ray tracing method set out, propagation effects can be added. Since the equations and physics allow, this is done at each propagation time step, as they all require the use of properties that change along the path. The logic of applying the effects at the end of the propagation process is shown in Figure 4.5.

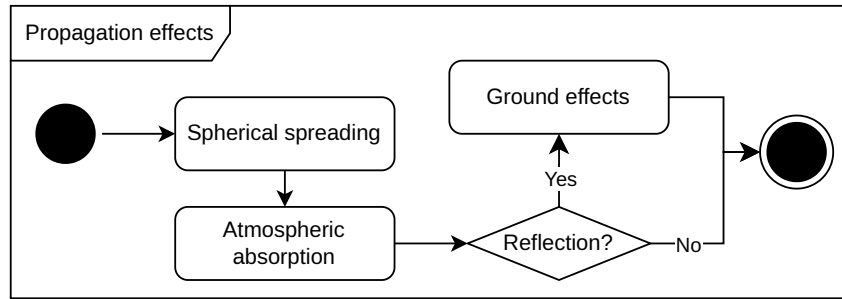


Figure 4.5: Flowchart of the sound propagation model.

Since the output of *HAWC2* is narrowband spectra at the central frequencies of fraction octave bands, it is decided to interpolate these results to an evenly spaced narrowband spectrum. This is mainly done to increase the accuracy of the propagation effects, as they have narrowband peaks and lows that would not be captured with limited frequencies. Interpolation is executed with the piece-wise linear *NumPy* [122] *interp* function.

Spherical spreading

First is spherical spreading, which is well described for ray tracing by Arntzen [86, Eq. 3.43] in the form of Equation 4.6:

$$A_f(t + \Delta t) = A_f(t) \sqrt{\frac{c(t + \Delta t) \cdot S(t)}{c(t) \cdot S(t + \Delta t)}} \quad (4.6)$$

This equation can easily be applied at each time step as all the necessary properties are tracked over time or can be recomputed. When ray cones with an angular width of $\delta\alpha$ are considered, the surface area S_t at time step t can be determined by Equation 4.7:

$$S(t) = \pi \left(s(t) \cdot \frac{1}{2} \delta\alpha \right)^2 \quad (4.7)$$

Hence, Equation 4.6 can be rewritten as Equation 4.8, which is consistent with the standard spherical spreading equation:

$$\frac{A_f(t + \Delta t)}{A_f(t)} = \frac{s(t)}{s(t + \Delta t)} \sqrt{\frac{c(t + \Delta t)}{c(t)}} \quad (4.8)$$

Atmospheric absorption

The effect of atmospheric absorption or attenuation is described by Bass et al. [82], [83], which is also used by the ISO 9613-1 standard for sound propagation [84]. They describe an absorption coefficient dependent on the temperature, pressure and humidity, with Equation 4.9 [82, Eq. 1]. The atmospheric conditions are again determined from the ISA described in [121].

$$\alpha(f) = f^2 \left[\left(\frac{1.84 \times 10^{-11}}{\left(\frac{T_0}{T}\right)^{\frac{1}{2}} \frac{p_s}{p_{s0}}} \right) + \left(\frac{T_0}{T}\right)^{2.5} \left(\frac{0.10680e^{-3352/T} f_{r,N}}{f^2 + f_{r,N}^2} + \frac{0.01278e^{-2239.1/T} f_{r,O}}{f^2 + f_{r,O}^2} \right) \right] \quad (4.9)$$

where the reference temperature is $T_0 = 293.15$ K and the reference atmospheric pressure is $p_{s0} = 101,325$ Pa. The resonance frequencies of Nitrogen and Oxygen are defined in terms of the atmospheric conditions by Equation 4.10a and Equation 4.10b, respectively [82, Eq. 2, 3]:

$$f_{r,N} = \frac{p_s}{p_{s0}} \left(\frac{T_0}{T}\right)^{\frac{1}{2}} \left(9 + 280 \cdot H \cdot \exp \left(-4.17 \left[\left(\frac{T_0}{T}\right)^{1/3} - 1 \right] \right) \right) \quad (4.10a)$$

$$f_{r,O} = \frac{p_s}{p_{s0}} \left(24 + 4.04 \times 10^4 \cdot H \cdot \frac{0.02 + H}{0.391 + H} \right) \quad (4.10b)$$

where the absolute humidity H can be determined from the relative humidity h through Equation 4.11 [82, Eq. 4]:

$$H = h \cdot \frac{p_{sat}}{p_s} \quad (4.11)$$

where the water vapour saturation pressure p_{sat} is given by Bass et al. [83, Eq. 2] as Equation 4.12:

$$\log_{10} \left(\frac{p_{sat}}{p_{s0}} \right) = -6.8346 \left(\frac{T_{01}}{T} \right)^{1.261} + 4.6151 \quad (4.12)$$

The atmospheric absorption is applied with Equation 4.13 [88, Eq. 4.5]:

$$\frac{A_f(t + \Delta t)}{A_f(t)} = e^{-\alpha \Delta s(t)/2} \quad (4.13)$$

Ground effects

An important part of outdoor sound propagation is ground reflection and its associated effects. These are accounted for with the method described by Embleton, Piercy and Daigle [81] and by Arntzen [86]. With each reflection on the ground, a ground reflection coefficient Q is applied to the reflected sound ray. This coefficient Q is described by Equation 4.14 [86, Eq. 3.16]:

$$Q = R_p + (1 - R_p)F_s \quad (4.14)$$

Where R_p is a wave reflection coefficient, and F_s is a spherical wave correction factor. The reflection coefficient is related to the sound impedance Z and the grazing angle $\theta_{grazing}$ by Equation 4.15 [86, Eq. 3.17]:

$$R_p = \frac{Z \sin \theta_{grazing} - 1}{Z \sin \theta_{grazing} + 1} \quad (4.15)$$

While the spherical wave correction factor is related to a numerical distance w by Equation 4.16 [86, Eq. 3.18]:

$$F_s = 1 + jw\sqrt{\pi}e^{-w^2} \operatorname{erfc}(-iw) \quad (4.16)$$

The numerical distance w is based on work by Ingard [123], Chessell [124] and Hubbard [125], and given by Arntzen [86, Eq. 3.19] in the form of Equation 4.17, where $k = 2\pi f/c$:

$$w^2 = j \frac{2\pi f r_2}{c} \frac{(\sin \theta_{\text{grazing}} + 1/Z)^2}{2(1 + \sin \theta_{\text{grazing}}/Z)} \quad (4.17)$$

The complex complementary error function in Equation 4.16 is approximated through the method implemented in *Python's* [126] SciPy module [91].

Arntzen [86, Eq. 3.20] gives the ground impedance, from the work by Delany and Bazley [127] as Equation 4.18:

$$Z = 1 + 0.0511 \left(\frac{f}{\sigma_e} \right)^{-0.75} + 0.0768j \left(\frac{f}{\sigma_e} \right)^{-0.73} \quad (4.18)$$

where typical values of the flow resistivity factor σ_e are given by Sutherland and Daigle [128, Tab. 2], as presented in Table 4.1:

Table 4.1: Ranges of typical flow resistivity [kPa s/m²][128, Tab. 2]

Soil	Lower σ_e	Higher σ_e	Used σ_e
Concrete	30,000	100,000	50,000
New asphalt	5,000	15,000	10,000
Dirt, wet	4,000	8,000	5,000
Dirt, roadside	300	800	500
Grass lawn	125	300	250
Forest floor	20	80	50
Snow	1.3	50	25

4.2.3. Gaussian beam reception

As described above, Gaussian beam tracing is used in this work, which requires setting up a reception method for these beams. It consists of two steps: detecting the reception and the determination of the received amplitude.

Since the only necessary requirement for reception is a ray passing a receiver point, a method to check this is implemented. It determines planes perpendicular to the ray at the last two positions. The geometry is shown in Figure 4.6. Each plane is defined by a point and normal vector, as defined in Equation 4.19.

$$\text{Plane 1:} \quad \vec{p}_1 = \vec{x}(t) \quad \vec{n}_1 = \frac{\vec{x}(t + \Delta t) - \vec{x}(t)}{\|\vec{x}(t + \Delta t) - \vec{x}(t)\|} \quad (4.19a)$$

$$\text{Plane 2:} \quad \vec{p}_2 = \vec{x}(t + \Delta t) \quad \vec{n}_2 = \frac{\vec{x}(t) - \vec{x}(t + \Delta t)}{\|\vec{x}(t) - \vec{x}(t + \Delta t)\|} \quad (4.19b)$$

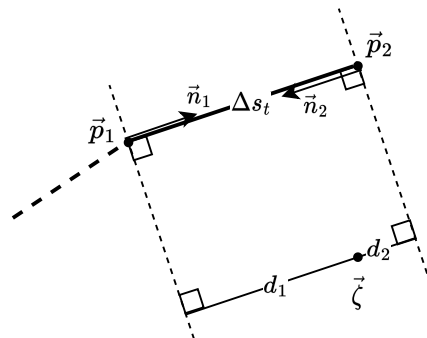


Figure 4.6: Geometry used to check the reception of a sound ray.

When the perpendicular distance (d_1 and d_2) from either plane to the receiver point is less than the last Δs_t , the ray has passed the receiver point. This condition is expressed in Equation 4.20.

$$d_1 = \left| \vec{n}_1 \circ (\vec{\zeta} - \vec{p}_1) \right| \leq \Delta s(t) \quad \text{and} \quad d_2 = \left| \vec{n}_2 \circ (\vec{\zeta} - \vec{p}_2) \right| \leq \Delta s(t) \quad (4.20)$$

If this condition is met, a ray is marked as received and propagation is stopped. Then, the received sound amplitude is to be determined. Portner and Bucker [116] describe the bell curve for the attenuation with Equation 4.21a [116, Eqs. 13]. The reference frame of this bell curve is shown in Figure 4.7.

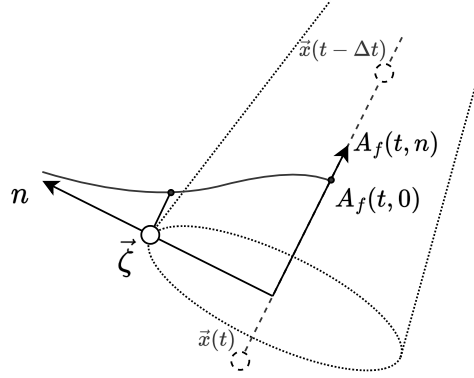


Figure 4.7: Reference frame for the bell curve in Equation 4.21c

For a uniformly spaced spherical grid with separation angle $\delta\alpha$ between the rays, the ray cones cover enough space when ϵ is defined by Equation 4.21b [116, Eqs. 14], which results in the Gaussian curve in Equation 4.21c. It should be noted that the amplitude spectrum at the central ray $A_f(t, 0)$ is the same as the spectrum presented previously as $A_f(t)$.

$$A_f(t, n) = A_f(t, 0) \exp \left[-\frac{1}{2} \omega \epsilon n^2 / (c^2 s^2 + \epsilon^2) \right] \quad (4.21a)$$

$$\epsilon = \frac{2c^2}{\omega(\delta\alpha)^2} \quad (4.21b)$$

$$A_f(t, n) = A_f(t, 0) \exp \left[-n^2 / \left((\delta\alpha)^2 s^2 + \frac{1}{\pi f} \right) \right] \quad (4.21c)$$

The beam width $\delta\alpha$ is found from the secondary source grids of the source model, as described in subsection 3.2.2. Figure 4.8 shows the geometry used to determine the beam width, where the distance d is taken from algorithm 1. Since the grid is a unit sphere, the initial distance is $s_0 = 1$ m.

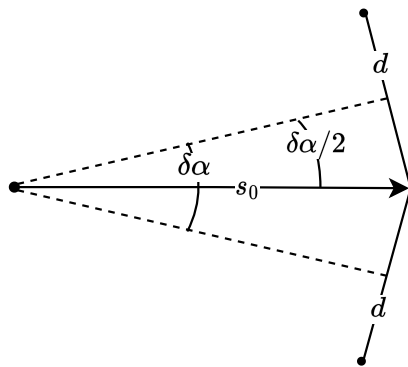


Figure 4.8: Geometry to determine the Gaussian beam width.

Trigonometry defines the beam width as Equation 4.22.

$$\sin\left(\frac{\delta\alpha}{2}\right) = \frac{d_d}{2s_0} = \frac{d_d}{2 \cdot 1} \Rightarrow \delta\alpha = 2 \arcsin\left(\frac{d_d}{2}\right) \quad (4.22)$$

The required normal distance for the Gaussian bell curve can be approximated with Equation 4.23, illustrated in Figure 4.9.

$$n = \sqrt{\|\vec{\zeta} - \vec{p}_1\|^2 - d_1^2} \quad (4.23)$$

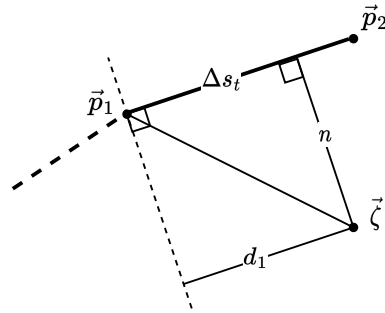


Figure 4.9: Geometry used to determine the normal distance used in the Gaussian beam model.

Since a receiver can now receive a ray without direct interception, the number of rays guaranteeing sound reception can be severely limited. This method also solves the issue of caustics and dark zones commonly found in classical ray tracing.

5

Binaural Rendering

An important part of human sound perception is our ability to localise sound [129]. Since the propagation of wind turbine noise involves ground and obstacle reflections, as well as atmospheric refraction; sound will be received from a multitude of directions. Since the setup of this thesis is to provide a tool for noise perception, rendering the sound in a directional way is very important [130].

Our ability to localise sound is made possible by our recognition of the difference in sound received by both ears. In sound research, two methods are generally applied: convolution of the sound signal with a head-related impulse response (HRIR) function; or the application of a head-related transfer function (HRTF) to the sound spectrum of the incoming signal. For a time domain analysis, it is also accepted to split the analysis into a spectral component with the HRTF and a time component in the form of an interaural time difference (ITD) function. Since this thesis focuses on spectral content in the time domain in the form of a spectrogram, the focus is on combining an HRTF with an ITD functions to achieve the binaural effect.

5.1. Head-Related Transfer Functions

HRTFs use a head-centered spherical coordinate system, shown in Figure A.1. An azimuth angle between 0 and 360 degrees in the horizontal plane and a polar angle between 0 and 90 degrees upwards from the horizontal plane are typically used. The polar angle can also be adjusted downward for sound incidence from the lower hemisphere.

It is well known that these HRTFs are very dependent on the individual, with tests showing large differences in perception through a standardised HRTF. Therefore, two methods of determining these HRTFs are generally used. These involve either artificial heads and torsos or those of individuals. Measurements are done with in-ear microphones that measure the sound response from a directional speaker system. The accepted standard dataset for an HRTF is the measurements by Gardner and Martin [131], [132] of the KEMAR artificial head and torso simulator (HATS), designed by Burkhard and Sachs [133].

5.1.1. HRTF of a HATS

Pioneered by Burkhard and Sachs [133] and Shaw [134] in the 1960s, the creation of an average head and torso simulator for the human population was studied. Databases containing these HRTFs, created with artificial heads, are well available online [131], [135]–[137].

These artificial heads are based on the dimensions of the average person in a population sample. The largest issue that is encountered is the strong dependency on the sampling method used to obtain these average dimensions. The most comprehensive study in this regard is the study by Burkhard and Sachs [133]. It can be argued, however, that in the time since that study, the average population has changed. Thus, the KEMAR torso might not be fully representative of the current population. In listening tests, it is found that dummy heads infer consistent error when it comes to sound localisation [138]. Dummies created from an individual human head are found to be almost as good as the real one [139].

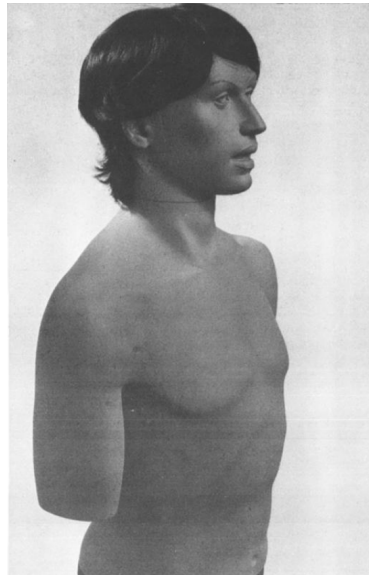


Figure 5.1: Picture of the head and torso simulator KEMAR, presented by Burkhard and Sachs [133, Fig. 5].

5.1.2. Individual HRTF

The limitations of artificial heads are well known; therefore, researchers have created databases with measurements of the HRTF of individual human heads. The main constraint in these measurements is the large time requirement to capture enough data of good quality. Centring a test subject within the loudspeaker array is also a challenge, especially due to the long duration of a measurement campaign. New signal processing techniques have been explored to create faster methods of obtaining individual HRTFs [140]–[142].

5.1.3. Head movement HRTF

If head movement is of significant concern to the listening experiment, one should account for the rotation of the head relative to the torso. Moldrzyk [143] has presented a procedure and preliminary results. This involves measuring the HRTF of a torso at multiple head movement angles and applying a head-tracking device. Databases of HRTFs that take into account head orientation are not well available. No further discussion is given since head movement is considered out of the scope of this thesis.

5.2. Interaural Time Difference

Lord Rayleigh recognised the difference in sound reception time between both ears as a significant factor in sound localisation of humans [144]. Therefore, an ITD function is researched to achieve the most realistic auralisation result possible. Analytical equations are available and well-accepted in sound localisation research. Experimental determination of the ITD is also used and researched extensively.

5.2.1. Analytical methods

Equations describing the ITD appeared in the textbook on experimental psychology by Woodworth in 1938 [145]. While no derivation or qualification is given in the original work, Feddersen [146] found it to agree well with the delay for clicks. The functions are still used in binaural acoustics and synthesis [147]–[150].

Limitations of this simple model come from the underlying assumptions: simple ray-tracing paths and a spherical head with perfectly spaced ears. Aaronson and Hartmann [151] address these limitations by developing a more thorough method based on the exact diffraction equation by Lord Rayleigh [152]. This study found that their method performs best for tones below 0.8 kHz, but the Woodworth formula provides better estimates above 1.5 kHz. For broadband sources, the Woodworth model is still found to be valuable.

5.2.2. Experimental determination

The delay time can also be determined experimentally when determining the HRTF of a test subject. Katz and Noisternig [153] recognise three families of methods to determine the ITD experimentally. Their study also extensively compares these methods, where it is concluded there are large variations in their results. These variations exceed the just-noticeable-difference by up to multiple multiples. A short summary of these methods is given for completeness.

The first family is described as thresholds methods, which determine the time of first arrival of incident sound based on a detection threshold. Examples are found in Abbagnaro et al. [154], Kuhn [155], and Begault and Trejo [156]. This method has been utilised by Algazi et al. [157] with certain pretreatments.

Another family of methods considers the time difference associated with the cross-correlation between the two ears. Examples are found in Kistler and Wightman [158], Middlebrooks [159], Macpherson and Middlebrooks [160], and Langendijk and Bronkhorst [161]. These methods are supported by the neural link to the correlation of binaural cues [162]. Instead of the absolute level of the arrival time difference, the time delay with maximum coherence of the signals in both ears is used.

Lastly, methods have been created that employ phase components of the signal to determine the group delay, which can be translated into a time delay. Jot et al. [163] and Minnaar et al. [164] have presented such methods. Methods in this family mostly differ in their selection of analysis parameters [153].

While very promising, more comparative studies are to be done with these methods in order to determine their applicability and accuracy [153]. Due to time constraints, experimental methods are not used in the current work.

5.3. Methodology

Figure 5.2 shows the process in which the binaural rendering is to be applied to the incoming sound. Firstly, the incoming direction is determined. Then, the signal is split into left and right signals in order to apply the HRTF. Based on the direction of the incoming sound, the left or right signal should be delayed to account for the reception delay. Each of these steps is described in the following subsections.

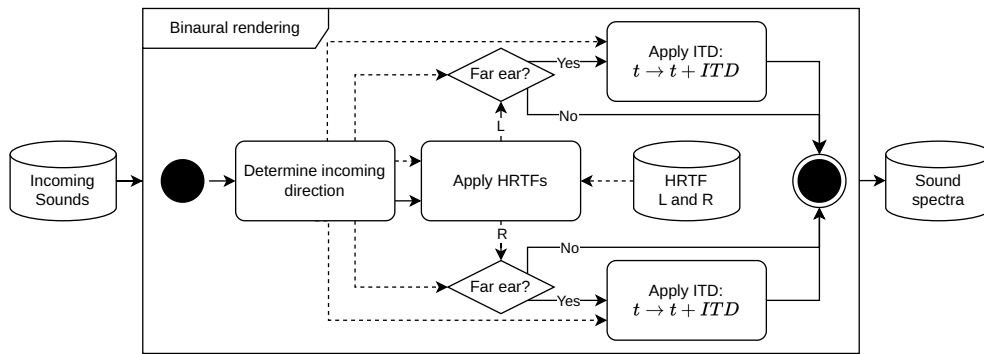


Figure 5.2: Flowchart of the reception model.

5.3.1. Determination of Incoming Direction

An important part of creating directional audio is determining the direction of the incoming sound. Each sound ray is set to store its source position $\vec{\xi}$, which is converted to a Head-Related Spherical coordinate, as described in Appendix A. The origin point of the coordinate is set as the receiver point $\vec{\zeta}$ in question. A head rotation θ_0 can be included in the input of the auralisation, which can also be added at this stage of the process. This results in the conversion described by Equation 5.1:

$$\vec{\xi} \rightarrow \vec{H}(r, \theta, \phi, \theta_0) + \vec{\zeta} \quad (5.1)$$

5.3.2. HRTF database

The MIT measurements of the KEMAR HATS by Gardner and Martin [131], [132] are used for the binaural attenuation. These are obtained through the SOFA conventions data repository [137] and implemented through the *pysofaconventions* python module [165]. From the campaign by Gardener and Martin, the data set obtained with the small pinna is selected.

The data from the SOFA conventions repository is given as HRIR functions. The HRTF is the Fourier transform of the HRIR, which is obtained computationally through the *SciPy* [91] Fast Fourier Transform (FFT). The resulting amplitude on the horizontal plane (polar angle of 0°) is presented in Figure 5.3.

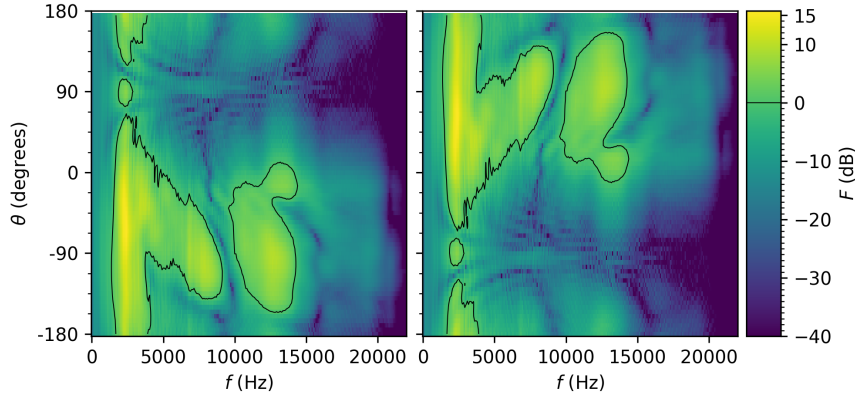


Figure 5.3: HRTF plots from the measurements by Gardner and Martin, as obtained through the SOFA convention repository [131], [132], [137], [165].

The HRIR for the left ear would be applied to a sound signal through a convolution:

$$[p(t)]_{\text{left}} = p(t) * [\text{HRIR}(t)]_{\text{left}} \quad (5.2)$$

And since the HRTF is the FFT of the HRIR, the spectral application is a simple multiplication:

$$[A_{f,t} \cdot e^{j\Delta\phi_{f,t}}]_{\text{left}} = A_f \cdot e^{j\Delta\phi_{f,t}} \cdot [\text{HRTF}_f]_{\text{left}} \quad (5.3)$$

HAWC2 is limited to outputting the wind turbine noise at the central frequencies of fractional octave bands. Since the HRTF above is in a narrowband spectrum, interpolation has to be applied. It is decided to use piece-wise linear interpolation with *NumPy*'s [122] *interp* function.

5.3.3. ITD functions

While the literature describes improved interaural time difference functions, the Woodworth model is favourable for broadband signals [151]. The equations for ears located at 90° from the front and a sound source on the right side of the head read [151, Eqs. 1a, 1b]:

$$\text{ITD} = (a/c)(\theta + \sin \theta) \quad [0 \leq \theta \leq \pi/2] \quad (5.4a)$$

$$\text{ITD} = (a/c)(\pi - \theta + \sin \theta) \quad [\pi/2 \leq \theta \leq \pi] \quad (5.4b)$$

The ITD is then applied to spectra that travel towards the "far" ear, as follows:

$$[A_{f,t+\text{ITD}} \cdot e^{j\Delta\phi_{f,t+\text{ITD}}}]_{\text{far}} \leftarrow [A_{f,t} \cdot e^{j\Delta\phi_{f,t}}]_{\text{far}} \quad (5.5)$$

Based on the work by Hartley and Fry [166], and Algazi, Avendano and Duda [157]; the head radius a is set at 87.5×10^{-3} m. It should be noted that, in most cases, the simulation timestep is much larger than the resulting interaural time delay. For this reason, the application of the ITD is left until after sound reconstruction. Otherwise, the ITD would not affect the spectrogram, which is only stored at the simulation timesteps. Adding extra timesteps to apply the ITD before reconstruction would result in significant complications in obtaining the final spectrogram.

6

Sound Reception and Signal Reconstruction

The previous chapters in this thesis are all focused on sound spectra, which require some form of spectral inversion to achieve a sound signal. In current methodologies of wind turbine auralisation, this is done by applying random phase to the spectral magnitude and applying an inverse Fourier transform. While this seems to give adequate results, different methods of achieving the final signal are explored in this thesis. These methods all apply some form of phase recovery or phase reconstruction. In section 6.1, the methods found in literature are summarised, after which the methodology for the signal reconstruction in this thesis is set out in section 6.2.

6.1. Phase Reconstruction Methods

In this first section, different phase reconstruction algorithms are summarised. The most common is the algorithm developed by Griffin and Lim (GLA) [92], described in subsection 6.1.1, along with a fast variant. Many algorithms have been derived, based on the work by Griffin and Lim, such as Real-Time Iterative Spectrogram Inversion (RTISI) in subsection 6.1.2, RTISI with look-ahead capability (RTISI-LA), a variant on RTISI by Abdelmalek, Mnasri and Benzarti [167] in subsection 6.1.3. In subsection 6.1.4, an algorithm based on a relation between spectrogram phase and magnitude is presented along with a variant for real-time reconstruction. Optimisation-based and non-iterative algorithms are summarised in subsection 6.1.5 and subsection 6.1.6. Lastly, arguments are presented for using random phase without any recovery algorithm in subsection 6.1.7.

6.1.1. Iterative Griffin and Lim Algorithm (GLA)

One of the most common algorithms for signal reconstruction from the STFT magnitude is developed by Griffin and Lim [92]. Their iterative approach, named the Griffin-Lim Algorithm, applies the inverse STFT (iSTFT) to obtain an estimate of the signal. The phase of the STFT of this signal estimate is then combined with the original STFT magnitude ($A_{f,t}^0$) to obtain the next iteration's signal estimate, p_t^{i+1} . An initial guess of the phase, $\phi_{f,t}^0$, is required, commonly set to zero or random phase.

$$X_{f,t}^i = \text{STFT} \{p_t^i\} \quad (6.1a)$$

$$p_t^{i+1} = \text{iSTFT} \left\{ A_{f,t}^0 \frac{X_{f,t}^i}{|X_{f,t}^i|} \right\} \quad (6.1b)$$

Many improvements to, variations of, and implementations of this algorithm exist, some of which are presented below. No literature proves the convergence of the GLA or any of its modifications. Care should thus be taken to monitor this.

Fast Griffin-Lim Algorithm (FGLA)

In 2013, Perraudin et al. suggested the addition of an acceleration parameter α_g to the GLA [168]. This parameter allows for faster convergence of the GLA. Still, care should be taken in selecting the magnitude of the acceleration, as too large values are known to result in divergence. Their modification of Equation 6.1 is shown in Equation 6.2:

$$X_{f,t}^i = \text{STFT} \{p_t^i\} \quad (6.2a)$$

$$X_{f,t}^{i-1} = \text{STFT} \{p_t^{i-1}\} \quad (6.2b)$$

$$p_t^{i+1} = \text{iSTFT} \left\{ A_{f,t}^0 \frac{X_{f,t}^i + \alpha_g (X_{f,t}^i - X_{f,t}^{i-1})}{|X_{f,t}^i + \alpha_g (X_{f,t}^i - X_{f,t}^{i-1})|} \right\} \quad (6.2c)$$

6.1.2. Real-Time Iterative Spectrogram Inversion (RTISI)

Inspired by GLA, Beauregard et al. proposed an efficient algorithm for application to real-time signal reconstruction [169]. Per frame of the magnitude spectrogram, part of the time signal is reconstructed similarly to GLA. The complete algorithm is presented in Figure 6.1. In the reconstruction of a frame m , one or more previous frames $m - n$ are overlap-added to the current frame estimation to account for the overlap between STFT frames.

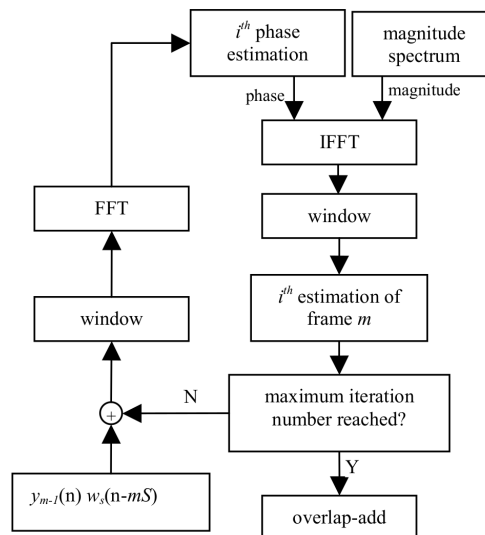


Figure 6.1: "Frame-by-frame iterative phase estimation process" [169, Fig. 2].

The authors recognise that the frame-by-frame approach inherently imposes errors in the reconstructed signal. The main issue is that the overlap-add of future frames $m + 1$, $m + 2$, ... potentially affect the spectral energy in frame m . The nature of the algorithm compensates for this additional energy in the recovery of the future frames, however. Combined with maintaining phase consistency between frames, the authors find any common source of degradation to be prevented. While fast, the algorithm is limited in achievable signal-to-noise ratio (SNR) [170].

Real-Time Iterative Spectrogram Inversion with Look-Ahead (RTISI-LA)

In recognising the above-described issues with RTISI, Zhu et al. modified the algorithm to utilise information of future frames to create the current frame [170]. To achieve this, a frame buffer is used as presented in Figure 6.2b. The buffer contains all frames overlapping with frame m , frame m itself, and K future frames (with $K = 0$, RTISI-LA equals RTISI). While processing is still done frame-by-frame, the whole frame buffer is used in the overlap-add step of the original RTISI algorithm, enabling the current frame m to be generated with partial information about future frames $m + n$.

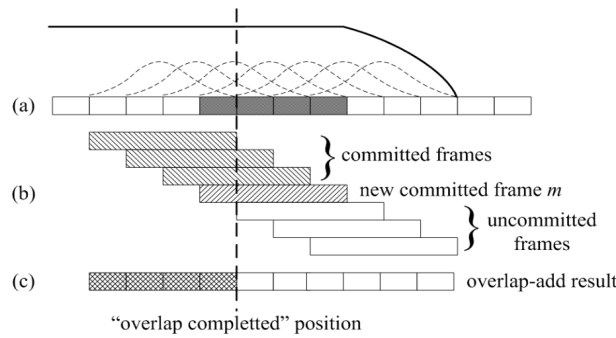


Figure 6.2: "RTISI with Look-Ahead after committing frame m . (a) Constructed signal with the indication of the contour (solid line) and overlapped windows (dashed line). (b) The frames are processed in the frame buffer. There are three types of frames in the buffer: frames committed in the previous process, the newly-committed frame m and the uncommitted frames. (c) The overlap-add result of the frames in the buffer. The shaded part is the 'overlap completed' signal" [170, Fig. 3].

The framework of the algorithm is presented in Figure 6.3. Notably, during each iteration of frame m , all future frames up to and including $m + K$ are also individually updated. To initialise frame $m + K$, the phase from frame m before iteration is used.

In evaluating the algorithm, it is found that with few iterations, the performance is similar to the original RTISI. It differentiates itself after more iterations with a continued growth of the SNR. The SNR is also generally larger than the results of GLA.

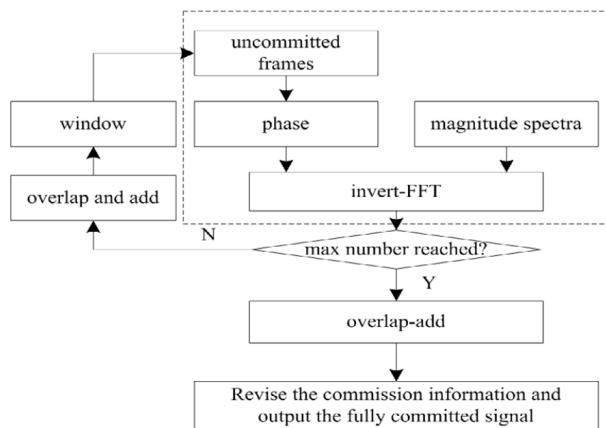


Figure 6.3: Flowchart of the RTISI-LA algorithm [170, Fig. 4].

6.1.3. Abdelmalek, Mnasri and Benzarti Iterative Algorithm

In an attempt to improve upon RTISI, Abdelmalek, Mnasri and Benzarti [167] employ the knowledge about the phase-magnitude relation of the STFT found by Portnoff [171]. They use the results from Shimauchi et al. [172] to estimate the initial phase for use in the RTISI algorithm instead of the originally used arbitrary phase. The algorithm for the time signal reconstruction is shown in Figure 6.4 [167, Fig. 4].

Most objective metrics used to compare with other signal reconstruction methods are worse for this new algorithm. In a subjective comparison, however, the authors found that the result from the proposed algorithm is preferred over RTISI and SPSI [167, Fig. 10].

6.1.4. Phase Gradient Heap Integration algorithm (PGHI)

Due to the iterative nature of the above algorithms, combined with their unknown convergence characteristics, non-iterative methods have been sought for signal reconstruction. Průša and Søndergaard [173] propose one prevalent algorithm based on the STFT phase-magnitude relationship, first introduced by Portnoff [171].

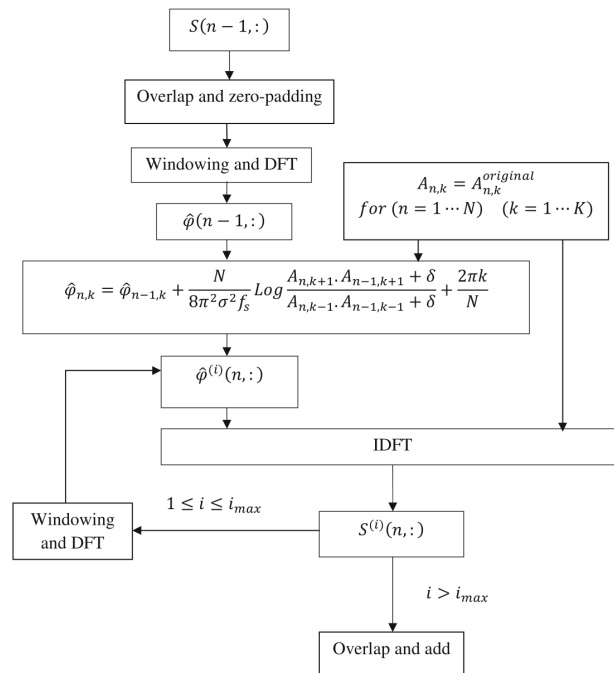


Figure 6.4: The algorithm proposed by Abdelmalek, Mnasri and Benzarti [167, Fig. 4]

This gradient is then integrated over the most prominent contours based on the magnitude of the spectrogram. A heap data structure (originally designed for the *heapsort* algorithm [174]) is used to efficiently keep the STFT points sorted as they are popped and added over the integration process. When some phase information is known, [173, Algorithm 2] can initialise the algorithm, increasing accuracy and computational cost. The authors suggest running the PGHI algorithm with a high tolerance tol and then rerunning with a low tol and the initialisation algorithm.

As a standalone algorithm, PGHI shows good convergence compared to the Single Pass Spectrogram Inversion algorithm (SPSI), introduced later. When used as the initial phase for the iterative methods presented above, PGHI provides a better initial estimate and, hence, better results than SPSI. Especially combined with I-BFGS and FGLA, the performance is very good. No comparison against the iterative methods without initialisation is presented.

Real-Time Phase Gradient Heap Integration algorithm (RTPGHI)

A downside of PGHI is that it cannot be used for real-time applications as it requires look-ahead capability. Průša and Søndergaard thus proposed RTPGHI to relieve this look-ahead requirement [175]. The phase gradient is determined similarly as above ([175, Eq. 13-14]) and used as an input. Most of the principles of PGHI are reused, but the part that requires a look-ahead in time is revised.

With a large enough window overlap, RTPGHI outperforms other state-of-the-art algorithms, with the compromise in larger compute times compared to SPSI. Compared to the iterative methods, compute time is reasonable for the favourable characteristics of the results.

6.1.5. Optimisation based algorithms

Some research groups consider signal reconstruction as an optimisation problem. Expanding on their 2011 findings, Decorsière et al. [176] identified a similar equation to the distance function of the Griffin and Lim algorithm [92, Eq. 4] as an objective function in the signal reconstruction problem [177, Eq. 4]. They then developed a method based on the limited memory Broyden-Fletcher-Goldfarb-Shanno (I-BFGS) [178] optimisation algorithm. One issue Decorsière et al. [177] recognise is the optimisation problem's size, with each point in the reconstructed signal being a dimension. This implies a quadratic scaling with signal length, which limits this algorithm to short signals or signals with sparse spectrograms.

Others, such as Waldspurger et al. [179], Candès et al. [180], Sun and Smith [181] and Balan [182] have developed similar methods that employ convex optimisation of the problem in matrix form. All of these encounter the same limitations as Decorsière’s method in terms of computational cost due to their quadratic scaling.

6.1.6. Other algorithms

Outside of the previously presented algorithms, others have been described in literature. These are presented in this section for completeness but are deemed not to apply to the auralisation in this thesis.

Bouvier and Ezzat designed an algorithm that treats signal reconstruction as solving a non-linear system of equations for each time frame [183]. An iterative solution strategy is suggested that initialises with samples from previous frames. The algorithm is only designed to work with rectangular windows, which cannot be guaranteed in this thesis. Hence, a more thorough discussion is omitted.

In 2015, Beauregard et al. proposed the Single Pass Spectrogram Inversion (SPSI) algorithm [184] as a low-resource alternative to the GLA and its variants. It is primarily inspired by phase vocoders with phase-locking around magnitude peaks, as presented by Laroche [185] and Puckette [186]. The phase rate at peak bins is estimated by interpolating the magnitude spectrum, as shown by Abe and Smith [187]. The SPSI algorithm is shown in Figure 6.5:

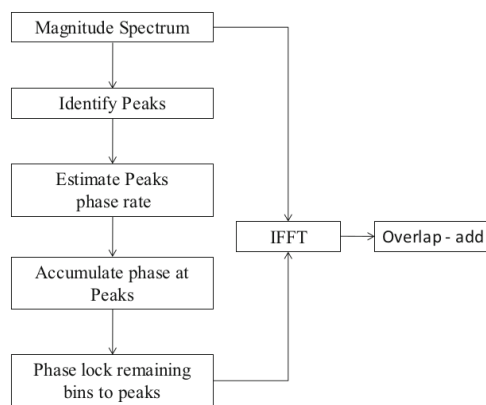


Figure 6.5: Single Pass Spectrogram Inversion (SPSI) [167, Fig. 2], adapted from [184, Fig. 2].

Similarly, Magron et al. [188] proposed an algorithm based on phase unwrapping. While following the same ideas as SPSI, it treats impulse-like components separately [167]. Since SPSI relies on using magnitude peaks for its phase estimation, which is not present in the spectra generated by HAWC2, these algorithms are not discussed further.

Lastly, Eldar et al. [189] presented a method to reconstruct a signal under the assumption that it is sparse in the original domain. In audio signal processing, this is found to be unrealistic [167], and this algorithm is thus not further elaborated on.

6.1.7. Random phase

While phase is recognised as an important component of sound in the spectral form [190], which is supported by the large variety of phase recovery methods presented above, an argument could be made that for specific sound signals, phase reconstruction is not of importance for the sound quality. Auralisation methods presented by Rizzi et al. [191]–[193] have limited the signal reconstruction to a random applied phase and a simple inverse Fourier transform. No literature is found that quantifies the difference in terms of psychoacoustics. Thus, a baseline case of random phase application is considered in the following methodology as a low-resource alternative.

6.2. Reconstruction Methodology

The process of reconstructing the sound signal is relatively simple, given the above algorithms. At this stage of the auralisation, the multiple sound spectra from the individual sound rays are to be summed first. Then, the signal can be reconstructed. This process is shown in Figure 6.6 and described below.

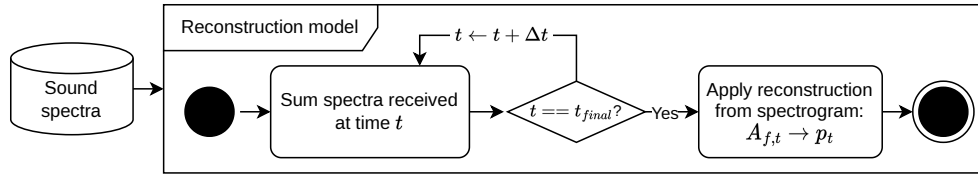


Figure 6.6: Flowchart of the reconstruction model.

A singular spectrogram must be established per receiver ear before applying the above methodologies. This is done by summing all received sound rays at equal time steps. Since interference can occur due to the ground reflections, incoherent summation of the sound spectra of the different rays is done. At each time step, a list of incoming sound spectra from the sound rays is stored per ear, each with a magnitude A_t^i and a relative phase $\Delta\phi_t^i$ spectrum. The total magnitude of all incoming sound is then determined as follows:

$$A_t = \left| \sum_i A_t^i e^{j\Delta\phi_t^i} \right| \quad (6.3)$$

Since the use of phase reconstruction in wind turbine auralisation has not been described in literature, a baseline is created with random phase reconstruction. This is done by applying a random phase to the above sound amplitude spectrogram, where the random phase is determined with the *Scipy* [91] function for random sampling on a uniform distribution. The limits of this uniform distribution are set to $-\pi < \phi \leq \pi$. Initially, the Griffin-Lim algorithm establishes if phase reconstruction positively influences the final sound signal. Further phase reconstruction algorithms can be considered based on the GLA results.

Since the reconstruction algorithms are purely mathematical, there is no assurance that the energy from the spectrogram is maintained in the final signal. Therefore, after reconstruction, conservation of signal energy is ensured, using Parseval's theorem, as described by Equation 6.4. No further corrections are needed, as the spectra from *HAWC2* are pressure spectral densities. Hence, no conversion from power spectral density is to be considered.

$$\frac{1}{N} \sum_{i=0}^{N-1} |X_i|^2 = \sum_{i=0}^{N-1} |p_i|^2 \quad (6.4)$$

In reconstructing, the inverse Fourier transform is used per spectrogram timestep. High levels of overlap and windowing are applied to these time segments to achieve a smooth signal. With more than 50% overlap, one has to scale the window, as they only allow for overlap of two signal segments when reconstructing. This is illustrated in Figure 6.7.

With the large amounts of overlap, this project applies a different system to quantify this overlap. Instead of defining the percentage of overlap over the next and previous frames, the overlap, o , is defined by the number of points in the Fourier transform N_{FFT} compared to the number required for the given Δt and sampling frequency. This new overlap parameterisation is defined in Equation 6.5:

$$N_{\text{required}} = f_s \cdot \Delta t \quad (6.5a)$$

$$N_{\text{FFT}} = o \cdot N_{\text{required}} \quad (6.5b)$$

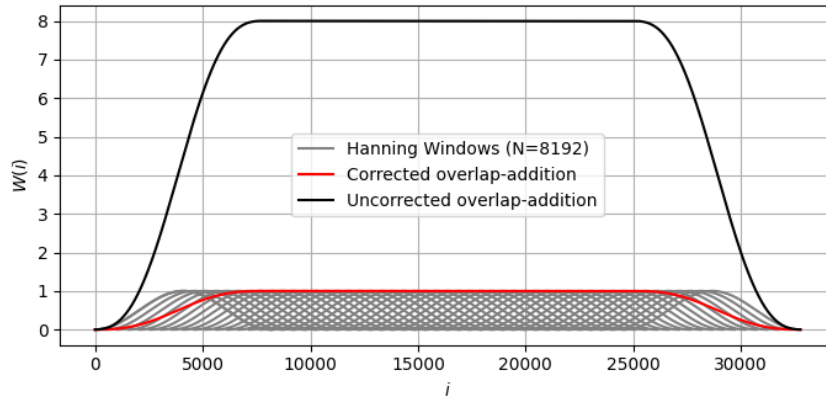


Figure 6.7: Illustration of window correction for overlap-addition with large overlap amounts.

To illustrate how this overlap parameter works, some examples of converting the conventional overlap amount to the new parameter o are given:

$$50\% \rightarrow o = 2$$

$$100\% \rightarrow o = 3$$

$$750\% \rightarrow o = 16$$

Coming back to Figure 6.7, the scaling s_w is easily defined in terms of this overlap factor by Equation 6.6:

$$s_w = \max\left(1, \frac{o}{2}\right)^{-1} \rightarrow W_{\text{scaled}} = s_w \cdot W \quad (6.6)$$

7

Implementation of WinTAur

In the previous chapters, individual parts of the auralisation toolchain have been discussed, and methodologies for each of them have been presented. This chapter focuses on implementing and integrating the partial methodologies to achieve the research objective.

The toolchain is implemented in the *Python* programming language [126], version 3.11.3. Multiple external modules are used, of which the most relevant are: *NumPy* [122], *SciPy* [91], *Pandas* [194], *webb* [195], *compress-pickle* [196]. The resulting code is called the *Wind Turbine Auralisation tool(chain)*, abbreviated to *WinTAur*.

7.1. Software Implementation

This section covers the code implementation of the auralisation methodology. This work applies an object-oriented programming approach. The tool is summarised in the diagram in Figure 7.1. The starting point of the tool is the project directory containing a set of input files and a *HAWC2* model.

The input files are Unicode text files with `.aur` file extension. These files are structured similarly to a *HAWC2* `.htc` input file. This file contains the necessary parameters to run both the *HAWC2* simulations, the propagation model and the reconstruction model. Details of the input file structure can be found in the *README* file of the *GitHub* repository¹ of *WinTAur*. The *HAWC2* model should contain everything needed to run a simulation. A `.htc` file containing everything except the wind and noise blocks should also be in the model directory. It should be ensured the model works outside of the auralisation toolchain before running the noise simulations.

The tool starts with a prompt to enter the name of a project directory. The *Project* class reads this directory and initialises a *Case* class instance for each `.aur` file. The *Project* instance then starts by running the cases. The toolchain's first part is running a *HAWC2* simulation. This is the most computationally expensive part, depending on the demanded resolution of the sphere input in the simulation. After the *HAWC2* simulation, the classes for the different models are initialised. Then, per reception point, the models are run in the order shown in the diagram. The logic underlying these models is explained in the following subsections. They are presented in order of implementation, and notes about challenges encountered during this implementation are made.

7.1.1. Propagation Model

The first part of the auralisation toolchain implemented is the propagation model described in chapter 4. The diagram in Figure 7.2 shows the workflow of running the propagation model. Firstly, a time limit for propagating the rays is determined to limit the compute time. This is set at three times the sound travel time from the turbine hub to the receiver point. Then, all sound rays are propagated according to the logic described in subsection 4.2.1.

¹Available on: https://github.com/spockele/thesis_code

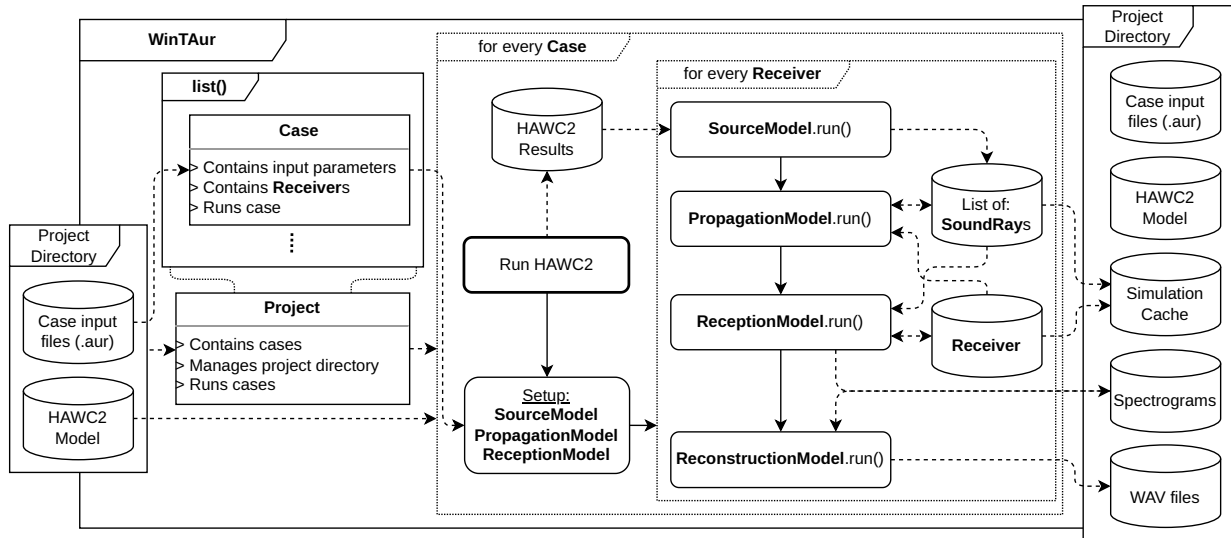


Figure 7.1: Diagram summarising the flow of information in WinTAur.

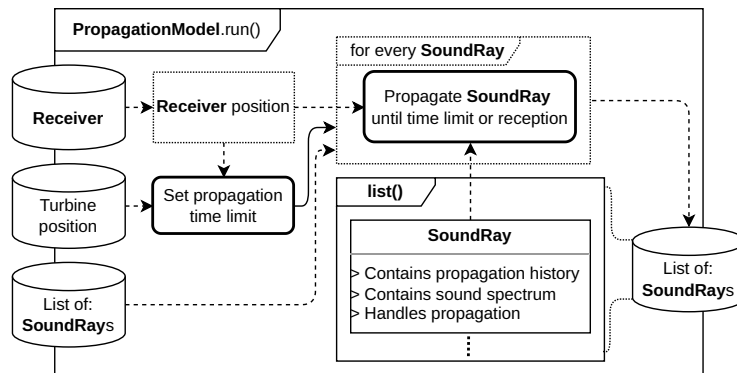


Figure 7.2: Diagram summarising the flow of information in the propagation model implementation.

The propagation effects are calculated according to the description in subsection 4.2.2. The ground effect is calculated after the ray is fully propagated due to the reliance on information about the full propagation path. The remainder of the propagation effects is calculated at each time step, as established in the methodology. The speed of sound used in Equation 4.17 of the ground effects calculations is the speed of sound at 20°C, $c = 343$ m/s.

After implementing the frequency-dependent sound propagation effects, i.e. ground reflections and atmospheric absorption, it is found that applying these effects to an octave band spectrum results in audio subjectively very different from experimental recordings. This can be explained by the fact that, especially for ground interference, the interference pattern only affects narrow frequency bands. This means some effects are not captured in the octave bands, while others are applied to a full octave band. To avoid artefacts resulting from this mismatch in frequency resolution, the spectra from the HAWC2 results are interpolated linearly to the frequency resolution of the HRTF function used in the binaural rendering. While this resolution is still relatively low, it is deemed adequate for the desired sound quality. The effect of the interpolation resolution should be investigated further to ensure it does not affect the objective sound quality metrics.

At the initial implementation stage of the ground reflection model, the phase spectrum of the sound rays is initialised as zero for all frequencies and timesteps. This zero-phase initialisation inherently assumes that the phase of the noise from all sources is coherent at emission, which does not make sense for aerodynamic noise caused by turbulence. This phase coherence causes a significant ground interference

pattern in the generated spectrograms. This interference pattern is not observed in the spectrograms of the validation recordings of an actual turbine. This discrepancy confirms the assumption that noise caused by turbulence can be considered incoherent with a randomised phase at emission. For this reason, the phase spectra of the sound rays are initialised with a random spectrum sampled from a uniform distribution with limits $-\pi < \phi \leq \pi$, through *Scipy* [91]. This random phase added at the source level significantly reduces the severe interference pattern. Regarding the subjective experience with the sound, the noise could be described as ‘tinny’ and ‘plastic cuppy’ when the phase was initialised as zero. Adding the random phase initialisation removed these sounds, and the noise is subjectively much closer to the recordings.

7.1.2. Source Model

The second part of the implementation involves the source model. The overall logic of Figure 3.1 is followed, with some details adapted to ease the implementation. The workflow of this model, shown in Figure 7.3, starts with the *HAWC2* simulation results. These are interpolated to the simulation time steps to simplify the further processes. The calculated wind turbine noise is stored per simulation observer point through the *H2Sphere* class into instances of *H2Observer*. An instance of the *Source* class is initialised for each blade position in time. These source instances generate the initial sound rays according to the methodology described in section 3.2. These rays are then stored in a list and passed on to the propagation model.

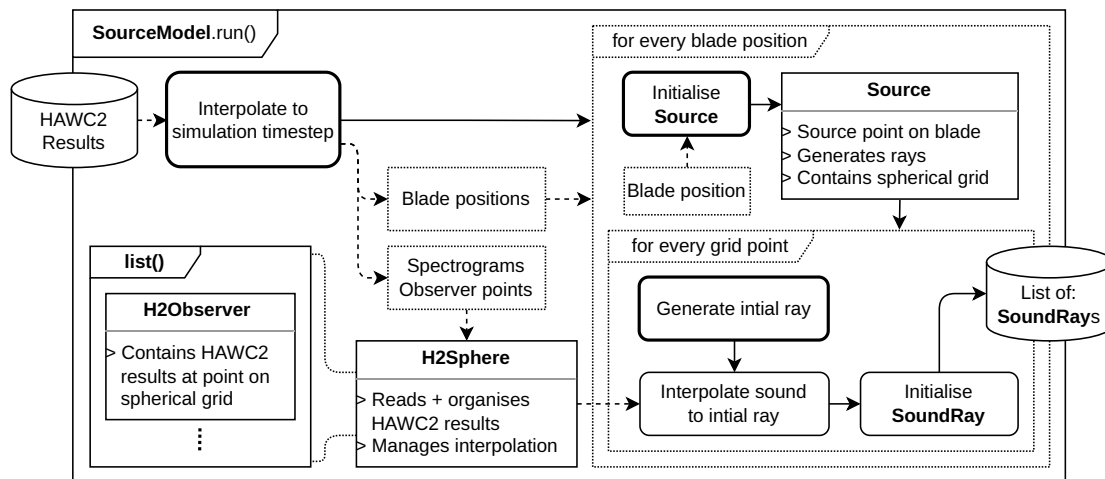


Figure 7.3: Diagram summarising the flow of information in the source model implementation.

The source model was originally implemented with a single spherical grid to draw the initial sound rays for all three blades. This spherical grid was on the same sphere as the *HAWC2* results but with the option to have a larger resolution. While interpolation was required, the initial rays required less calculations. It has a significantly less complex code implementation than what is finally used but results in undesired amplitude fluctuations. These are caused by the Gaussian beam tracing relying on a grid with uniform angular spacing. This is not the case in the originally conceived source model, where the uniform spacing on the *HAWC2* result sphere results in larger beam widths on the side where the blade source point is close. This, in turn, results in certain sound rays being received at elevated levels in relation to their distance from the receiver. Ultimately, this resulted in subjectively unrealistic results, with large fluctuations. The source model, as proposed in this thesis, eliminates this issue.

To improve compute time, the number of rays generated is limited to those strictly necessary for the simulation. The filtering to generate the correct rays is based on the angle from the source point towards the receiver point. Rays are only generated when their initial direction is within 25° of the direction towards the receiver.

The simulation in *HAWC2* is expected to be run with a larger timestep than the ray tracing and final spectrograms. To enable this discrepancy, linear time interpolation of the *HAWC2* results is implemented with the *NumPy* [122] *interp* function. This interpolation also involves the angular position of the turbine blades.

These angular positions are limited in the range $[0, 2\pi[$ radians, with a numerical discontinuity going from 2π to 0 radians. During interpolation, this angular discrepancy results in one of the blades jumping a full rotation between two *HAWC2* time steps. For example, with a *HAWC2* timestep $\Delta t_{H2} = 0.04$ s and a ray tracing timestep $\Delta t_{RT} = 0.01$, the angular position would go as follows:

$$\psi(t \rightarrow t + \Delta t_{H2}) : 2\pi - \delta \rightarrow \frac{3\pi}{2} - \frac{\delta}{2} \rightarrow \pi \rightarrow \frac{\pi}{2} + \frac{\delta}{2} \rightarrow 0 + \delta \quad (7.1)$$

The effect of this discrepancy is sudden jumps in noise levels in the resulting spectrograms and sound files. These jumps in level are so significant that the audio is unusable as wind turbine noise. The solution to this issue is found in the *NumPy* [122] *unwrap* function, which can eliminate large value jumps in a time series of angles. After this interpolation issue is fixed, no unexpected artefacts from the source model are present in the auralised noise.

During the implementation of the coordinate systems, a misinterpretation occurred in creating the cylindrical coordinate system. In its current form, the *HAWC2* aerodynamic model azimuth angle is offset. The zero azimuth direction, when looking at Figure A.1, is in the negative z-direction in the Cartesian system, corresponding to $\psi = +90^\circ$. This misinterpretation is only found after implementing the complete toolchain due to subjective errors in the audible output. Due to time constraints, the cylindrical coordinates are not modified. Instead, the azimuth from *HAWC2* is adjusted.

7.1.3. Reception and Reconstruction Model

The last required part to complete the auralisation tool is the reception and signal reconstruction, as described in chapter 6. The reception model also contains the binaural rendering from chapter 5. The implementation, shown in Figure 7.4, starts with the list of sound rays and the instance of the *Receiver* class. Each sound ray is checked for reception, followed by the extraction of sound information at the reception point. This information is fed into an instance of *ReceivedSound*, which stores the information temporarily and applies the binaural rendering if selected. These received spectra are ordered per received time step to be summed into the final spectrogram. The final spectrogram is stored in the *Receiver* instance. The signal reconstruction implementation consists of inverting the spectrogram and storing the signal as a *WAV* file.

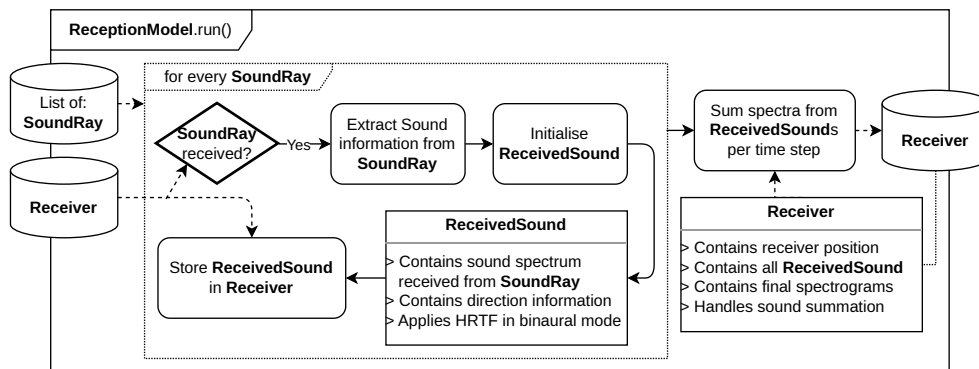


Figure 7.4: Diagram summarising the flow of information in the reception model implementation.

With the established equations and parameters to calculate the interaural time delay, this delay is on the order $ITD \sim 10^{-4}$ s. With an established simulation timestep $\Delta t = 10^{-2}$ s, also used for reception and the final spectrograms, a lot of interpolation would be required to apply the interaural time delay to the individual received sound spectra. Due to time and computational constraints in the project, it is decided to apply the ITD in a relatively simplified manner. Instead of determining the incoming angle of each sound ray and applying the corresponding time delay before the signal reconstruction, the time delay is determined based on the relative position of the wind turbine hub and applied to the reconstructed time signal of the ear, which is furthest away from the turbine. This simplification might warp the directional experience of the binaurally rendered sound, which is recognised as a limitation at this stage.

While the tool should eventually auralise a full *HAWC2* time series, the current implementation limits the reconstruction to the periodic repetition of one rotor rotation. The main driver for this choice is the requirement for limited compute time due to the project duration. The signals per rotation are overlap-added with a fitted Tukey window to achieve a smooth signal. While the validation analysis could be done with short signals representing one rotor revolution, using longer signals averages the background noise to avoid influences of short disturbances.

The results from signal reconstruction with an implementation of the GLA deteriorated in subjective quality as more iterations of the algorithm were run. Unfortunately, the *iSTFT* function in *SciPy* [91] is not an exact inverse Fourier transform, which the author did not know at the time of implementation. The function is an implementation of the GLA, which explains the deterioration in quality after running it multiple times. While this work technically does not apply the signal reconstruction algorithms from section 6.1, the GLA is used through *SciPy* with random phase initialisation.

The discrete Fourier transform requires enough data points to reconstruct the signal to achieve the desired sampling frequency. For this work, a sampling frequency $f_s = 51.2$ kHz is selected with a simulation time step of $\Delta t = 0.01$ s. By Equation 6.5a, at least 512 points are required in the DFT per time step. To achieve an acceptable signal quality, an overlap $o = 16$ is needed, thus resulting in $16 \cdot 512 = 8192$ DFT data points per time step. To achieve this requirement, interpolation is done during the signal reconstruction phase. Initially, it was planned to fill the octave bands with white noise, but linear interpolation is deemed more appropriate considering the results from Bertagnolio, Madsen and Fischer [31].

7.2. Verification

Throughout the implementation, individual parts of the code are verified. Since the proposed methodologies are based on well-established literature, models are verified against data available in their respective literature sources. For some models, such as ray tracing, verification against literature data is too complex for the scope of this work. These complex models are unit-tested with straightforward cases for which the governing equations are solved exactly.

The models that are unit-tested are the following: the ray-tracing logic, the implementations of the coordinate systems described in Appendix A, functions related to geometry and trigonometry, the implementation of the ISO Standard Atmosphere [121], and all functions implementing singular equations.

One model implementation that is explicitly verified against data in literature is the atmospheric absorption model by Bass et al. [83]. The equation used to replicate their plot is

$$\bar{\alpha}(f, \Delta s = 100 \text{ m}) = 20 \log_{10} \left(e^{100 \cdot \alpha(f)} \right) \quad (7.2)$$

Figure 7.5 displays minor discrepancies in areas where the graphs overlap significantly, but these are attributed to errors in the digitisation of the figure in Bass et al. [83, Fig. 1] rather than implementation errors.

The ground reflection model implementation is compared against two sources: the original paper by Embleton, Piercy and Daigle [81] and the implementation by Arntzen [86]. Figure 7.6 shows minor discrepancies between the current implementation and the original work. It is found, however, that the original figures are severely deformed, and the digitisation is thus far from perfect. The current implementation matched well with the comparison against the expected values from Arntzen [86] in Figure 7.7.

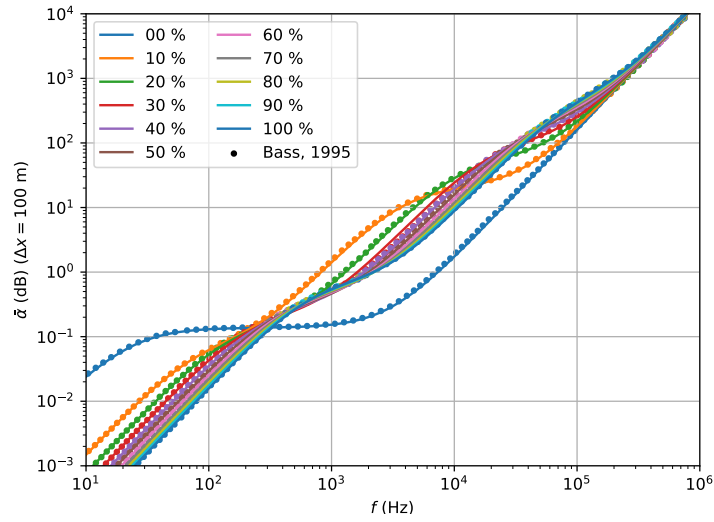
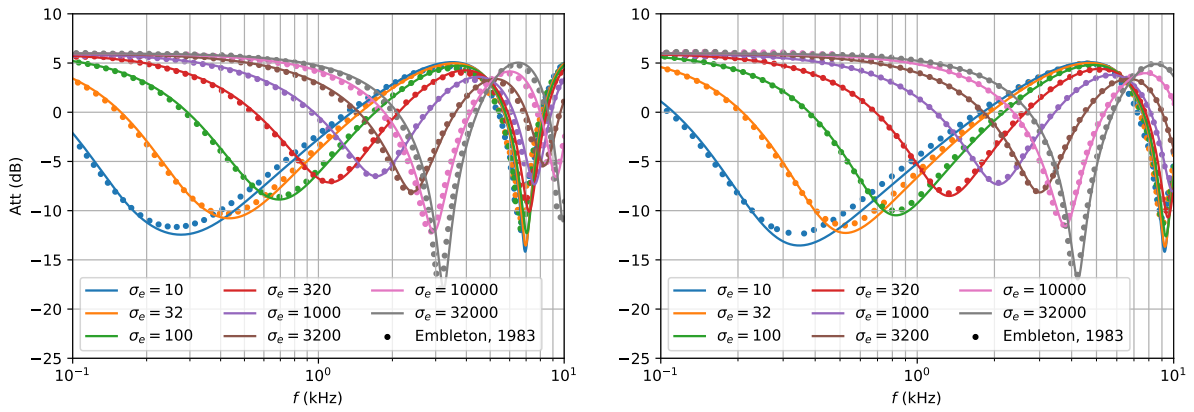


Figure 7.5: Plot comparing the current implementation of the atmospheric absorption with expected values.



(a) Source and receiver heights 0.31 m and 1.22 m, and horizontal separation of 15.2 m [81, Fig. 2]

(b) source and receiver heights 0.31 m and 0.46 m, and horizontal separation of 7.62 m [81, Fig. 3]

Figure 7.6: Comparison of the current implementation of the ground reflection model with expected values.

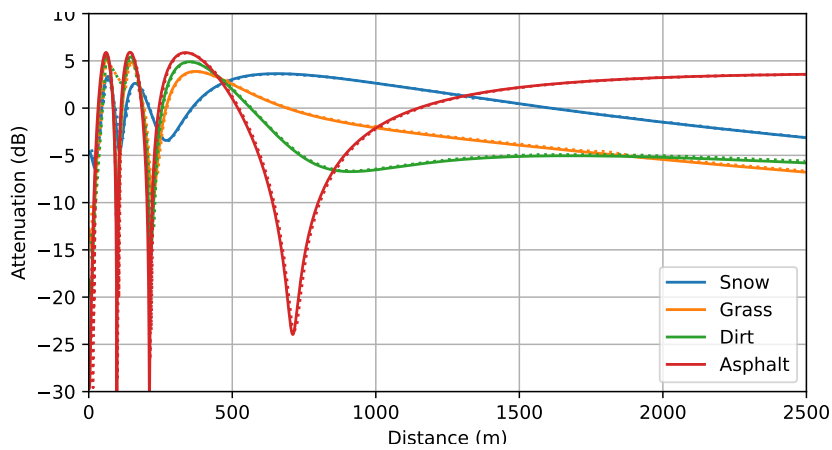


Figure 7.7: Comparison of the current implementation of the ground reflection model with expected values.

8

Numerical Validation

This chapter of the report covers the validation of WinTAur through numerical means. The first section covers the setup of the validation cases. The experimental setup, data selection and simulation setup are described. The second section describes the validation with sound quality metrics. This is done since this thesis focuses on application in psychoacoustics. Lastly, a spectral analysis is performed to aid in understanding possible sources of discrepancies.

8.1. Case Study Setup

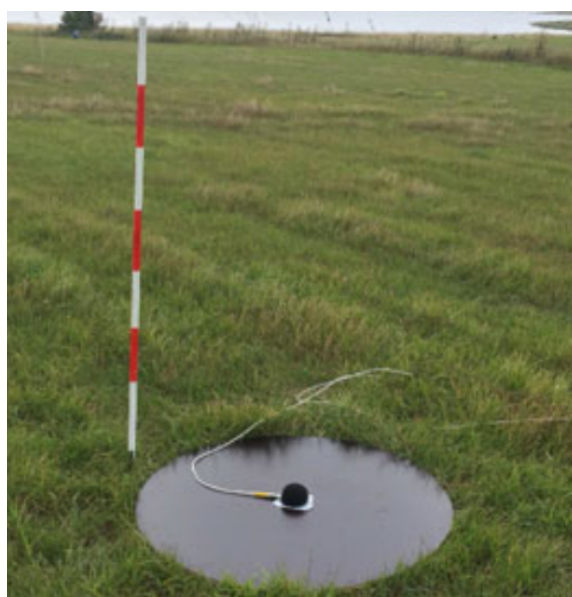
This section describes the case study setup to validate *WinTAur*. The experimental setup used for obtaining the noise measurements is described first, followed by the case selection for the validation. Lastly, the execution of the simulations and data processing is covered.

8.1.1. Experimental Setup

The wind turbine used for validation is a *Nordtank NTK 500/41* wind turbine located on foundation four at the DTU Risø campus in Roskilde, Denmark. The turbine is a traditional Danish, three-bladed, stall-regulated wind turbine with a capacity of 500 kW and a rotor diameter of 41 m, pictured in Figure 8.1a. This wind turbine has been extensively studied and tested, making it ideal for validating the presented tool. Most importantly, a validated model for *HAWC2* simulations [31], [197], [198] is available for this study.



(a) The *Nordtank NTK 500/41* wind turbine [198, Fig. 2].



(b) The microphone setup [199, Fig. 2].

Figure 8.1: Experimental setup for validation.

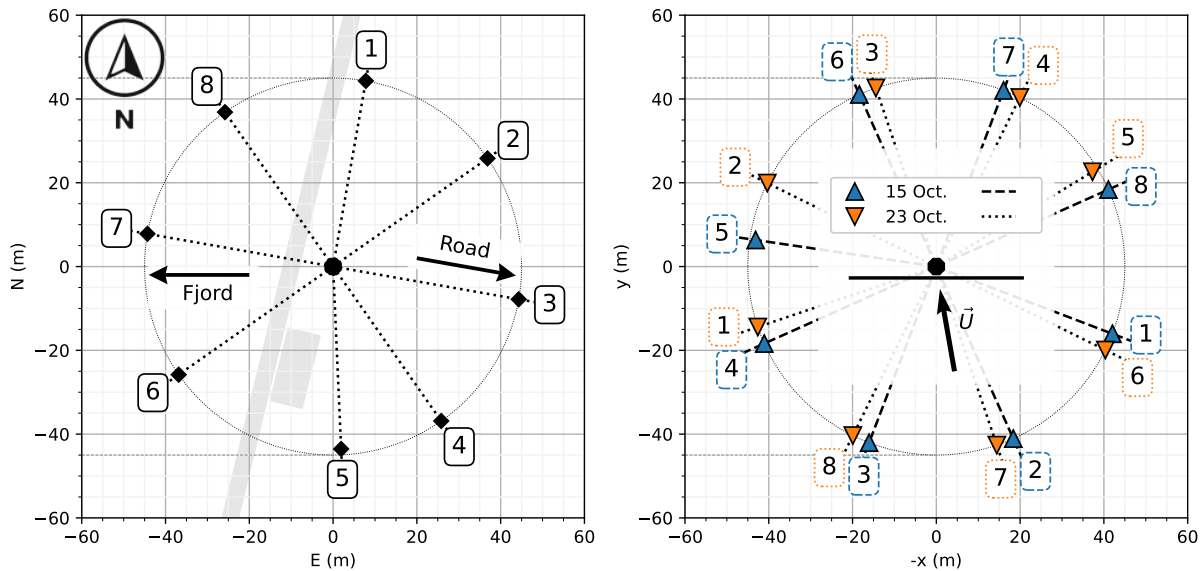


Figure 8.2: Positions of the microphones around the wind turbine. Left: absolute positioning, right: positioning relative to rotor plane.

The setup used to obtain the operational data consists of a 36 m meteorological mast at 2.5 rotor diameters to the west of the turbine, instrumentation to monitor the turbine's operating parameters, and a PC-based data acquisition system to record the data in 16 bits at 35 Hz. Noise measurements are made with eight microphones manufactured by *BSWA Technology Co.* (ref. MPA 261 combining a 1/2" microphone and a pre-amplifier) set up around the turbine at a 45 m distance from the turbine. They are set up on plywood boards with a primary windshield but no secondary windshield, as shown in Figure 8.1b. The positioning around the turbine is displayed in Figure 8.2. In the left plot, the access road and a shed are shown in light grey [31], [199].

One missing parameter in the dataset from Bertagnolio et al. [199] is the air humidity, which is required as an input of the atmospheric absorption model in subsection 4.2.2. Hourly relative humidity measurements by *Danmarks Meteorologiske Institut* (DMI) [200] are supplemented in the dataset through linear interpolation.

8.1.2. Case Selection

In the first stage of case selection, the wind turbine operational data is looked at, which is summarised in Tables B.2, B.4 and B.3. Cases where the wind turbine is changing operational state (ramping up or down), no significant electrical power is produced during operation, or cases with significant yaw changes are not used as they cannot be simulated with the current, steady-state version of the code.

In some of the remaining noise measurements, audible disturbances are noted. This is acceptable for a time-averaged spectral analysis but would cause issues with sound quality metrics in the assessment. Therefore, spectrograms of the pressure spectral level are objectively inspected, and samples with visible disturbances are eliminated. A subjective listening inspection is done in cases where disturbances are doubted.

During the subjective inspection, it was noted that the measurements on October 15th were dominated by background noise. Therefore, the time-averaged, A-weighted signal-to-noise ratio (SNR) of the two-minute simulations noise signal against the average background noise of the corresponding microphones is determined and plotted in Figure 8.3.

The subjective impression is confirmed, and a minimum SNR limit of 3 dB is set to filter cases highlighted in red. Based on this, all data from October 15th and most cases at microphone position five are eliminated. The final case selection is shown in Table 8.1. There are eight cases with the turbine in operation and five with the turbine turned off. The latter noise recordings are used as background.

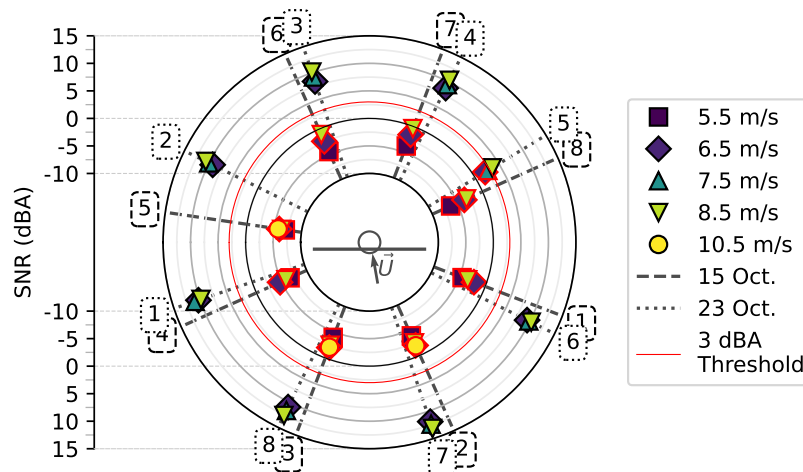


Figure 8.3: A-weighted signal-to-noise ratio (SNR) of the simulated cases.

Table 8.1: Summary of wind turbine data selected for validation [199], [200].

Timestamp	Turbine Status	Mean WS (m/s)	WS Bin (m/s)	Mean Rotor RPM	Mean Power (kW)	TI (%)	Temperature (°C)	Pressure (hPa)	Humidity (%)	Mean WD (°)	Mean yaw (°)
23 Oct. 15:12	off	9.45	9.5	-	0	8	12.16	1017	74	285	252
23 Oct. 15:34	off	8.97	8.5	-	0	5	12.17	1017	76	288	305
23 Oct. 15:36	off	8.77	8.5	-	0	4	12.17	1017	77	289	305
23 Oct. 15:50	off	8.11	8.5	-	0	7	12.13	1018	78	283	295
23 Oct. 15:52	off	7.58	7.5	-	0	5	12.10	1018	79	282	295
23 Oct. 15:18	on	7.91	7.5	26.9	164	8	12.18	1017	75	288	298
23 Oct. 15:20	on	8.79	8.5	26.9	197	9	12.17	1017	75	287	298
23 Oct. 15:22	on	8.44	8.5	26.9	201	5	12.22	1018	75	289	298
23 Oct. 15:24	on	8.85	8.5	26.9	237	8	12.24	1018	75	289	298
23 Oct. 15:42	on	6.58	6.5	26.8	94	4	12.15	1018	77	289	295
23 Oct. 15:44	on	6.46	6.5	26.8	83	3	12.09	1018	78	291	295
23 Oct. 16:00	on	7.53	7.5	26.9	139	5	12.08	1018	80	286	295
23 Oct. 16:02	on	7.58	7.5	26.9	148	6	12.09	1018	80	287	295

8.1.3. Simulation Setup

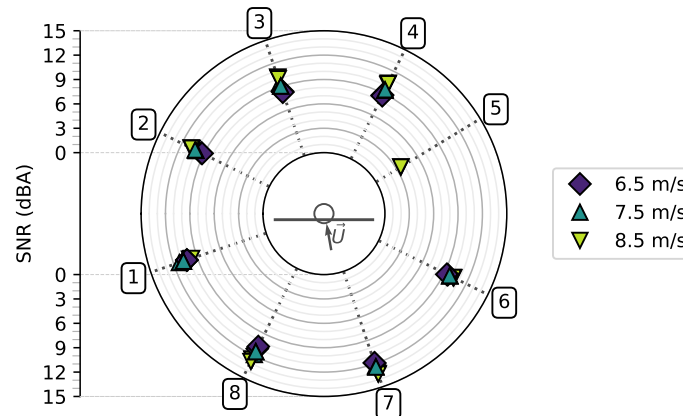
The simulations use the operational parameters from Table 8.1. However, other parameters are required that are independent of the case. Due to time constraints, a sensitivity analysis of these parameters is not feasible within this study. The parameters are set according to Table 8.2, where the values are chosen as a compromise between compute time and a subjective assessment of the results. The output duration and sampling frequency are determined based on the description of the noise recordings by Bertagnolio et al. [199]. All signals are created without the binaural rendering described in chapter 5 since the noise measurements are not recorded binaurally. The ground type for the reflections is set to be grass, as it is the most prevalent in the test area.

Table 8.2: Case independent WinTAur simulation parameters selected for validation.

	Number of rays per source	Source location on blade	Radius of <i>HAWC2</i> sphere
Source Model	1024	$0.85R$	$1.1R$
	Output sampling frequency	Overlap o	Output audio duration
Reconstruction Model	51.2 kHz	16	120 s

After running the simulations, background noise is added to the noise signals to allow for a good comparison with sound quality metrics. It is found that the experimental recordings are not at the indicated 51.2 kHz, requiring resampling to match the simulation outputs. Background noise samples are matched randomly to the simulation cases per microphone position.

Before the sound quality metric analysis, the SNR is revisited and plotted for the remaining cases in Figure 8.4. There is a slight dependence on the wind speed, which is expected as Bertagnolio et al. [31] show a higher wind turbine noise level at higher wind speeds, thus increasing the SNR. There is no significant dependence on the microphone position, except at position five. The source of this low SNR is not known, but the presence of a shed right next to the microphone could be an explanation. This low SNR is kept in mind throughout the analysis, as it may explain discrepancies.

**Figure 8.4:** A-weighted signal-to-noise ratio (SNR) of the selected cases.

8.2. Sound Quality Assessment

The sound samples generated with the above setup are analysed with the Sound Quality Assessment Toolbox for MATLAB [201], [202]. The toolbox determines the statistics of the sound quality metrics for the full 120 second files. The following subsections cover the analysis of loudness, sharpness, roughness, fluctuation strength, tonality and psychoacoustic annoyance. As established, the plots only present cases with an SNR above 3 dBA, thus only the ones from October 23rd.

In the assessment, microphones three and seven are the reference directions for upstream and downstream, respectively. Similarly, microphones one and five are the respective references for left and right. The just-noticeable-difference (JND) lines in the difference plots show the JND percentages presented by Osses, Greco and Merino-Martinez [203, Tab. 1], multiplied by the mean metric value of the measured noise at each microphone position. The complete analysis below is based on the mean values of the sound quality metrics as representative values for the sound samples. In all cases and for all metrics, the simulations have lower result values than the measurements. Thus, the positive values in the plots in this section all represent the measurements having the higher values for the different metrics.

8.2.1. Loudness

Loudness (N) is a metric to measure a sensation of intensity. While sound pressure levels are important for this metric, the tonal content also significantly affects the human sensation of intensity. A loudness of 0 sone represents noise at the human threshold of hearing, and 64 sone represents a perceived intensity equivalent to a 1000 Hz tone of 100 dB [25]. The typical loudness range is 0 through 120 sone [203].

Firstly, Figure 8.5 presents the loudness of the measured wind turbine noise of the selected cases. Given the range between 7.5 and 15.0 sone, Fastl and Zwicker [25, Fig. 16.1] indicate the noise intensity is between a bird twitter and normal conversation. Given the increasing sound pressure levels, the consistent increase in loudness in Figure 8.5 with wind speed is expected.

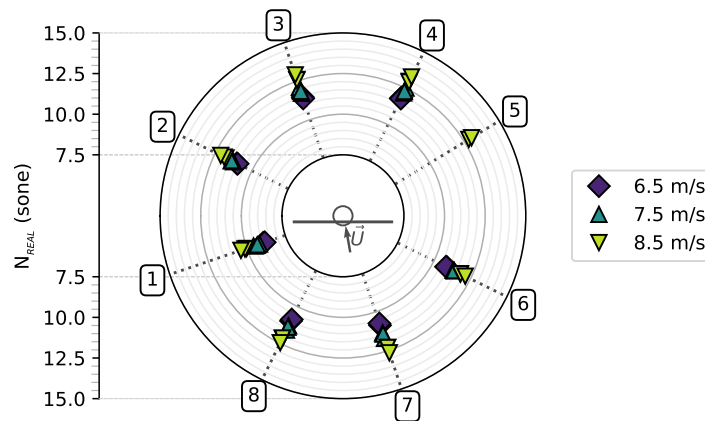


Figure 8.5: Loudness of the measured noise (N_{REAL}).

Figure 8.6 shows the difference in loudness between the simulation results from *WinTAur* and the measurements. The differences are consistently outside the range of just noticeable. For the downstream positions, microphones two through four show similar differences, whereas the cases at 8.5 m/s show larger differences than at other wind speeds. The increasing dominance of stall noise with wind speed for a stall-controlled turbine can explain this trend as it is a known limitation of *HAWC2*.

The upstream differences are generally more minor than the downstream ones. The results at position seven stand out, as they show the most minor differences. This is not unexpected given that Bertagnolio et al. [31] mainly validate the aeroacoustics model at this position. Looking at section 2.2, the difference between the upstream and downstream results can be explained by the lack of turbulence scattering in the propagation model, combined with the more considerable turbulence in the wake of the turbine. While the propagation distance in this validation is relatively small, the lack of wake modelling in the wind speed used in the ray tracing may also explain this upstream-downstream difference. The lower SNR at position five does not significantly affect the results.

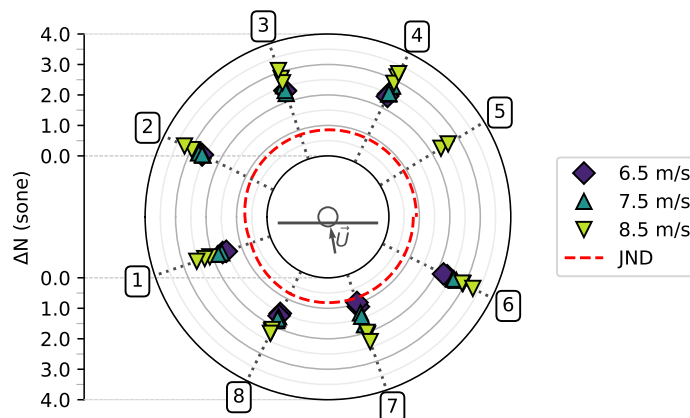


Figure 8.6: Difference in loudness (ΔN) between *WinTAur* simulations and measurements.

8.2.2. Sharpness

Sharpness (S) measures a timbre sensation related to the spreading of the frequency content and the comparative presence of high- to low-frequency components. The typical range of sharpness is 0 through 10 acum [203]. The sharpness of the measured noise, in Figure 8.7, is in a small range from 1.1 to 1.6 acum. The upstream values are closer to the bottom of this range, the downstream values are in the middle, and the left and right-hand positions are in the upper part of the sharpness range. Based on the directionality analysis by Bertagnolio et al. [31, Fig. 12], which shows a larger ratio of high- to low-frequency components and narrower spectra on the left and right sides of the turbine, this is an expected result. Otherwise, there is little difference in values between the presented wind speeds, which is also expected from the validation of *HAWC2* [31].

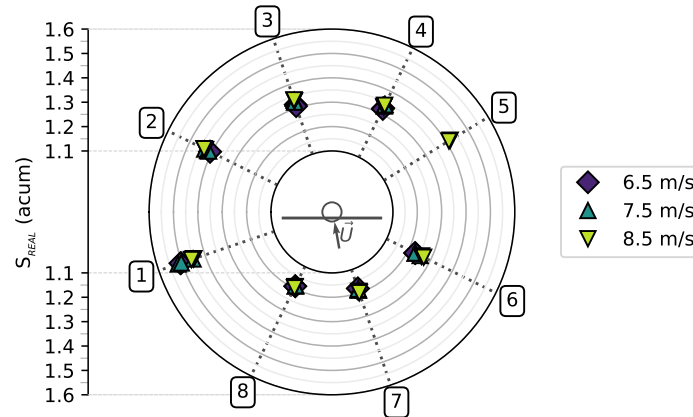


Figure 8.7: Sharpness of the measured noise (S_{REAL}).

The upstream sharpness deltas in Figure 8.8 match well between simulations and measurements, as they are inside the JND range for the lower wind speeds. At the other microphone positions, the deltas are larger and significantly outside the JND range. Similar to the loudness, the results at 8.5 m/s show generally larger differences between simulation and measurement, which can also be related to the stall noise as it primarily affects the high-frequency range of the noise spectra [31].

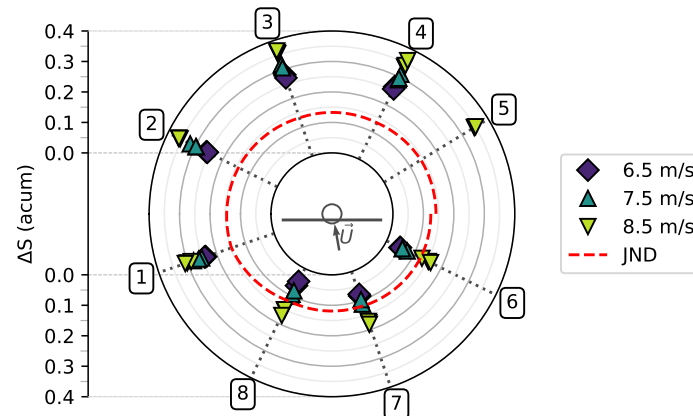


Figure 8.8: Difference in sharpness (ΔS) between WinTAur simulations and measurements.

8.2.3. Roughness

The roughness metric (R) characterises a timbre sensation related to rapid amplitude or frequency modulations at a rate of order 15 – 300 Hz. It is expressed in asper, with values ranging from 0 to 3.2. Figure 8.9 shows the roughness of the measured noise is very low with a maximum of 0.075 asper. The values are least spread out on the upstream side and most on the turbine’s left side. Wind speed is related to roughness, where the 8.5 m/s cases stand out again.

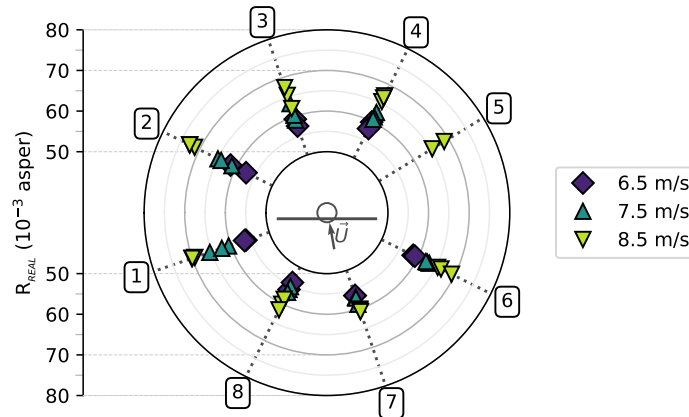


Figure 8.9: Roughness of the measured noise (R_{REAL}).

The deltas in roughness are lowest up- and downstream of the turbine and largest on the left side of the turbine. There is also a relation with wind speed, where the 8.5 m/s cases stick out again for having larger differences than the others. When normalised with the corresponding values in Figure 8.9, the wind speed relations in Figure 8.10 disappear, but the differences between microphone positions remain, showing the difference in roughness is mostly related to the discrepancies in directivity from *HAWC2*.

Considering the overlap amount of $\sigma = 16$ in the reconstruction, combined with the spectrogram timestep of 0.01 s, modulations at a rate of 6.25 Hz are the fastest modulations unaffected by the overlap addition. The amplitude and frequency modulation is only resolved at 25 Hz by the 0.04 s timestep in *HAWC2*, adding to the possible explanation of the difference in roughness. The simulation results have a lower roughness value than the recordings, which adds to the plausibility of this explanation. A solution should be found to lower the overlap and simulation timesteps, but a sensitivity analysis should be done to prove this hypothesis.

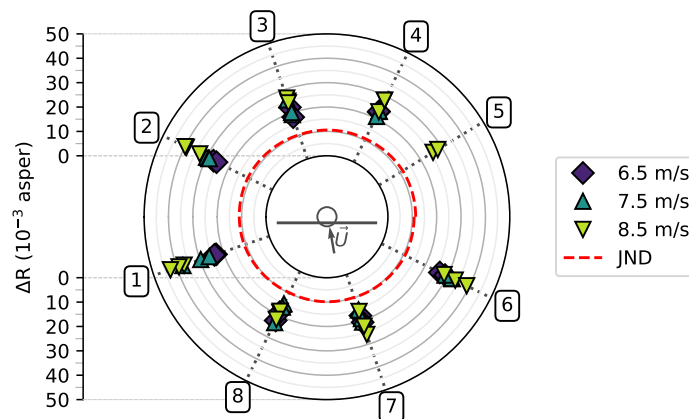


Figure 8.10: Difference in roughness (ΔR) between WinTAur simulations and measurements.

8.2.4. Fluctuation Strength

The fluctuation strength (FS) metric measures slow amplitude and frequency modulations with a rate below 20 Hz. This metric is critical in wind turbine noise, as slow modulations are a significant factor in public perception [26], [204]–[207]. Considering the blade pass frequency (BPF) of the *NTK 500/41* turbine is 1.4 Hz, the fluctuation strength is significant. Figure 8.11 shows the values for this metric are in the order of 0.1 vacil, which is relatively low in the typical range of 0 to 3 vacil, defined by Osses, Greco and Merino-Martinez [203]. A significant difference is noted between the microphones on the left and right and the microphones up- and downstream. Observers closer to the rotor plane are expected to experience more significant modulations, as they are right underneath either the down- or upstroke of the blade. A relation between wind speed and fluctuation strength is complex to establish.

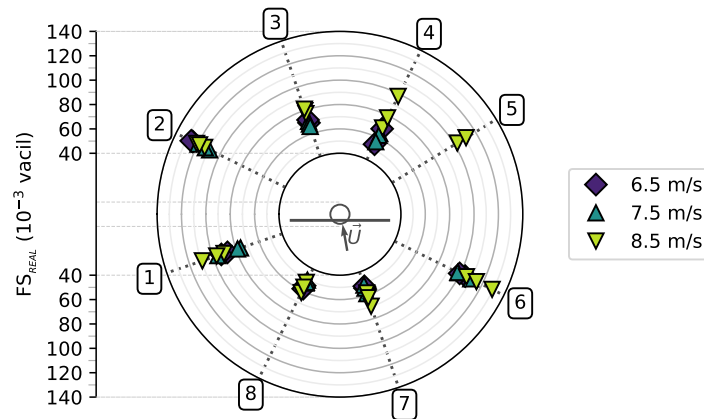


Figure 8.11: Fluctuation strength of the measured noise (FS_{REAL}).

The differences between simulation and measurements in Figure 8.12 show minimal relation with wind speed. Variations at the different observer positions seem case-dependent, with no clear indication of what plays a role. The most minor discrepancies are found up- and downstream, which does not come unexpectedly with lower fluctuation strength at those positions. The downstream differences are more significant than upstream, indicating the lack of wake modelling may again play a role. On the left side, microphone one shows a significantly different behaviour from the other side position microphones, but no clear explanation can be given.

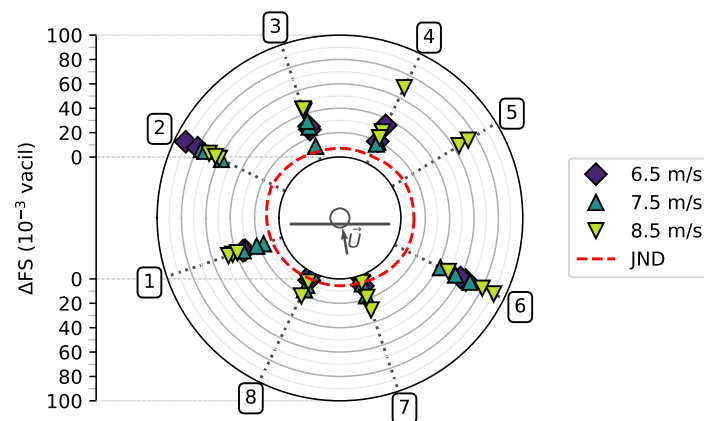


Figure 8.12: Difference in fluctuation strength (ΔFS) between WinTAur simulations and measurements.

8.2.5. Tonality

A measure of the amount of tonal content, the tonality (K), is expected to have insignificant values, given the broadband nature of wind turbine noise. Figure 8.13 confirms this hypothesis, with the maximum value of 0.035 tonality units (t.u.) significantly lower than the maximum possible value of 1 t.u. There is some inverse relation with wind speed, where cases at 8.5 m/s are again outliers compared to the other speeds. The directional effect is mainly a difference in the spread of tonality over the wind speeds.

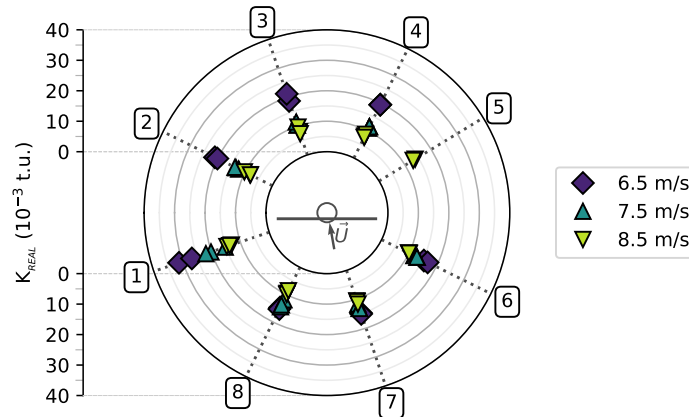


Figure 8.13: Tonality of the measured noise (K_{REAL}).

The differences between *WinTAur* and experimental recordings in Figure 8.14 show that the simulations are accurate at generating the same tonality in some instances. Since *HAWC2* does not predict tonal components, this analysis is expected to primarily be affected by the background noise, thus not adding much value to the discussion.

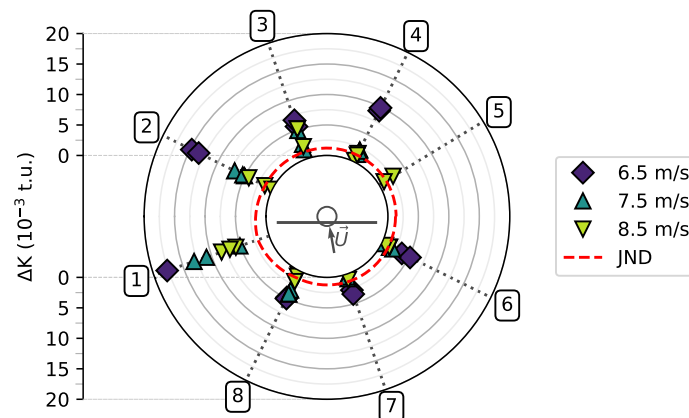


Figure 8.14: Difference in tonality (ΔK) between *WinTAur* simulations and measurements.

8.2.6. Psychoacoustic Annoyance

Lastly, the overall psychoacoustic annoyance (PA) is a summarising metric for all the above metrics. For this analysis, the definition by Fastl and Zwicker [25] is used, as the addition of tonality by Di et al. [208] is not relevant to the low tonality range. The values of psychoacoustic annoyance in Figure 8.15 repeat the overall story of the sound quality metric analysis. Wind speed has some influence, with the 8.5 m/s cases different from the other wind speeds. The main factor affecting the psychoacoustics is the position around the turbine.

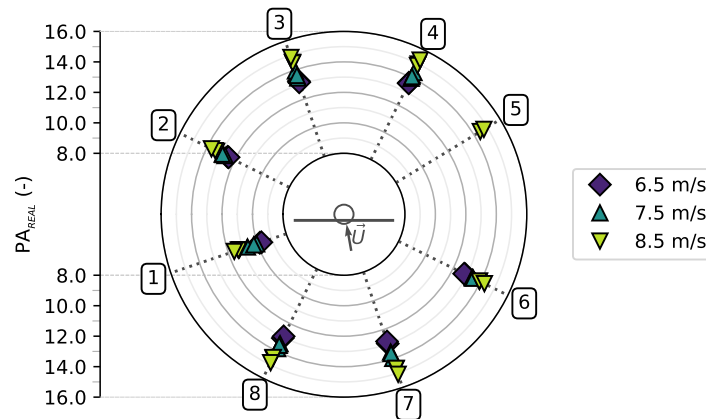


Figure 8.15: Psychoacoustic annoyance of the measured noise (PA_{REAL}).

Regarding the difference between simulated and measured noise, the 8.5 m/s sticks out in Figure 8.16, but not as significantly as some other metrics. Microphone position seven shows the most minor differences, and the left and right sides show the most significant differences. The simulations work best at the location where *HAWC2* is most intensively validated. The directional discrepancies presented by Bertagnolio et al. [31] are reflected in a directional change in the difference in most metrics.

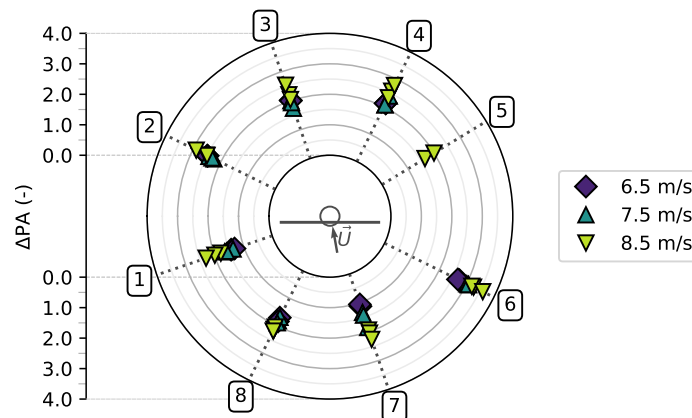


Figure 8.16: Difference in psychoacoustic annoyance (ΔPA) between WinTAur simulations and measurements.

8.3. Spectral Analysis

A better understanding of the discrepancies from the previous section is sought in a more technical spectral analysis. Different parts of the auralisation toolchain are examined to find possible sources of discrepancy. First, the Gaussian beam tracing is validated against *HAWC2* results at the microphone positions. Then, the influence of the propagation effects is investigated, followed by a spectral validation of the entire toolchain. This section only presents spectra of the difference between the different samples for each case (e.g., the difference between *HAWC2* and the Gaussian beam tracing). The spectra of each sample of each case are kept in Appendix C.

8.3.1. Gaussian Beam Tracing Validation

For this validation, *WinTAur* is run with all propagation effects, but the spherical spreading is deactivated. No background noise is added to the sample either. The difference between *WinTAur* and *HAWC2* are plotted in Figure 8.17. Firstly, an attenuation in the low-frequency range is found with a minimum of -10 dB. This discrepancy may pose an important issue since Bertagnolio et al. [31] found *HAWC2* to underpredict the low-frequency noise. An explanation can be found in the Gaussian beam reception Equation 4.21c, where a mathematical error is found in the denominator of the frequency-dependent term. This should have been $c^2/(\pi f \delta \alpha)^2$, meaning the lower frequencies are probably over-attenuated. Since this is found too late to be fixed in this work, the effect of correcting Equation 4.21c should be investigated in future work.

Next to the low-frequency attenuation, the delta shows a sawtooth pattern, for which an explanation cannot be given. A pattern different from the other positions is found at microphone one, with significant amplification between 40 Hz and 200 Hz. The low-frequency attenuation at this position is also less. Given that the Gaussian beam tracing is mostly within 6 dB from spherical spreading, the method is highly effective in predicting noise levels for a simple propagation case.

8.3.2. Influence of Propagation Effects

The influence of adding the propagation effects from subsection 4.2.2 is also investigated to understand better the final validation of the *WinTAur* results. Figure 8.18 shows the plots of this analysis. The ground effect has the largest influence in the low frequencies, while the atmospheric absorption dominates in the high frequencies.

The plots show an amplification of 2 to 5 dB in frequencies up to 2000 Hz. Because the microphones in the experiment are mounted on plywood boards, the reflective amplification is expected to be closer to a perfect reflection of 6 dB. Therefore, in this validation setup, the ground reflection is identified as a probable source of discrepancy in the low-frequency range. Based on the verification plots in Figure 7.6, this discrepancy is not expected to be very large depending on the exact absorption properties of the plywood boards, as reflections are rarely perfect.

As expected from the plot of the Bass et al. [83] model in Figure 7.5, the effect of atmospheric absorption is most prominent in the high-frequency range. There is no significant difference in attenuation between the different cases, which the slight differences in atmospheric conditions in Table 8.1 clearly explain. The microphone positions show no significant differences in the effect of atmospheric absorption, indicating its directional independence.

8.3.3. Toolchain Validation

With the additional understanding of the influence of different parts of the *WinTAur* propagation model, the overall results are presented in Figure 8.19. The low frequencies up to 100 Hz are not considered for this analysis as strong tonal components are present in the recordings. This is visible in the plots in Appendix C. Given the operating rotor RPM combined with the gearbox ratio, mechanical noise is expected to be present in the range from 25 to 60 Hz, which is the case. Looking at the peaks in Figure 8.19 in this frequency range, a large, tonal under-prediction from *WinTAur* is found.

In the frequencies between 100 and 2000 Hz, all *WinTAur* show a consistent attenuation of 2 to 6 dB with some tonal discrepancies. Based on the above discussion about the ground reflections, this discrepancy is likely due to the wrong choice of ground type for this validation. A strong disagreement between the simulations and recordings is found between 2 and 10 kHz. It is consistently more significant for the cases with a wind speed of 8.5 m/s, indicating this may be caused by stall noise. Notably, this discrepancy is almost not present at the upstream microphones (seven and eight), which matches the description of bad high-frequency directivity prediction of *HAWC2* by Bertagnolio et al. [31].

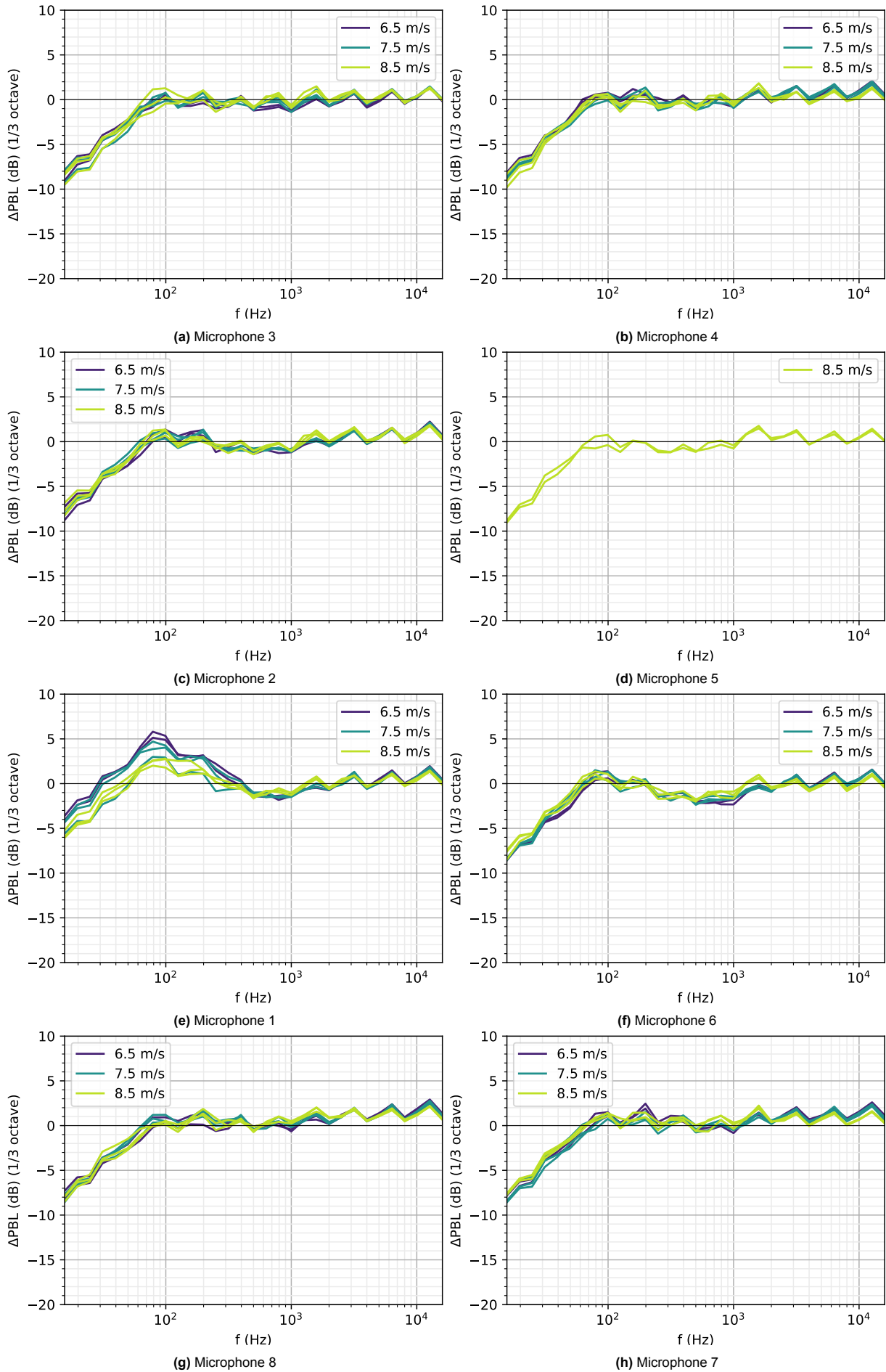


Figure 8.17: 1/3 Octave band level differences between the Gaussian beam tracing and *HAWC2*'s propagation.

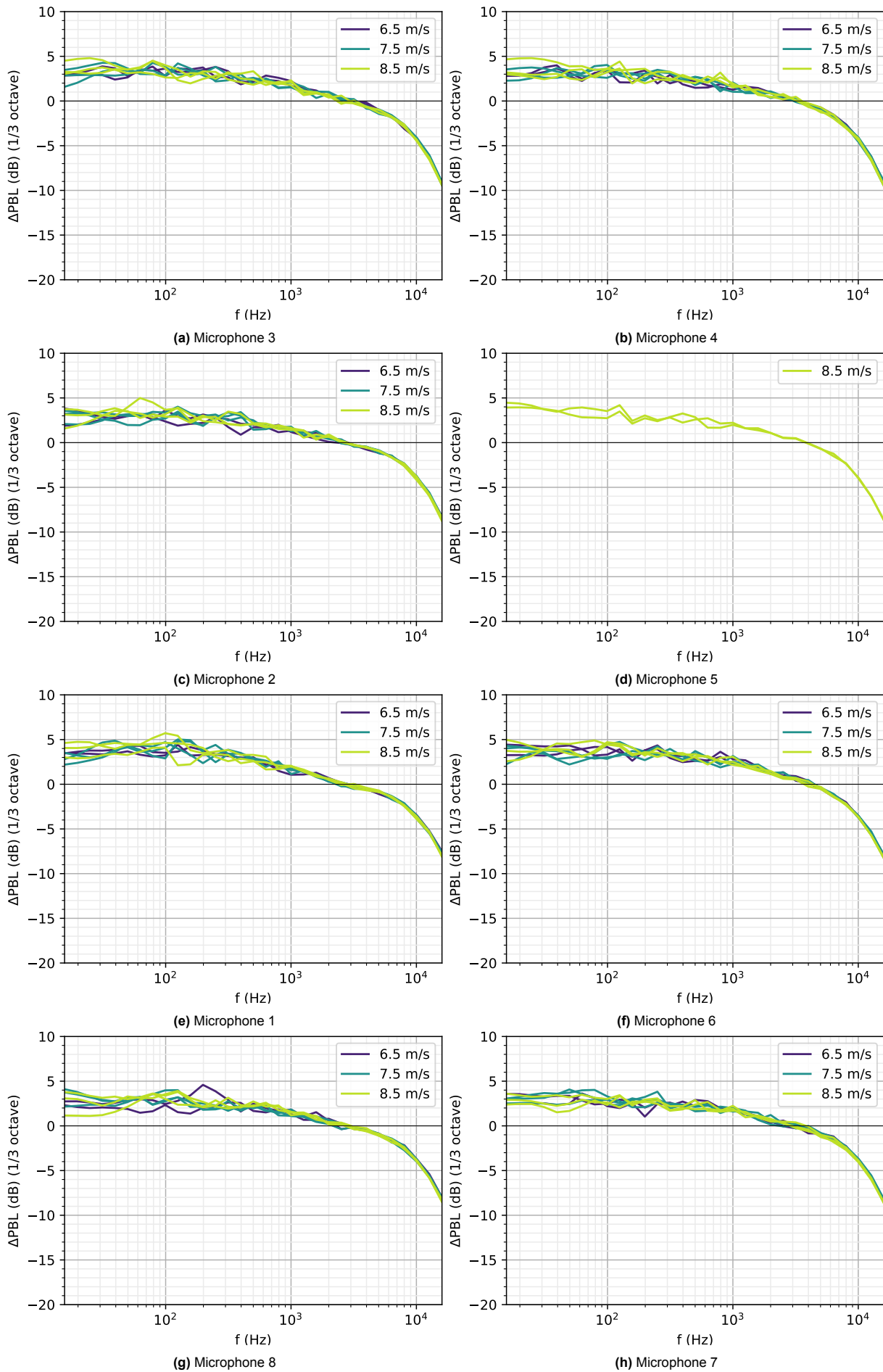


Figure 8.18: 1/3 Octave band level differences between WinTAur with all propagation effects and WinTAur without.

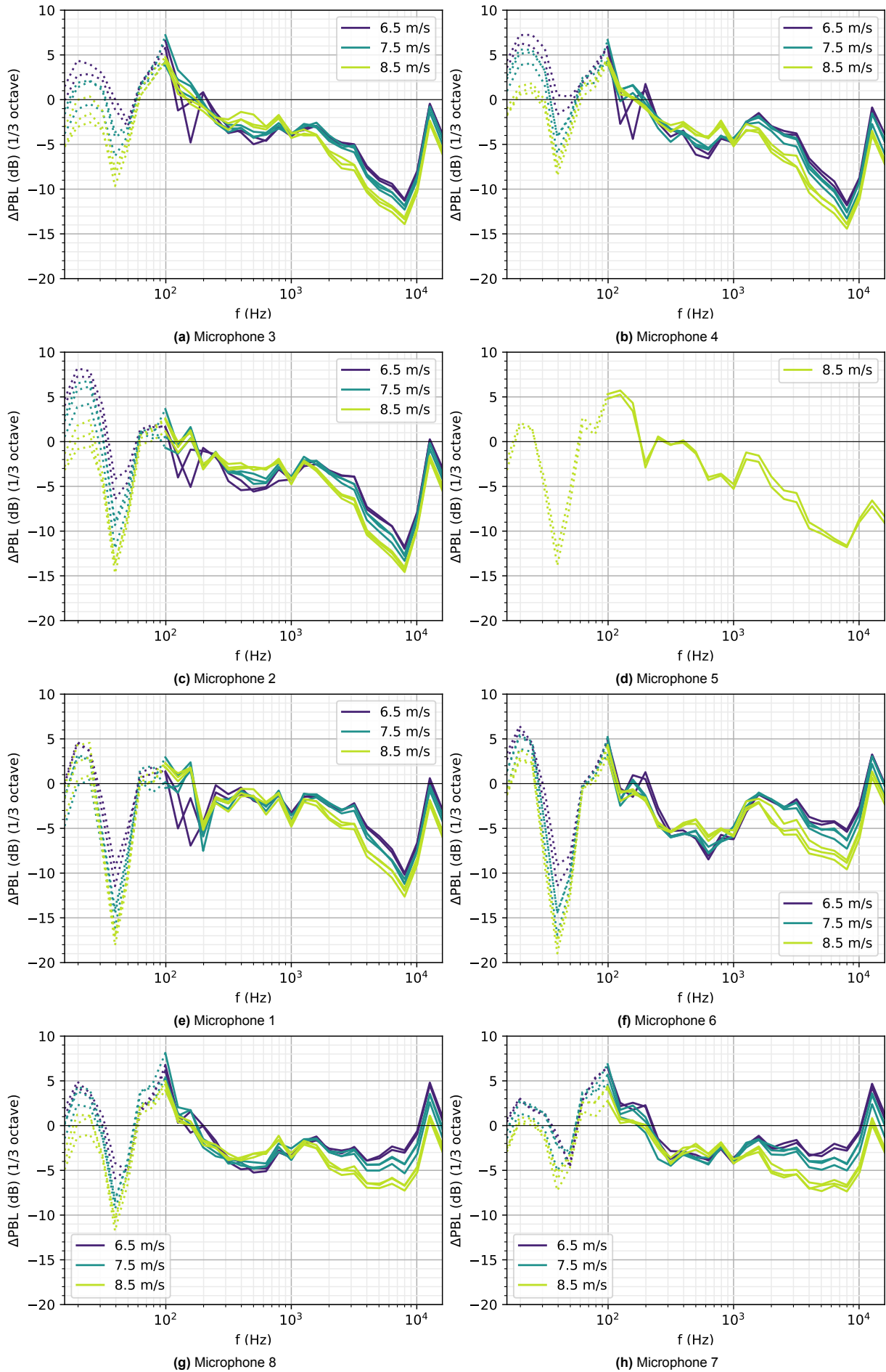


Figure 8.19: 1/3 Octave band level differences between WinTAur simulations with BGN and experimental recordings.

9

Listening Experiment

With the numerical validation of WinTAur showing significant differences between recorded and simulated wind turbine noise, it is decided to run a listening experiment to validate the tool in a subjective setting. The experiment in this work is loosely based on the work by Susini, McAdams and Winsberg [209], Parizet et al. [210], [211], Rossi, Crenna and Codda [212], and Alamir et al. [213].

9.1. Test Setup

The listening experiment is run in the Psycho-Acoustic Listening Laboratory (PALILA) at the Delft University of Technology, Aircraft Noise and Climate Effects Section [214]. PALILA is a box-in-box concept, soundproof booth inside a dedicated room at the TU Delft Aerospace Engineering Faculty, with an interior square plan form of 2.32 m by 2.32 m, and 2.04 m height. The walls, floor and ceiling are built from double-walled, modular bricks of two 19 mm MDF panels, separated by 52 mm acoustic-absorbing, agglomerated polyurethane foam and fibres, made out of recycled denim and upholstery. There is a single door made of the same panel composition, which has a soundproof seal. The floor and ceiling are covered in a 50 mm layer of acoustic-absorbing foam. The booth is separated from the building floor through a damping system, where the hollow space is filled with sound-absorbing foam. The walls and ceiling are further covered in rounded square shapes, made from felt-like fibre to provide an almost-anechoic environment. In two diagonally-opposed corners, bass traps are placed to dampen low-frequency sound further.



Figure 9.1: Test setup for the listening experiment inside PALILA.

Sound reproduction is done with a pair of *Sennheiser HD 559* [215], open-back, around-ear headphones. They are connected to a *HP Elitebook 850 G1* [216] notebook computer running the user interface. The user interface is created in *Python 3.8.10* [126], using the *Kivy 2.2.1* [217] GUI development platform. Sound is played through the *Kivy* integration of *GStreamer* at the 30% volume setting of the computer.

At the start of each experiment, participants are informed about the thesis topic and how the listening experiment is coupled with the research. Then, they are seated, asked to silence their phones, and adjust the headphones to a comfortable fit. The interface and question procedure are introduced. For the first two sections of the experiment, participants are explicitly asked to compare their feelings and experiences with the sound samples rather than focusing on the sound details. Finally, they are informed about the experiment's expected duration and how to leave the listening room. After the experiment, participants are informally asked about their impressions of the experiment, the findings of which are summarised below.

9.1.1. Sound Sample Selection

Similar to the method of case selection in the numerical validation, the recording samples and corresponding simulations are chosen subjectively. Since the number of cases should be limited to keep the listening experiment at a reasonable length, only three cases are selected. The decision is also made only to use cases from October 23rd since the wind turbine noise has an A-weighted SNR above zero, meaning it is audibly at higher levels than the background noise. The latter is done to increase the effect of the wind turbine noise on the participants' perception. The selected cases for the listening experiment are presented in Table 9.1. The first two cases gauge the perceptual differences between the experimental recordings and WinTAur simulations. The last case is used to investigate the human perception of the difference with different propagation effects turned on or off and is also used to test the binaural rendering.

Table 9.1: Summary of wind turbine data selected for the listening experiment [199], [200].

Timestamp	Turbine Status	Mean WS (m/s)	WS bin (m/s)	Mean Rotor RPM	Mean Power (kW)	TI (%)	Temperature (°C)	Pressure (hPa)	Humidity (%)	Mean WD (°)	Mean yaw (°)
15:24	on	8.85	8.5	26.9	237	8	12.24	1018	75	289	298
15:44	on	6.46	6.5	26.8	83	3	12.09	1018	78	291	295
15:58	on	7.70	7.5	26.9	151	7	12.07	1018	79	285	295

9.1.2. Questionnaire for Participant Statistics

At the start of the experiment, participants are asked to fill out a questionnaire to record population statistics and to gauge possible hearing impairments. The interface used for this questionnaire is shown in Figure 9.2. Table 9.2 presents the questions and answers used to establish the nature of the population sample. These statistics could highlight bias towards certain parts of the population if it exists. On the other hand, the questions in Table 9.3 are used to explain possible outliers in the dataset.

We start with a few questions about you.
These answers are collected anonymously.

Age:

Current gender identity:

Highest completed level of school/education:

Current employment status:

How would you rate your attitude towards wind turbines?

Have you ever heard a wind turbine before this experiment?

Are you currently suffering from any ear disease?

Have you had an accident that affected your hearing?

Do you use a hearing aid?

How did you find out about this experiment?




Figure 9.2: Screen capture of the questionnaire interface.

Table 9.2: Questionnaire items related to gathering statistics of the population sample of the experiment. The left column is the question asked; the right column presents the options for participants.

Population statistics	
Age	Filled by participant
Current gender identity	Prefer not to say Woman Man Non-Binary Agender Other
Highest completed level of school/education	Prefer not to say Elementary (Kindergarten through primary school) Some High School (No Diploma) High School Graduate Some College, but No Degree Bachelor’s Degree Master’s Degree Doctorate
Current employment status	Prefer not to say Employed for wages Self-employed Homemaker Student Retired Out of work or unable to work
How did you find out about this experiment?	Posters Information screens Social media TU Delft website Brightspace Other

Table 9.3: Questionnaire items to establish possible outlier results. The left column is the question asked; the right column presents the options for participants.

Participant Parameters	
How would you rate your attitude towards wind turbines?	Very Positive Positive Neutral Negative Very Negative
Have you ever heard a wind turbine before this experiment?	Yes No
Are you currently suffering from any ear disease?	Yes No
Have you had an accident that affected your hearing?	Yes No
Do you use a hearing aid?	Yes No

9.1.3. Comparison Between Recordings and Simulation

After the questionnaire, participants will be given 20 questions to gauge the realism of the auralised noise. They will be presented with two sound fragments of seven seconds, with a two-second break in between. After listening to both fragments, participants are asked to rate the difference on a scale from 0, meaning functionally the same, to 4, meaning completely different. Each sample is presented twice to the participants. Participants are offered a short break to refocus every five questions during this experiment section. The interface mandates seven seconds, but participants can wait longer before continuing.

The user interface during these questions is shown in Figure 9.3. There are four distinct steps, where Figure 9.3a is the screen initially presented to the participants. Figure 9.3b shows the interface while listening to a sound sample, followed by the screen in Figure 9.3c, where the participant can answer the question. Finally, the interface in Figure 9.3d is shown when a question is finished, and the participant can continue to the next question.



Figure 9.3: Cropped screen captures of the interface for the first and second set of questions.

9.1.4. Influence of Propagation Effects

In the second listening part of the experiment, participants are presented with the same type of question as the previous one. Instead of comparing recordings and simulations, participants are given two simulation samples with different propagation effects. The various combinations of effects are presented in Table 9.4. Each combination is presented twice. The interface used is the same as in the previous part, with the same exposure duration for the different sound samples. A break is given every four questions instead of five, as the difference between samples is significantly smaller than in the first listening section.

Table 9.4: Selection and naming of comparisons in the second listening section of the experiment.

	None	Ground effect	Atmospheric absorption	Both
None		none - ground	none - atm	none - all
Ground effect	ground - none			ground - all
Atmospheric absorption	atm - none			atm - all
Both	all - none	all - ground	all - atm	all - all

9.1.5. Binaural Effect

During the last listening section of the experiment, the effectiveness of the binaural rendering module is tested by presenting the participants with eight spatially rendered samples. Four directions are given to the participants: directly in front (0°), directly behind (180°), to the left (270°) and the right (90°). Each direction is presented twice. Participants then are asked to judge the direction on an eight-point wind rose, as is shown in Figure 9.4. The concept of the question procedure is similar to the one presented for the previous two listening sections, except for the different answer scale.

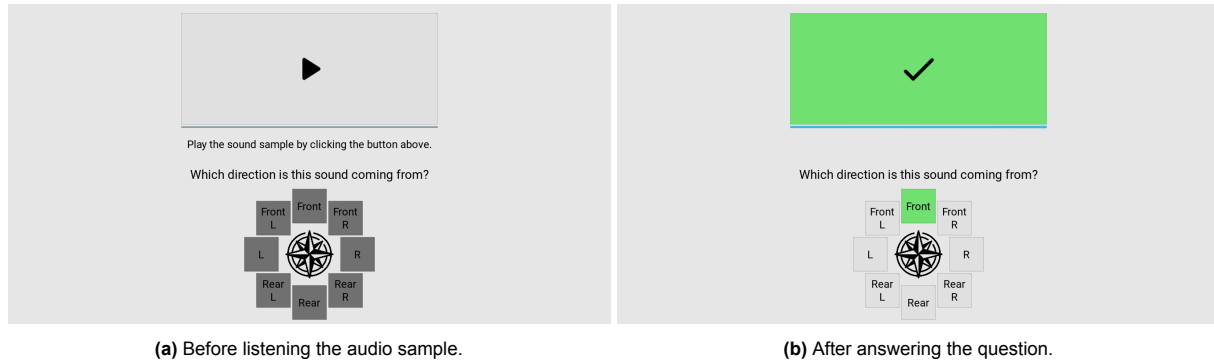


Figure 9.4: Cropped screen captures of the interface for the third set of questions.

9.1.6. Expected Limitations

Some limitations of the experimental setup are thought out before analysing the data. Firstly, the order of the samples is the same for all participants. Each participant is expected to require a few questions to calibrate their responses on the difference scale; hence, the results will potentially be skewed. In further questions, their positioning in the question queue may also play a role that should be investigated. For this purpose, each combination of audio samples will be repeated twice, and these repetitions are to be compared against one another.

Another anticipated limitation is that there might be a large spread in difference ratings since the question and scale are entirely subjective. With this in mind, outlier filtering should not be done based on the common rules of thumb concerning the mean and standard deviation of the dataset. Instead, inspiration is taken from Boulet et al. [218], who used the Pearson correlation matrix to check for participants with response behaviour that could be considered an outlier. In this work, the participant's data is regarded as a significant outlier if the median of the participant's correlations is lower than the 16th percentile of all correlation values. This eliminates results outside of the 68% confidence interval.

9.2. Participant Statistics

The participants of this listening experiment are a convenience sample found through advertisements on the campus of TU Delft. Multiple calls for participants are made through different media: physical posters are hung in most faculty buildings, digital posters are shown in a few faculty buildings, a digital poster is placed on the Aerospace Engineering Brightspace page, and a poster is posted on multiple digital media. This yielded a sample representative of the overall university population [219], of which the statistics are shown in Figure 9.5.

In terms of gender, the ratio of men to women is roughly seven to three, with no one in the other gender categories. The attitude towards wind turbines is generally favourable, with no participants answering on the negative side of the spectrum. In the sample, more participants indicated they had been exposed to wind turbine noise before than not. The population sample is highly educated, with most people having a university degree. Most participants are either students or employed for wages, with some being self-employed. This sample is deemed adequate for the current listening experiment as it does not attempt to gauge annoyance or attitudes. However, looking out for biases concerning these statistics in analysing the results is still essential.

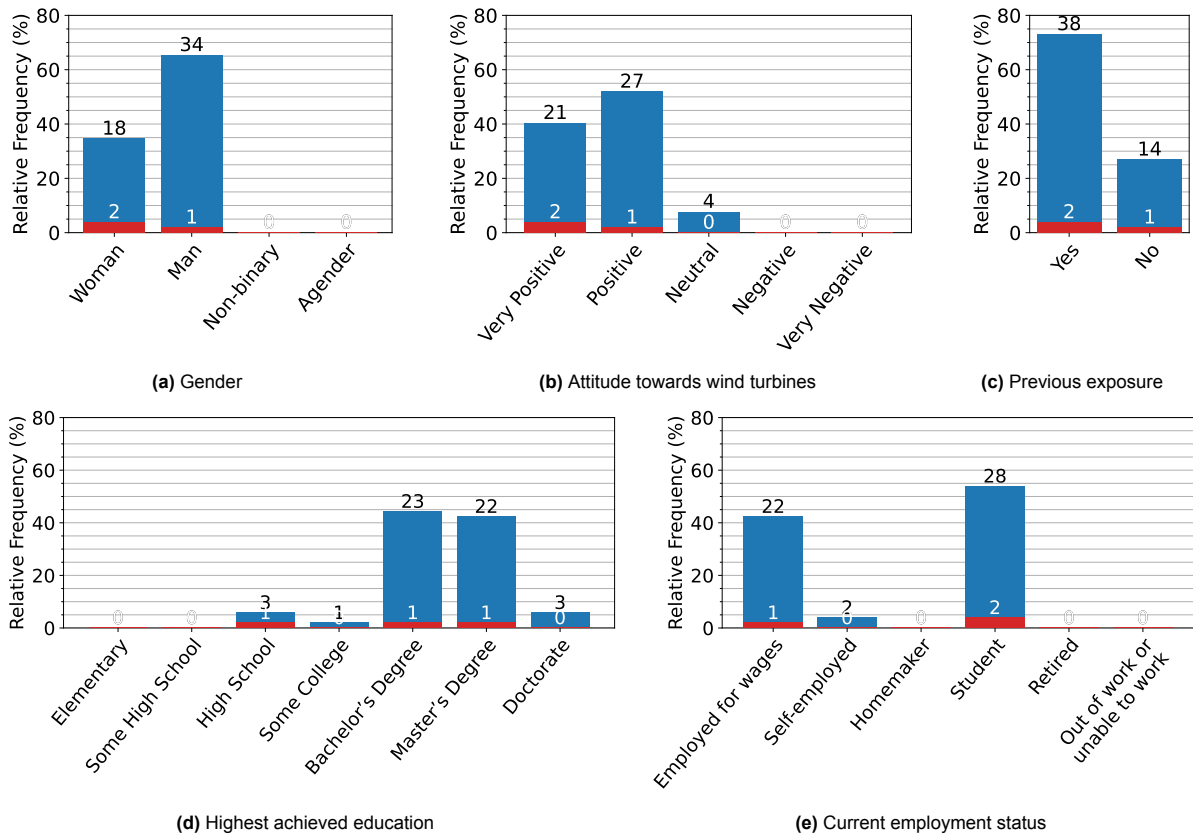


Figure 9.5: Statistics of the population sample participating in the listening experiment. The red parts of the bars represent the filtered outliers, as described in subsection 9.3.1.

Next to the above statistics, the participant age and the time taken to complete the experiment are also quickly highlighted with Figure 9.6 and Figure 9.7. The participants are relatively young, with a median of 25.5, a 3rd quartile of 28, and a maximum of 54 years. While this does raise a suspicion of age bias, there does not seem to be one in the results.

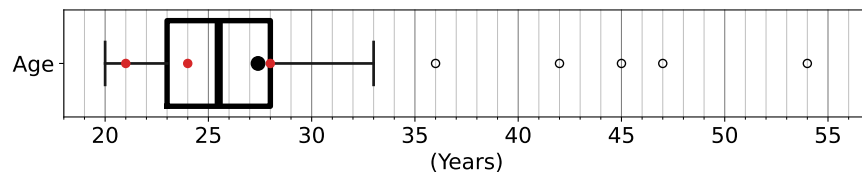


Figure 9.6: Age statistics of the listening experiment participants. Red dots represent the outliers filtered in subsection 9.3.1.

The completion time for the listening experiment was estimated at around 20 minutes, based on the amount and duration of the audio samples and on a rough estimate of the needed time to enter the answers and navigate through the interface. The completion time in Figure 9.7 shows that 20 minutes is a decent estimate, with most people completing the experiment within 15 to 18 minutes.

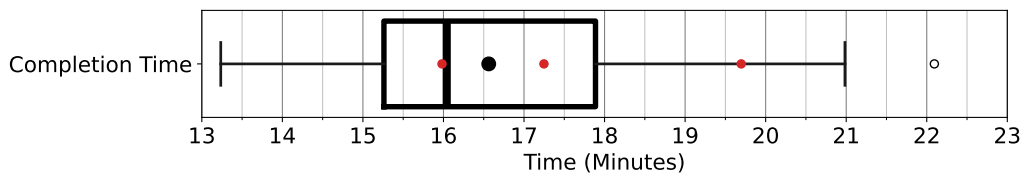


Figure 9.7: Completion time statistics of the listening experiment participants. Red dots represent the outliers filtered in subsection 9.3.1.

9.3. Experiment Results

This section discusses the findings of the listening experiment results. The filtering of outliers is covered first, followed by discussions of the three parts of the listening experiment as they relate to validating *WinTAur*.

9.3.1. Outlier Filtering with Pearson Correlation

As mentioned above, the Pearson correlation matrix filters the participant data for outliers. The matrices are shown before and after filtering in Figure 9.8. The results that are filtered are highly uncorrelated with the other results.

The number of outliers is red in the population statistic plots in Figure 9.5. It is found that the three outliers are distributed evenly through the population, and no bias is expected concerning the grouping of the participants.

There are ethical concerns regarding the filtering of data from human experiments. With participants actively participating in the experiment, it could be argued that outlier filtering wastes their time. While the author recognises this ethical concern, the added value of filtered data combined with the fact that participants are compensated regardless of their results is considered not to pose a moral issue. The data anonymisation is also done so that no explicit discrimination by the author is possible in selecting outliers and the threshold for outlier detection.

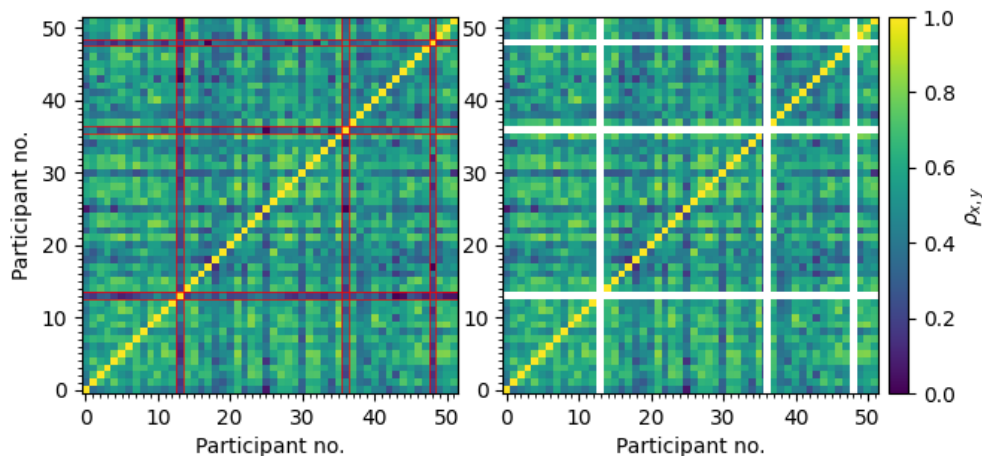
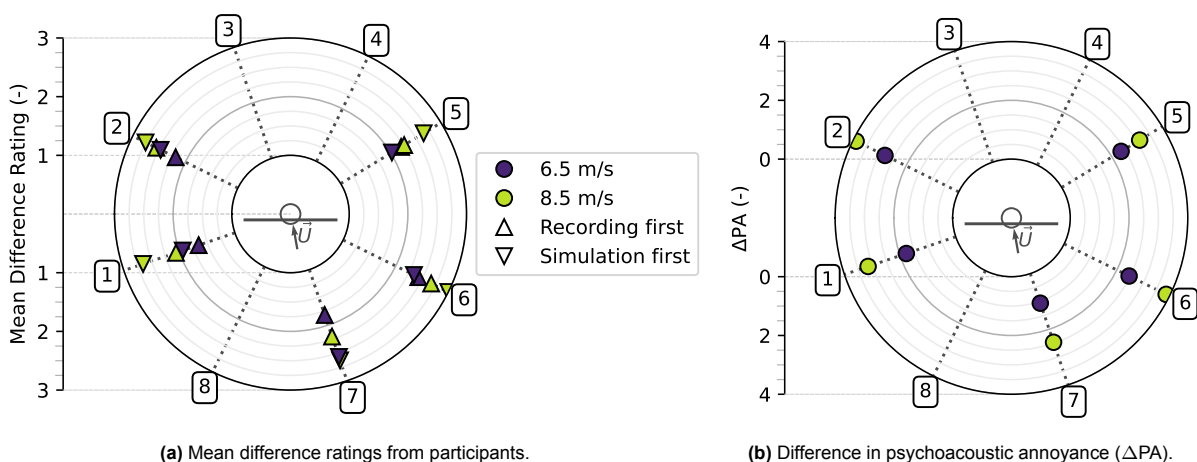


Figure 9.8: Pearson correlation matrices before (left) and after (right) outlier filtering, highlighting the participants marked as outliers. Note the diagonal is equal to one for all participants, as individual results are fully correlated with themselves.



(a) Mean difference ratings from participants.

(b) Difference in psychoacoustic annoyance (ΔPA).

Figure 9.9: Results for the presented differences in the first part of the listening experiment.

9.3.2. Differences Between Recordings and Simulations

Figure 9.9 shows the results of the first part of the listening experiment next to a sound quality metric analysis of the used samples. The relation with wind speed returns, with the psychoacoustic annoyance showing a more significant difference at higher wind speed. The mean subjective difference rating in Figure 9.9a confirms this relation. The directional differences from section 8.2 also return in the subjective ratings, proving the sound quality metrics can accurately validate the subjective human perception of the noise.

One parameter that raises questions is the order in which samples are presented. The difference rating is generally higher when a simulation sample is presented first than when a recording sample is presented first. The results in Figure 9.9a reflect this significant change. It is also found to be persistent in the presented cases. No explanation for this phenomenon is easily found but should be looked into further, as it may hurt the results and conclusions.

Regarding biases related to the population statistics, only one is significant enough to note, namely whether a participant indicated previous exposure to wind turbine noise. When not previously exposed, participants generally rate the differences between samples lower than when they have been. One suspected reason for this bias is that people with previous experience with wind turbine noise may recognise differences more easily and clearly.

9.3.3. Differences From Propagation Effects

Looking at the second part of the listening experiment, the differences are more minor than in the first part. This is expected based on the verbal impressions of the participants. The plot in Figure 9.10 shows the statistics of the difference ratings per step in propagation effect. These correspond to the names and steps presented in Table 9.4. On the left side of the plot, in orange, are the steps from no effects to only atmospheric absorption and from there to both propagation effects. The mean and standard deviation of adding these are shown in the third column. The central column shows the direct step from no propagation effects active to both being present. On the right side of this are the steps from no effects to only ground reflections to both effects being present, with their added mean and standard deviation next to the middle column. The right-most column presents the statistics when both effects are active in both samples, meaning no change is present.

Discussing the results in Figure 9.10, one can see that most propagation effects have some effect on the objective perception of the wind turbine noise. The effect is generally minimal. A limitation of the selected case could be the short propagation range. Due to the short range, the atmospheric absorption can only have little effect. The small rated difference in this experiment section could be partially explained by the significantly larger differences in the first part. Thus, the five-point scale may be a limiting factor. Also of note is that participants consistently rate a difference for the case where both samples are equal. From verbal feedback, this may be because participants did not expect this kind of case to be presented.

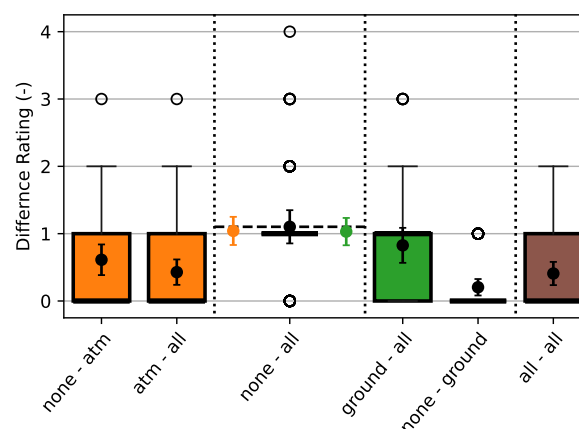


Figure 9.10: Statistics of the rated difference, per step in propagation effect addition as described Table 9.4.

Another curiosity is that adding the means and standard deviations of the partial steps from no effects to both results in a similar distribution to that of the direct step from none to both. It is also curious that adding a single effect can result in a lower or higher difference depending on the starting point. This can be explained intuitively, as having the additional sound from reflections is expected to suffer a more significant difference from adding atmospheric absorption.

9.3.4. Binaural Effect

The results for the third part of the experiment are shown in Figure 9.11. The results show many participants answered out of the expected range of answers on the front-rear axis. What is noted is that not many participants answered on the left-right axis for samples on the front-rear axis, showing the binaural rendering is decently capable of conveying a sense of direction. The experiment perfectly recognises the left-right difference, with no answers outside the expected range for samples on this axis. What is interesting to see is the more extensive spread of answers for samples on the left side compared to the right. A significant effect of the microphone location for the samples from the left side skews this result.

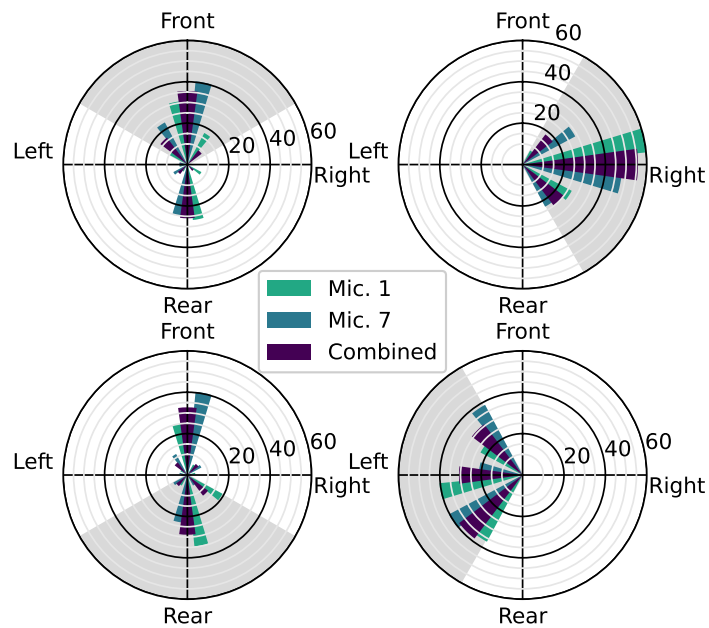


Figure 9.11: Relative frequency of indicated direction of the presented binaural wind turbine noise samples per origin location of the noise. The grey area marks the expected range of answers.

10

Conclusion and Future Work

This thesis set out to investigate the use of the aeroacoustics module of *HAWC2* in the auralisation of wind turbine noise. Implementing a complete toolchain from the frequency domain output of *HAWC2* to audio files has proven that this method is promising for psychoacoustic noise annoyance research.

In conclusion, a source, propagation, binaural rendering and signal reconstruction methodology have been proposed to cover all aspects of auralising the aeroacoustic output of *HAWC2*. These methodologies have been implemented in one code, called *WinTAur*. For signal reconstruction, a random phase method is chosen over the more complex phase reconstruction methods found in literature because initial results are not promising. Parts of this code are unit-tested and verified against their source literature, while other aspects are validated through numerical methods and a subjective listening experiment.

Differences in psychoacoustic loudness, sharpness and tonality between recorded and simulated noise have revealed discrepancies related to the wind speed. This relation is best explained by the limitations in stall noise modelling in *HAWC2*. In all metrics, differences in the level of discrepancy relate to the position around the wind turbine, where a position directly upstream shows the smallest discrepancies. The validation of *HAWC2* showing discrepancies in the directionality explains the latter finding. The fluctuation strength delta shows a dependence on the simulation case, which no single input parameter can easily explain. All differences between simulations and measurements are outside the ranges for just-noticeable-difference. The spectral analysis of these differences shows most of the discrepancies have three sources: the stall noise model, the noise directivity model and the ground reflection model. The first two significantly affect the results, while a change in ground type choice should fix the latter.

The numerical differences repeat in the results of a subjective listening experiment, where the same directional trends show up. The dependence on wind speed is also repeated in the subjective perception of the differences. This proves the psychoacoustic sound quality metrics should allow for accurate validation of future auralisation tools. The experiment also reflects the differences caused by adding propagation effects, such as atmospheric absorption and ground effects. These differences are more minor than the ones between simulations and measurements because of the short propagation distance.

Based on the results of this study, future work for the auralisation of modelled wind turbine noise is suggested. Firstly, a sensitivity analysis of the case-independent parameters is critical before improving the models. Conducting a validation with a large, pitch-controlled wind turbine should overcome the limitation of *HAWC2* regarding stall noise and is more relevant in the current onshore wind market. Noise measurements with lower background noise levels are strongly recommended as most of the available dataset was unusable due to a low signal-to-noise ratio.

Another recommendation is to explore different aeroacoustics models for use in the source modelling to potentially overcome the directivity limitations of *HAWC2*. The propagation model in this work is kept relatively simple as it only considers flat ground at 0 m altitude. Integrating the Gaussian beam tracing approach by Yunus [85] into the toolchain would enable the simulation of complex terrain and urban dwellings,

increasing the applicability of the code. This could allow for widespread use in public engagement regarding wind turbine projects near towns and villages. Proper modelling of turbulent scattering and the effect of the wind turbine wake can also prove valuable in a more accurate simulation of wind turbine noise.

While only investigated in a preliminary form, the binaural rendering in this work showed decent direction perception in the listening experiment. Creating a better resolution HRTF database and including this work in a VR system through real-time spatial rendering can enable an audio-visual investigation of wind turbine noise annoyance. Validating the binaural rendering through measurements with a head-and-torso simulator could provide valuable insights into wind turbine noise's directional effects.

A

Coordinate Systems

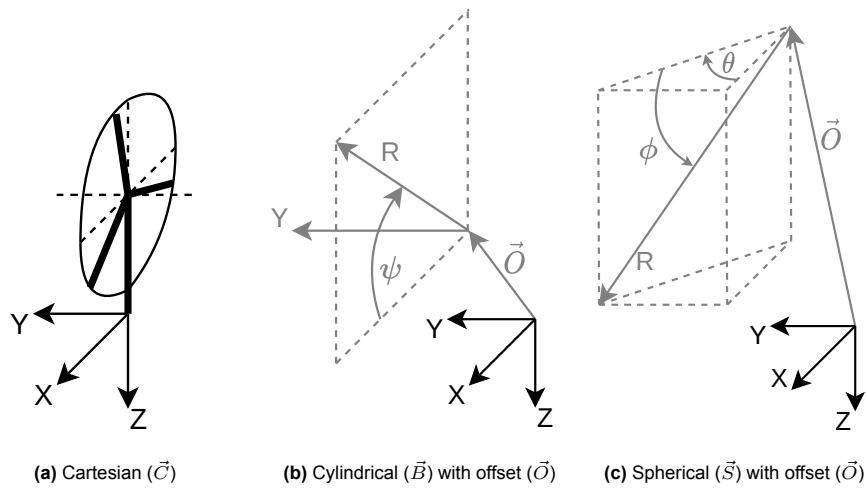


Figure A.1: Coordinate systems used in this thesis report

Cartesian

$$\vec{C}(x, y, z) \rightarrow \vec{S}(r, \theta, \phi) + \vec{O} : \begin{cases} r = \sqrt{(x - \vec{O}_x)^2 + (y - \vec{O}_y)^2 + (z - \vec{O}_z)^2} \\ \theta = \arctan\left(\frac{y - \vec{O}_y}{x - \vec{O}_x}\right) \\ \phi = \arctan\left(\frac{z - \vec{O}_z}{\sqrt{(x - \vec{O}_x)^2 + (y - \vec{O}_y)^2}}\right) \end{cases} \quad (\text{A.1})$$

$$\vec{C}(x, y, z) \rightarrow \vec{B}(r, y, \psi) + \vec{O} : \begin{cases} r = \sqrt{(x - \vec{O}_x)^2 + (y - \vec{O}_y)^2} \\ y = y - \vec{O}_y \\ \psi = \arctan\left(\frac{-(z - \vec{O}_z)}{x - \vec{O}_x}\right) \end{cases} \quad (\text{A.2})$$

$$\vec{C}(x, y, z) \rightarrow \vec{H}(r, \theta, \phi, \theta_0) + \vec{O} : \begin{cases} r = \sqrt{(x - \vec{O}_x)^2 + (y - \vec{O}_y)^2 + (z - \vec{O}_z)^2} \\ \theta = \arctan\left(\frac{\vec{O}_x - x}{y - \vec{O}_y}\right) - \theta_0 \\ \phi = \arctan\left(\frac{z - \vec{O}_z}{\sqrt{(x - \vec{O}_x)^2 + (y - \vec{O}_y)^2}}\right) \end{cases} \quad (\text{A.3})$$

Spherical

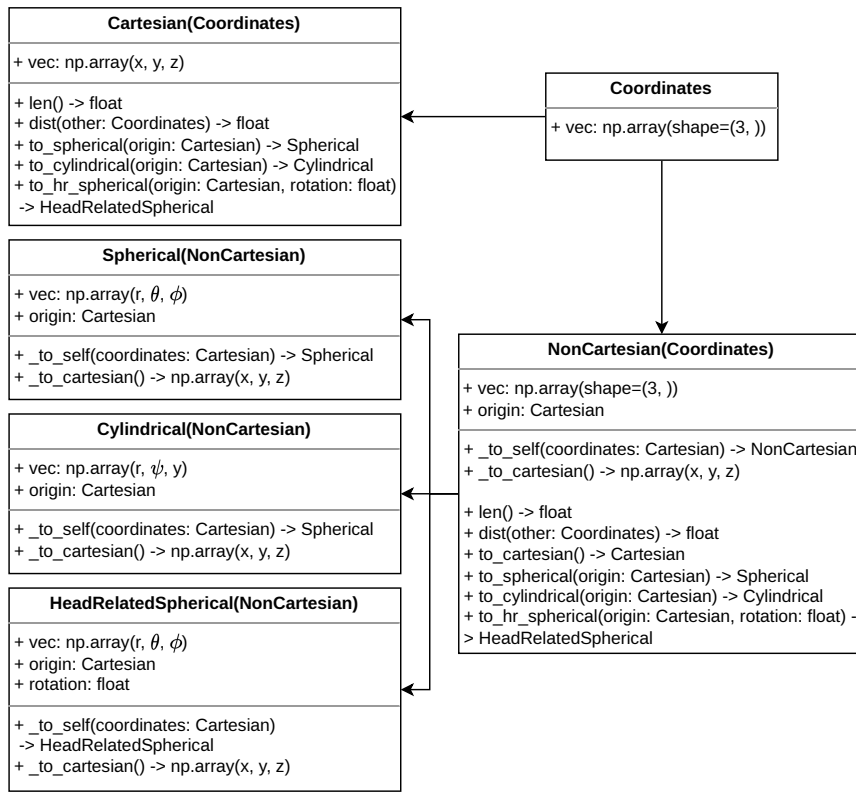
$$\vec{S}(r, \theta, \phi) + \vec{O} \rightarrow \vec{C}(x, y, z) : \begin{cases} x = r \cos \theta \cos \phi + \vec{O}_x \\ y = r \sin \theta \cos \phi + \vec{O}_y \\ z = r \sin \phi + \vec{O}_z \end{cases} \quad (\text{A.4})$$

Cylindrical

$$\vec{B}(r, y, \psi) + \vec{O} \rightarrow \vec{C}(x, y, z) : \begin{cases} x = r \cos \psi + \vec{O}_x \\ y = y + \vec{O}_y \\ z = -r \sin \psi + \vec{O}_z \end{cases} \quad (\text{A.5})$$

Head-Related Spherical

$$\vec{H}(r, \theta, \phi, \theta_0) + \vec{O} \rightarrow \vec{C}(x, y, z) : \begin{cases} x = -r \sin(\theta + \theta_0) \cos \phi + \vec{O}_x \\ y = r \cos(\theta + \theta_0) \cos \phi + \vec{O}_y \\ z = -r \sin \phi + \vec{O}_z \end{cases} \quad (\text{A.6})$$

**Figure A.2:** Class diagram of the Python implementation of the above coordinate systems.

B

Validation Data

Table B.1: Specification of the *Nordtank NTK 500/41* wind turbine (adapted from Paulsen, 2011 [198, Tab. 1]).

Rotor	
Rotor Diameter	41.1 m
Swept Area	1,320 m ²
Rotational Speed	27.1 RPM
Measured Tip Angle	$-0.2^\circ \pm 0.2^\circ$
Tilt	2°
Coning	0°
Blades	
Type	LM 19.1
Profiles	NACA 63-4xx and NACA FF-W3
Length	19.04 m
Chord	0.265 m - 1.630 m
Twist	0.02° - 20.00°
Air Brakes	Pivotal blade tips
Drivetrain	
Mechanical Brake	High speed shaft
Power Regulation	Passive aerodynamic stall
Gearbox	1:55.35 ratio Flender
Generator	Siemens 500 kW, 4 poles, 690 V
Tower	
Type	Conical steel tube
Hub Height	36 m
Masses	
Blade	1,960 kg
Rotor and Hub	9,030 kg
Tower Head Mass	24,430 kg
Tower Mass	22,500 kg

Table B.2: Summary of wind turbine data from October 15th, 2015 [199], [200].

Timestamp	Turbine Status	Mean WS (m/s)	Mean Rotor RPM	Mean Power (kW)	TI (%)	Temperature (°C)	Pressure (hPa)	Humidity (%)	Mean WD (°)	Mean yaw (°)
14:50	off	7.02	14.6	0	27	11.16	1022	64	67	293
14:52	off	8.24	14.6	0	18	11.16	1022	64	71	313
14:54	off	8.96	14.6	0	25	11.20	1022	64	71	84
14:56	change	8.87	14.7	0	17	11.16	1022	64	69	69
14:58	change	8.13	26.7	142	21	11.15	1022	64	66	79
15:00	on	8.19	26.9	177	21	11.13	1022	65	68	79
15:02	on	10.04	26.9	262	19	11.16	1022	65	67	79
15:04	on	8.55	26.9	142	16	11.13	1022	65	70	79
15:06	on	6.04	26.9	11	24	11.09	1022	65	75	79
15:08	on	5.69	26.9	104	32	11.05	1022	65	74	79
15:10	change	8.47	23.2	105	30	11.05	1022	65	71	79
15:12	off	9.95	14.6	0	16	11.12	1022	66	74	84
15:14	off	9.29	14.6	0	13	11.12	1022	66	71	85
15:16	off	8.64	14.6	0	24	11.06	1022	66	73	85
15:18	off	8.76	14.6	0	23	11.09	1022	66	74	85
15:20	off	7.84	14.6	0	16	11.07	1022	66	68	85
15:22	change	5.91	24.9	85	24	10.99	1022	66	69	85
15:24	on	6.26	26.9	111	22	10.93	1022	67	71	85
15:26	on	6.57	26.9	157	23	10.92	1022	67	74	85
15:28	on	8.29	26.9	215	21	10.96	1022	67	73	85
15:30	change	8.10	24.5	146	15	10.96	1022	67	72	85
15:32	off	6.97	14.6	0	21	10.95	1022	67	69	85

Table B.3: Summary of wind turbine data from October 23th, 2015 [199], [200].

Timestamp	Turbine Status	Mean WS (m/s)	Mean Rotor RPM	Mean Power (kW)	TI (%)	Temperature (°C)	Pressure (hPa)	Humidity (%)	Mean WD (°)	Mean yaw (°)
15:12	off	9.45	14.6	0	8	12.16	1017	74	285	252
15:14	off	9.27	14.6	0	6	12.17	1017	74	283	285
15:16	change	8.85	18.1	45	11	12.22	1017	74	286	298
15:18	on	7.91	26.9	164	8	12.18	1017	75	288	298
15:20	on	8.79	26.9	197	9	12.17	1017	75	287	298
15:22	on	8.44	26.9	201	5	12.22	1018	75	289	298
15:24	on	8.85	26.9	237	8	12.24	1018	75	289	298
15:26	change	9.01	26.0	197	6	12.27	1018	76	290	298
15:28	off	8.25	14.6	0	8	12.21	1018	76	288	298
15:30	off	8.87	14.6	0	8	12.20	1018	76	286	303
15:32	off	9.33	14.6	0	5	12.19	1017	76	288	305
15:34	off	8.97	14.6	0	5	12.17	1017	76	288	305
15:36	off	8.77	14.6	0	4	12.17	1017	77	289	305
15:38	change	7.30	22.9	76	9	12.10	1018	77	290	305
15:40	on	7.22	26.8	124	7	12.11	1018	77	288	297
15:42	on	6.58	26.8	94	4	12.15	1018	77	289	295
15:44	on	6.46	26.8	83	3	12.09	1018	78	291	295
15:46	change	6.65	25.5	72	7	12.04	1018	78	289	295
15:48	off	7.06	14.6	0	8	12.10	1018	78	287	295
15:50	off	8.11	14.6	0	7	12.13	1018	78	283	295
15:52	off	7.58	14.6	0	5	12.10	1018	79	282	295
15:54	off	7.26	14.6	0	9	12.07	1018	79	282	295
15:56	change	7.10	22.4	68	8	12.06	1018	79	281	295
15:58	on	7.70	26.9	151	7	12.07	1018	79	285	295
16:00	on	7.53	26.9	139	5	12.08	1018	80	286	295
16:02	on	7.58	26.9	148	6	12.09	1018	80	287	295
16:04	change	8.04	24.9	133.156	7	12.12	1018	80	291	295

Table B.4: Summary of wind turbine data from October 16th, 2015 [199], [200].

Timestamp	Turbine Status	Mean WS (m/s)	Mean Rotor RPM	Mean Power (kW)	Tl (%)	Temperature (°C)	Pressure (hPa)	Humidity (%)	Mean WD (°)	Mean yaw (°)
10:00	off	3.71	14.6	0	21	8.09	1019	97	29	292
10:02	off	3.37	14.6	0	20	8.09	1019	96	30	161
10:04	off	4.16	14.6	6	13	8.10	1019	96	28	42
10:06	off	4.02	14.6	0	22	8.11	1019	96	29	42
10:08	change	4.15	22.7	0	25	8.11	1019	96	25	42
10:10	change	4.49	26.0	-3	12	8.11	1019	96	28	42
10:12	change	4.03	26.5	7	22	8.13	1019	96	27	42
10:14	on	3.84	26.8	5	23	8.13	1019	96	27	41
10:16	on	4.05	26.8	8	20	8.13	1019	96	24	34
10:18	on	4.13	26.8	13	17	8.14	1019	96	27	34
10:20	change	3.93	26.0	18	19	8.15	1019	96	25	34
10:22	off	4.28	14.6	0	19	8.16	1019	96	29	35
10:24	off	4.11	14.6	0	21	8.17	1019	96	23	35
10:26	off	4.14	14.6	-6	16	8.18	1019	96	19	35
10:28	change	4.20	18.4	0	15	8.20	1019	96	25	35
10:30	change	3.68	26.8	24	17	8.21	1019	96	26	34
10:32	on	3.92	26.9	24	15	8.22	1019	95	30	35
10:34	on	4.51	26.8	-6	12	8.22	1019	95	28	34
10:36	change	4.42	26.6	3.	20	8.24	1019	95	30	34
10:38	change	4.01	26.5	11	16	8.25	1019	95	31	35
10:40	change	4.69	26.7	0	15	8.27	1019	95	29	38
10:42	on	4.43	26.9	1.	15	8.28	1019	95	26	38
10:44	on	3.90	26.9	7.	27	8.29	1019	95	27	38
10:46	on	3.80	26.9	3.	23	8.30	1019	95	24	39
10:48	on	3.01	26.9	20	27	8.32	1019	95	26	38
10:50	on	4.42	26.9	13	25	8.33	1019	95	24	39
10:52	on	3.79	26.9	15	21	8.32	1019	95	26	38
10:54	change	3.66	23.5	5	25	8.32	1019	95	29	38
10:56	off	3.93	14.6	0	23	8.35	1019	95	29	38
10:58	off	4.21	14.6	0	13	8.36	1019	95	27	38
11:00	off	3.67	14.6	0	14	8.39	1019	95	25	40
11:02	off	3.63	14.6	0	15	8.41	1019	94	24	77
11:04	off	4.30	14.6	-12	22	8.42	1019	94	28	82
11:06	off	4.19	14.6	-5	13	8.42	1019	94	25	61
11:08	off	3.51	14.6	-2	19	8.45	1019	94	27	54

C

Numerical Validation PBL Plots

— This page is intentionally left blank —
Plots start on the next page.

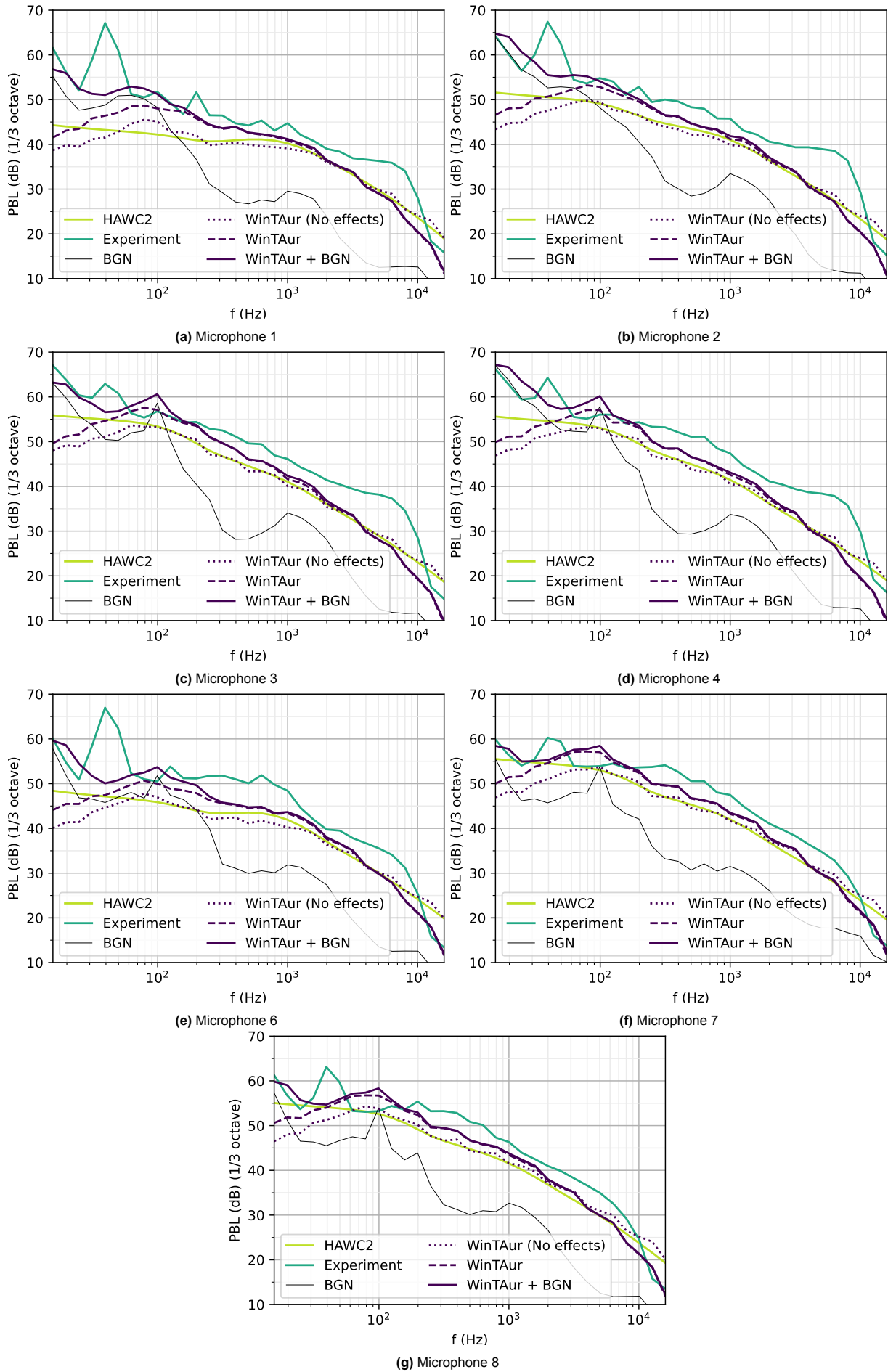


Figure C.1: 1/3 Octave band level spectra for the case: 23 Oct. 15:18 - 7.5 m/s

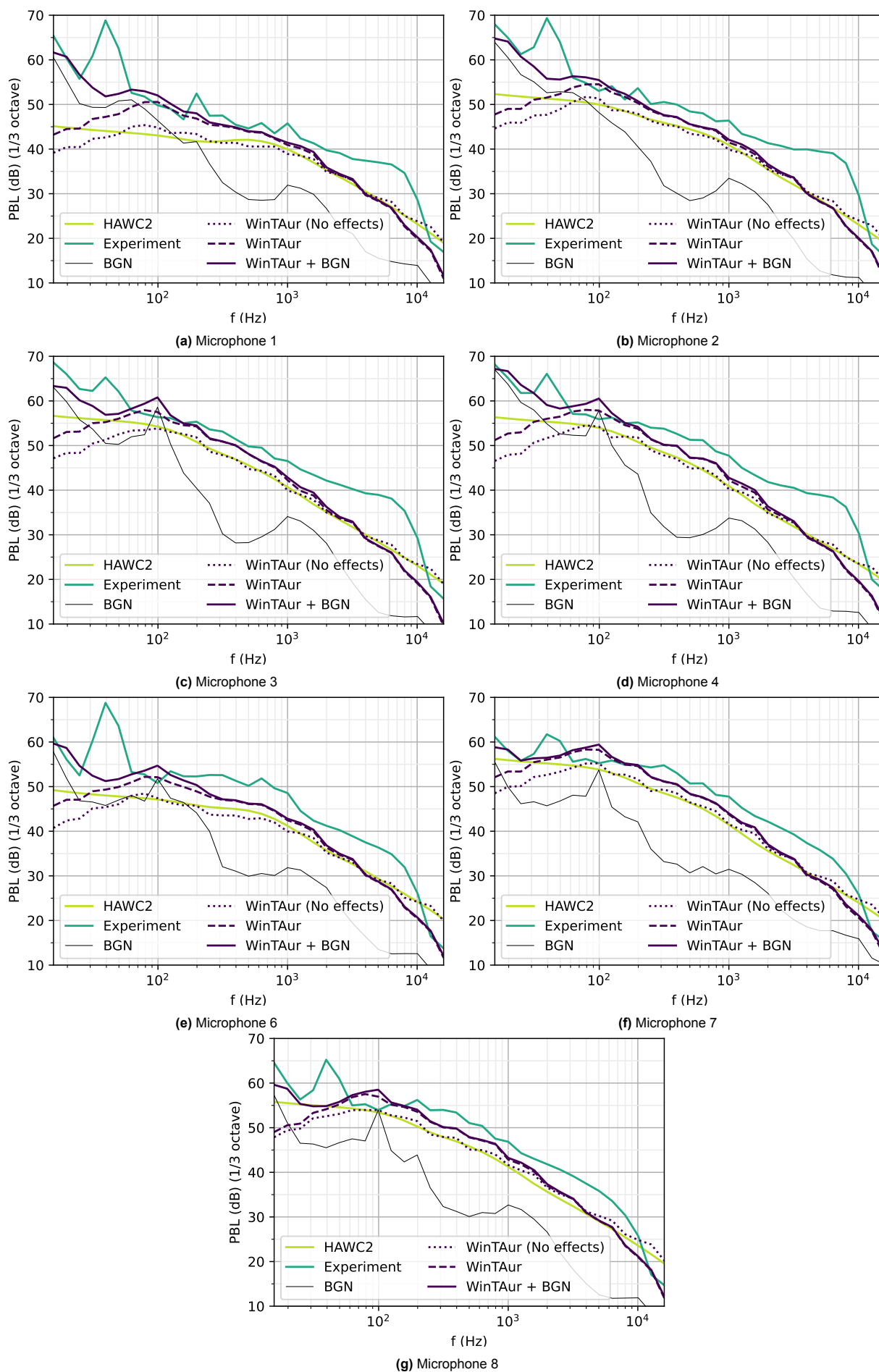


Figure C.2: 1/3 Octave band level spectra for the case: 23 Oct. 15:20 - 8.5 m/s

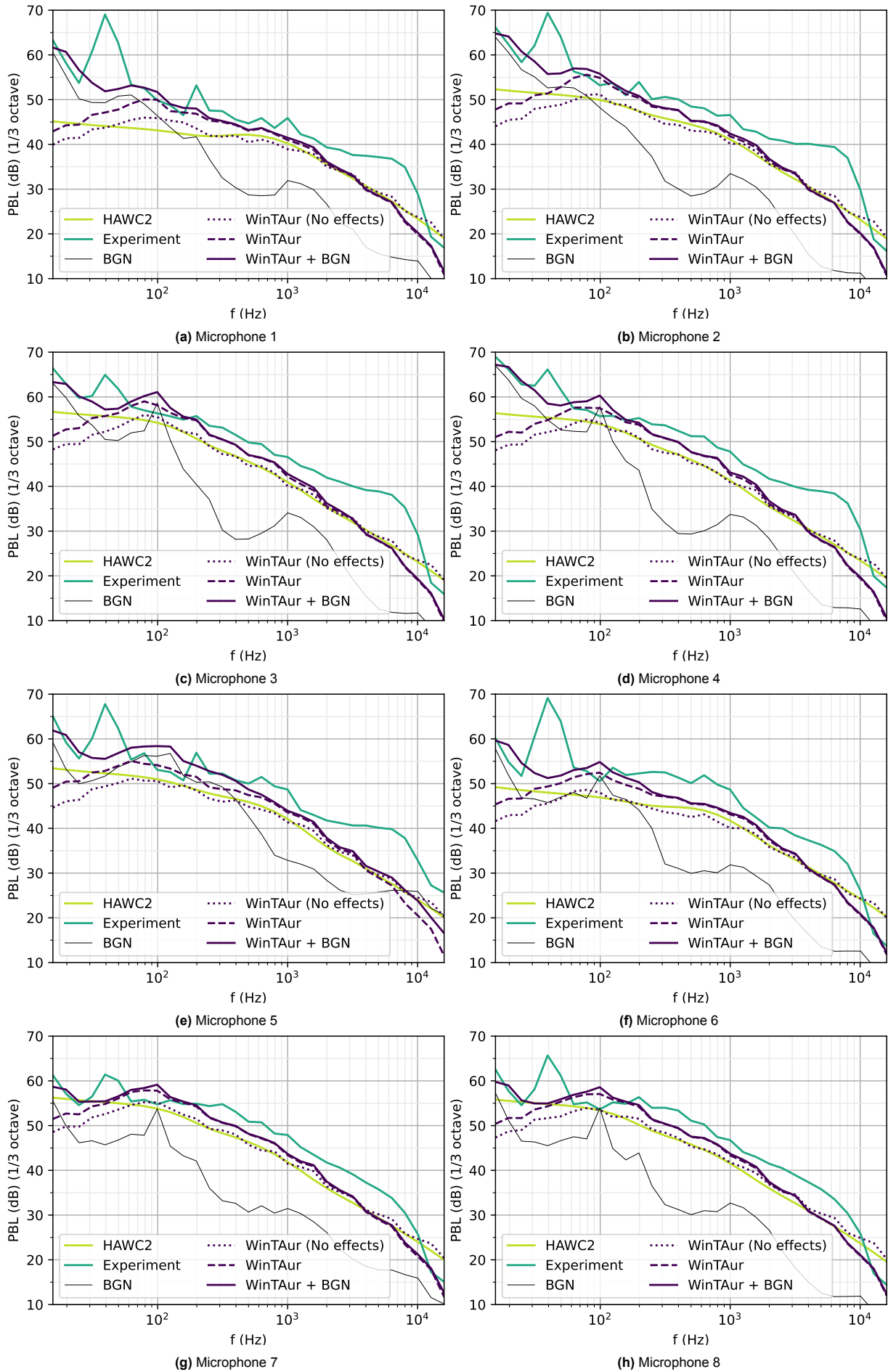


Figure C.3: 1/3 Octave band level spectra for the case: 23 Oct. 15:22 - 8.5 m/s

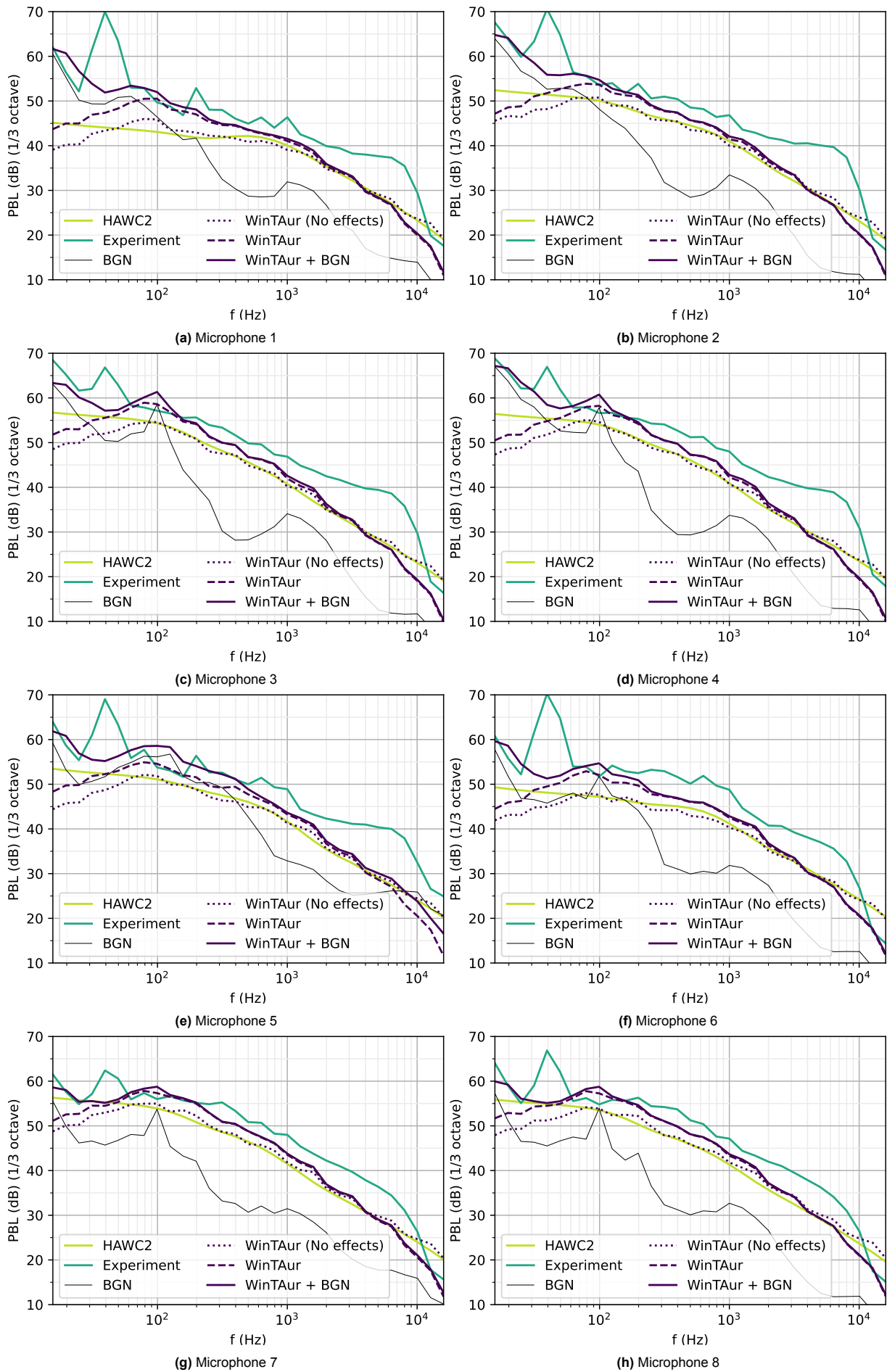


Figure C.4: 1/3 Octave band level spectra for the case: 23 Oct. 15:24 - 8.5 m/s

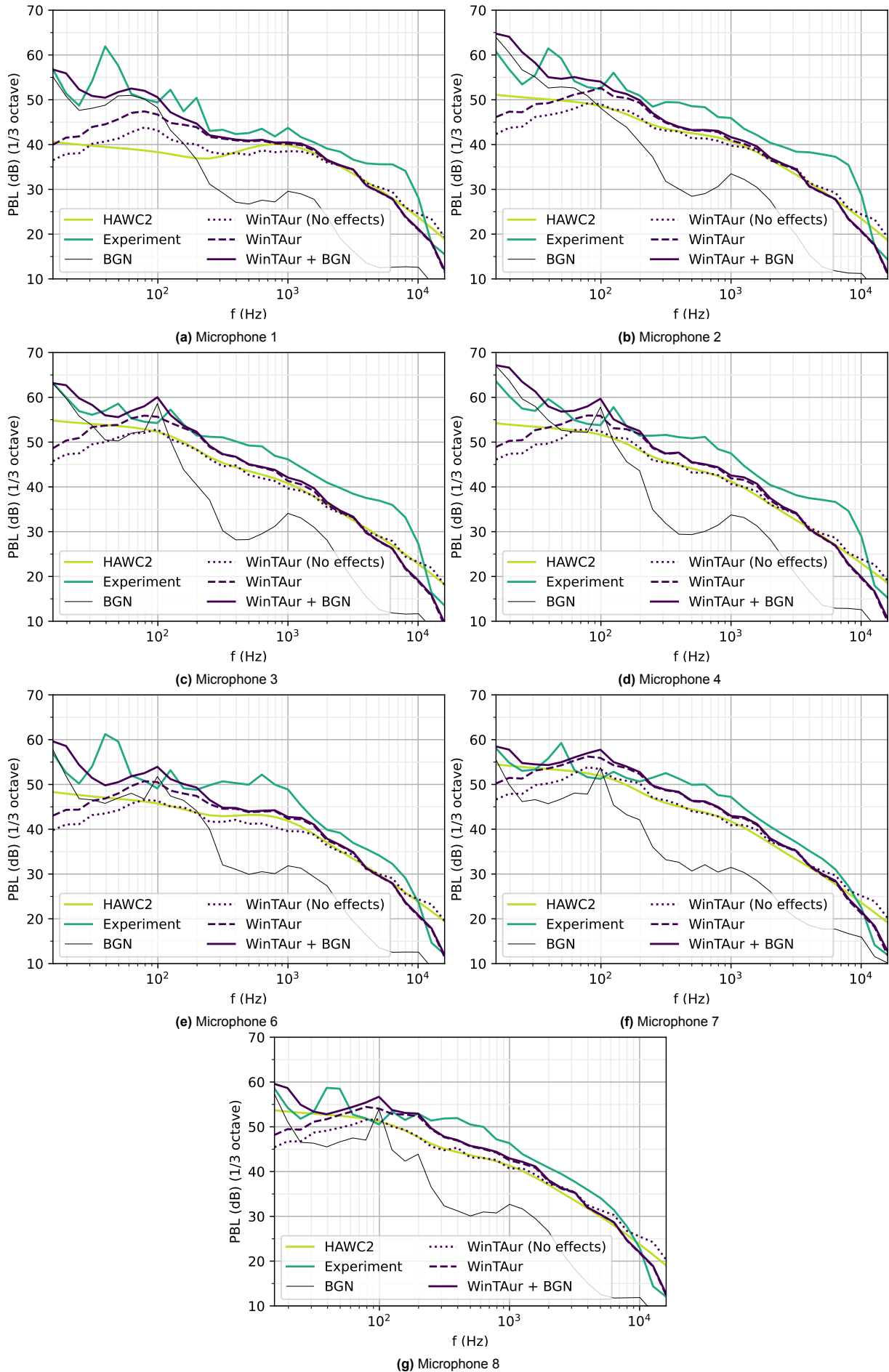


Figure C.5: 1/3 Octave band level spectra for the case: 23 Oct. 15:42 - 6.5 m/s

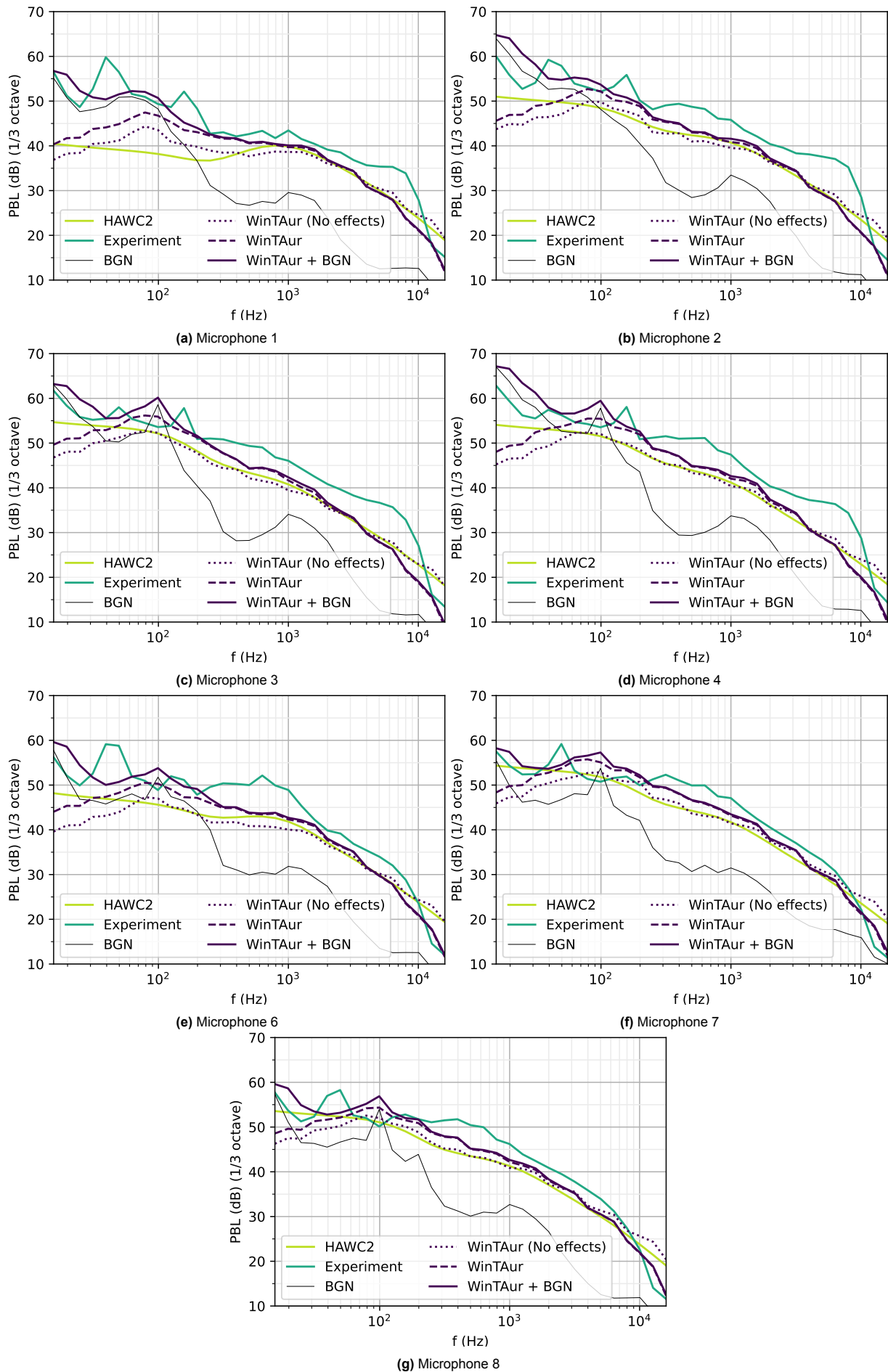


Figure C.6: 1/3 Octave band level spectra for the case: 23 Oct. 15:44 - 6.5 m/s

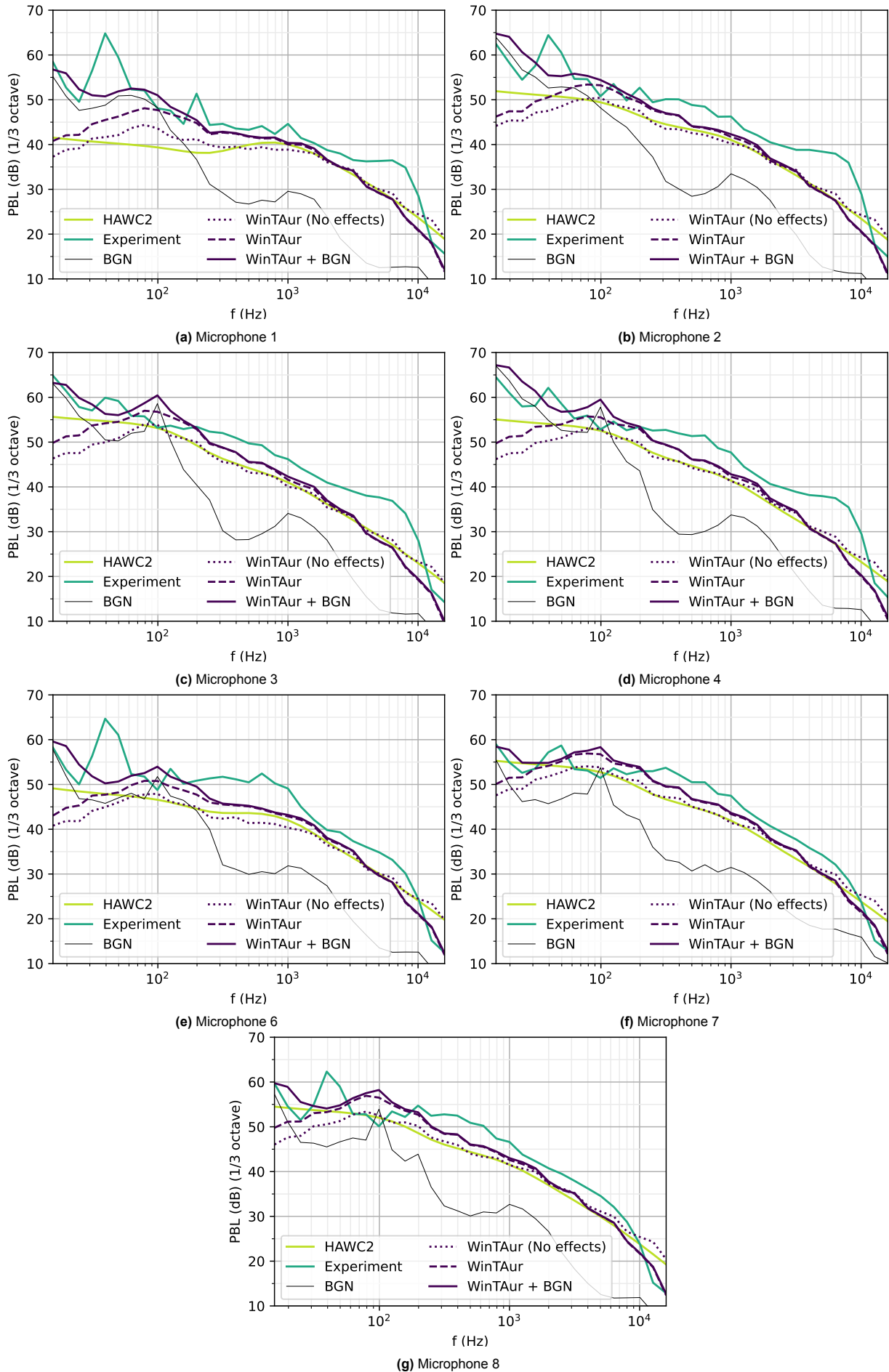


Figure C.7: 1/3 Octave band level spectra for the case: 23 Oct. 16:00 - 7.5 m/s

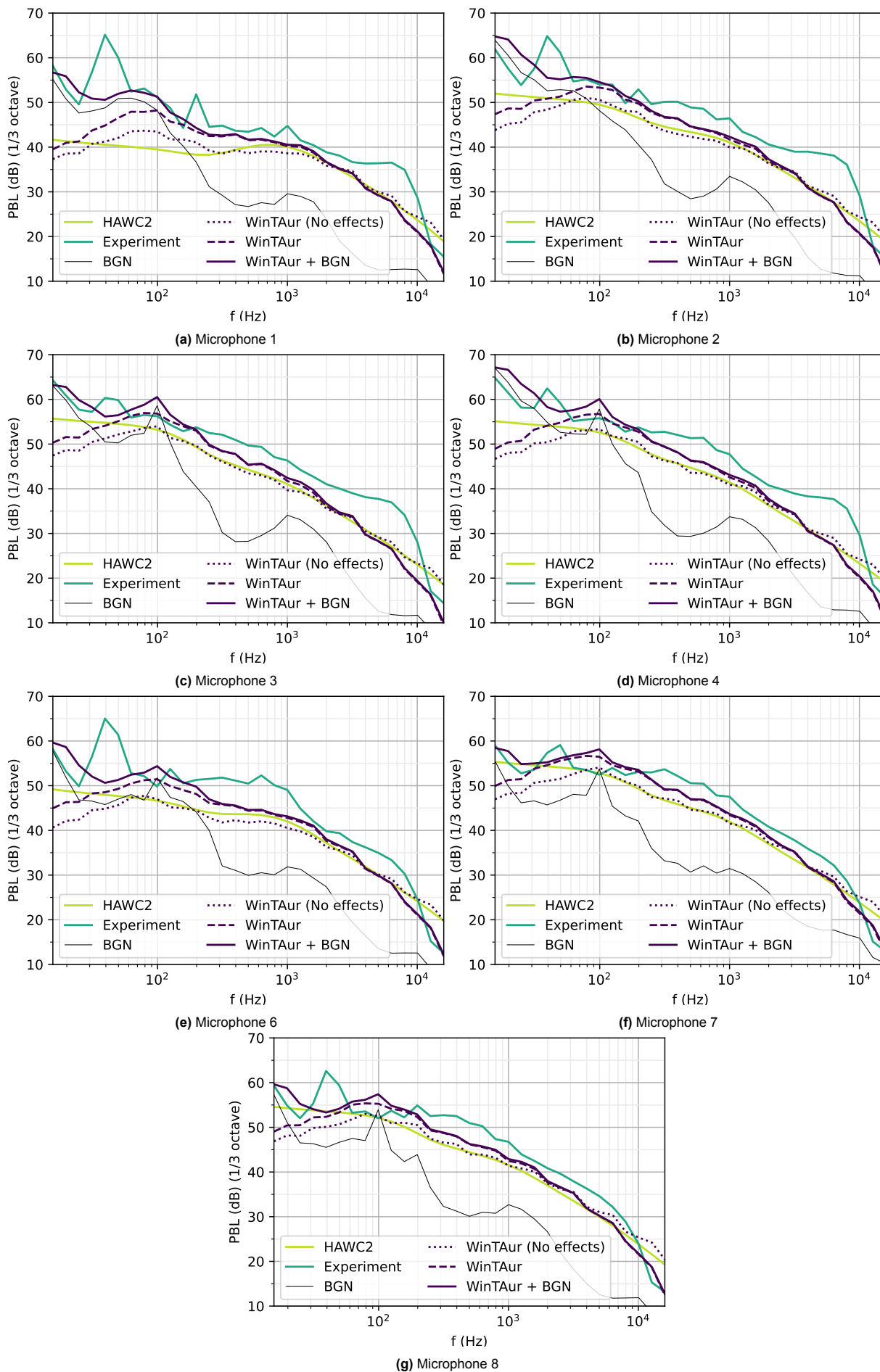


Figure C.8: 1/3 Octave band level spectra for the case: 23 Oct. 16:02 - 7.5 m/s

References

- [1] I. Komusanac, G. Brindley, D. Fraile, and L. Ramirez, “Wind energy in europe - 2021 statistics and the outlook for 2022-2026,” Wind Europe, Brussels, Belgium, Feb. 24, 2022.
- [2] G. Costanzo, G. Brindley, and P. Cole, “Wind energy in europe - 2022 statistics and the outlook for 2023-2027,” Wind Europe, Brussels, Belgium, Feb. 28, 2023.
- [3] R. Merino-Martínez, R. Pieren, and B. Schäffer, “Holistic approach to wind turbine noise: From blade trailing-edge modifications to annoyance estimation,” *Renewable and Sustainable Energy Reviews*, vol. 148, p. 111285, Sep. 2021. DOI: 10.1016/j.rser.2021.111285.
- [4] S. Oerlemans, M. Fisher, T. Maeder, and K. Kögler, “Reduction of wind turbine noise using optimized airfoils and trailing-edge serrations,” *AIAA Journal*, vol. 47, no. 6, pp. 1470–1481, Jun. 2009. DOI: 10.2514/1.38888.
- [5] D. S. Michaud, K. Feder, S. E. Keith, *et al.*, “Exposure to wind turbine noise: Perceptual responses and reported health effects,” *The Journal of the Acoustical Society of America*, vol. 139, no. 3, pp. 1443–1454, Mar. 2016. DOI: 10.1121/1.4942391.
- [6] V. Katinas, M. Marčiukaitis, and M. Tamašauskienė, “Analysis of the wind turbine noise emissions and impact on the environment,” *Renewable and Sustainable Energy Reviews*, vol. 58, pp. 825–831, May 2016. DOI: 10.1016/j.rser.2015.12.140.
- [7] R. Merino-Martinez, M. Snellen, and D. G. Simons, “Calculation of the fan rotational speed based on flyover recordings for improving aircraft noise prediction models,” in *Proceedings of the 23rd International Congress on Acoustics*, vol. 10 G - Aircraft noise, Aachen, Germany: Deutsche Gesellschaft für Akustik, Sep. 9, 2019, pp. 1600–1607.
- [8] R. Merino-Martínez, S. J. Heblj, D. H. T. Bergmans, M. Snellen, and D. G. Simons, “Improving aircraft noise predictions Considering Fan rotational speed,” *Journal of Aircraft*, vol. 56, no. 1, pp. 284–294, Jan. 2019. DOI: 10.2514/1.C034849.
- [9] H. M. E. Miedema and H. Vos, “Exposure-response relationships for transportation noise,” *The Journal of the Acoustical Society of America*, vol. 104, no. 6, pp. 3432–3445, Dec. 1998. DOI: 10.1121/1.423927.
- [10] E. Pedersen and K. Persson Waye, “Perception and annoyance due to wind turbine noise—a dose-response relationship,” *The Journal of the Acoustical Society of America*, vol. 116, no. 6, pp. 3460–3470, Dec. 2004. DOI: 10.1121/1.1815091.
- [11] B. Schäffer, S. J. Schlittmeier, R. Pieren, *et al.*, “Short-term annoyance reactions to stationary and time-varying wind turbine and road traffic noise: A laboratory study,” *The Journal of the Acoustical Society of America*, vol. 139, no. 5, pp. 2949–2963, May 2016. DOI: 10.1121/1.4949566.
- [12] S. A. Janssen, H. Vos, A. R. Eisses, and E. Pedersen, “A comparison between exposure-response relationships for wind turbine annoyance and annoyance due to other noise sources,” *The Journal of the Acoustical Society of America*, vol. 130, no. 6, pp. 3746–3753, Dec. 2011. DOI: 10.1121/1.3653984.
- [13] D. S. Michaud, S. E. Keith, K. Feder, *et al.*, “Personal and situational variables associated with wind turbine noise annoyance,” *The Journal of the Acoustical Society of America*, vol. 139, no. 3, pp. 1455–1466, Mar. 2016. DOI: 10.1121/1.4942390.
- [14] R. J. McCunney, K. A. Mundt, W. D. Colby, R. Dobie, K. Kaliski, and M. Blais, “Wind turbines and health: A critical review of the scientific literature,” *Journal of Occupational and Environmental Medicine*, vol. 56, no. 11, e108–e130, 2014, Publisher: Lippincott Williams & Wilkins.
- [15] J. H. Schmidt and M. Klokke, “Health effects related to wind turbine noise exposure: A systematic review,” *PLoS ONE*, vol. 9, no. 12, S. Tong, Ed., e114183, Dec. 4, 2014. DOI: 10.1371/journal.pone.0114183.

- [16] Z. A. Caddick, K. Gregory, L. Arsintescu, and E. E. Flynn-Evans, "A review of the environmental parameters necessary for an optimal sleep environment," *Building and Environment*, vol. 132, pp. 11–20, Mar. 2018. DOI: 10.1016/j.buildenv.2018.01.020.
- [17] E. Karasmanaki, "Is it safe to live near wind turbines? reviewing the impacts of wind turbine noise," *Energy for Sustainable Development*, vol. 69, pp. 87–102, Aug. 2022. DOI: 10.1016/j.esd.2022.05.012.
- [18] A. Bolders, M. Reedijk, and I. van Kamp, "Annoyance and sleep disturbance responses in people living in the vicinity of wind turbines in the netherlands," in *INTER-NOISE and NOISE-CON Congress and Conference Proceedings*, vol. 265, Feb. 1, 2023, pp. 4117–4124. DOI: 10.3397/IN_2022_0588.
- [19] A. Cranmer, J. D. Ericson, A. Ebers Broughel, B. Bernard, E. Robicheaux, and M. Podolski, "Worth a thousand words: Presenting wind turbines in virtual reality reveals new opportunities for social acceptance and visualization research," *Energy Research & Social Science*, vol. 67, p. 101507, Sep. 2020. DOI: 10.1016/j.erss.2020.101507.
- [20] R. Merino-Martínez, R. Pieren, B. Schäffer, and D. G. Simons, "Psychoacoustic model for predicting wind turbine noise annoyance," in *Proceedings of the 24th International Congress on Acoustics*, vol. A11: Psychoacoustics, Gyeongju, Korea, Oct. 24, 2022.
- [21] D. Pleban, G. Szczepanski, A. Wludarczyk, A. Alikowski, and K. Lada, "Assessment of wind turbine noise in laboratory conditions," *INTER-NOISE and NOISE-CON Congress and Conference Proceedings*, vol. 265, no. 4, pp. 3771–3776, Feb. 1, 2023. DOI: 10.3397/IN_2022_0532.
- [22] F. J. Y. Müller, V. Leschinger, G. Hübner, and J. Pohl, "Understanding subjective and situational factors of wind turbine noise annoyance," *Energy Policy*, vol. 173, p. 113361, Feb. 2023. DOI: 10.1016/j.enpol.2022.113361.
- [23] F. Butera, K. Burgemeister, K. Fisher, and D. Mounter, "Using wind farm noise auralisations for effective community consultation," in *Proceedings of 43rd International Congress on Noise Control Engineering*, vol. 249, Melbourne, Australia: The Australian Acoustical Society, Nov. 16, 2014, pp. 2993–3000.
- [24] J. K. Kirkegaard, D. P. Rudolph, S. Nyborg, *et al.*, "Tackling grand challenges in wind energy through a socio-technical perspective," *Nature Energy*, vol. 8, no. 7, pp. 655–664, Jun. 19, 2023. DOI: 10.1038/s41560-023-01266-z.
- [25] H. Fastl and E. Zwicker, *Psychoacoustics: facts and models* (Springer series in information sciences 22), 3rd. ed. Berlin, Germany; New York, NY, USA: Springer, 2007, 462 pp.
- [26] K. Waye and E. Öhrström, "Psycho-acoustic characters of relevance for annoyance of wind turbine noise," *Journal of Sound and Vibration*, vol. 250, no. 1, pp. 65–73, Feb. 2002. DOI: 10.1006/jsvi.2001.3905.
- [27] D. Mascarenhas, B. Cotté, and O. Doaré, "Synthesis of wind turbine trailing edge noise in free field," *JASA Express Letters*, vol. 2, no. 3, p. 033601, Mar. 2022, Publisher: Acoustical Society of America. DOI: 10.1121/10.0009658.
- [28] A. Bresciani, J. Maillard, and L. d. Santana, "Perceptual evaluation of wind turbine noise," presented at the 16ème Congrès Français d'Acoustique, CFA2022, Marseille, France: Société Française d'Acoustique; Laboratoire de Mécanique et d'Acoustique, Apr. 11, 2022.
- [29] W. C. van der Velden and D. Casalino, "Towards digital noise certification of serrated wind turbines," in *25th AIAA/CEAS Aeroacoustics Conference*, Delft, Netherlands: American Institute of Aeronautics and Astronautics, May 20, 2019. DOI: 10.2514/6.2019-2646.
- [30] K. Boorsma and J. G. Schepers, "Enhanced wind turbine noise prediction tool SILANT," presented at the Fourth International Meeting on Wind Turbine Noise, Rome, Italy: Energy research centre of the Netherlands (ECN), Apr. 12, 2011.
- [31] F. Bertagnolio, H. A. Madsen, and A. Fischer, "A combined aeroelastic-aeroacoustic model for wind turbine noise: Verification and analysis of field measurements," *Wind Energy*, vol. 20, no. 8, pp. 1331–1348, Aug. 2017. DOI: 10.1002/we.2096.
- [32] P. Bortolotti, E. Branlard, A. Platt, P. Moriarty, C. Sucameli, and C. Bottasso, "Aeroacoustics noise model of OpenFAST," National Renewable Energy Laboratory (NREL), Golden, CO, USA, Technical Report NREL/TP-5000-75731, Aug. 1, 2020. DOI: 10.2172/1660130.

- [33] M. Vorländer, *Auralization: Fundamentals of Acoustics, Modelling, Simulation, Algorithms and Acoustic Virtual Reality* (RWTHedition), Second. Cham, Switzerland: Springer International Publishing, 2020. DOI: 10.1007/978-3-030-51202-6.
- [34] S. A. L. Glegg and W. Devenport, *Aeroacoustics of low Mach number flows: fundamentals, analysis, and measurement*. London: Academic Press, 2017, 537 pp., OCLC: ocn959872129.
- [35] F. Bertagnolio and A. Fischer, "Wind turbine aerodynamic noise sources," in *Handbook of Wind Energy Aerodynamics*, B. Stoevesandt, G. Schepers, P. Fuglsang, and Y. Sun, Eds., Cham, Switzerland: Springer International Publishing, 2022, pp. 1365–1396. DOI: 10.1007/978-3-030-31307-4_70.
- [36] F. Brooks, D. S. Pope, and A. Marcolini, "Airfoil self-noise and prediction," NASA Langley Research Center, Hampton, VA, USA, NASA Reference Publication 1218, Jul. 1989.
- [37] S. Wagner, R. Bareiß, and G. Guidati, *Wind Turbine Noise*. Berlin, Heidelberg: Springer, 1996. DOI: 10.1007/978-3-642-88710-9.
- [38] R. K. Amiet, "Acoustic radiation from an airfoil in a turbulent stream," *Journal of Sound and Vibration*, vol. 41, no. 4, pp. 407–420, Aug. 22, 1975. DOI: 10.1016/S0022-460X(75)80105-2.
- [39] T. V. Kármán and C. C. Lin, "On the statistical theory of isotropic turbulence," in *Advances in Applied Mechanics*, R. V. Mises and T. V. Kármán, Eds., vol. 2, Elsevier, Jan. 1, 1951, pp. 1–19. DOI: 10.1016/S0065-2156(08)70297-7.
- [40] J. Mann, "The spatial structure of neutral atmospheric surface-layer turbulence," *Journal of Fluid Mechanics*, vol. 273, pp. 141–168, Aug. 1994, Publisher: Cambridge University Press. DOI: 10.1017/S0022112094001886.
- [41] W. J. Devenport, J. K. Staubs, and S. A. L. Glegg, "Sound radiation from real airfoils in turbulence," *Journal of Sound and Vibration*, vol. 329, no. 17, pp. 3470–3483, Aug. 16, 2010. DOI: 10.1016/j.jsv.2010.02.022.
- [42] P. Moriarty, G. Guidati, and P. Migliore, "Recent improvement of a semi-empirical aeroacoustic prediction code for wind turbines," in *10th AIAA/CEAS Aeroacoustics Conference*, Manchester, GREAT BRITAIN: American Institute of Aeronautics and Astronautics, May 10, 2004. DOI: 10.2514/6.2004-3041.
- [43] P. Moriarty, G. Guidati, and P. Migliore, "Prediction of turbulent inflow and trailing-edge noise for wind turbines," in *11th AIAA/CEAS Aeroacoustics Conference*, Monterey, CA, USA: American Institute of Aeronautics and Astronautics, May 23, 2005. DOI: 10.2514/6.2005-2881.
- [44] D. M. Chase, "Sound radiated by turbulent flow off a rigid half-plane as obtained from a wavevector spectrum of hydrodynamic pressure," *The Journal of the Acoustical Society of America*, vol. 52, no. 3, pp. 1011–1023, Sep. 1972. DOI: 10.1121/1.1913170.
- [45] K. L. Chandiramani, "Diffraction of evanescent waves, with applications to aerodynamically scattered sound and radiation from un baffled plates," *The Journal of the Acoustical Society of America*, vol. 55, no. 1, pp. 19–29, Jan. 1974. DOI: 10.1121/1.1919471.
- [46] M. Howe, "A review of the theory of trailing edge noise," *Journal of Sound and Vibration*, vol. 61, no. 3, pp. 437–465, Dec. 1978. DOI: 10.1016/0022-460X(78)90391-7.
- [47] R. K. Amiet, "Noise due to turbulent flow past a trailing edge," *Journal of Sound and Vibration*, vol. 47, no. 3, pp. 387–393, Aug. 8, 1976. DOI: 10.1016/0022-460X(76)90948-2.
- [48] M. Roger and S. Moreau, "Back-scattering correction and further extensions of amiet's trailing-edge noise model. part 1: Theory," *Journal of Sound and Vibration*, vol. 286, no. 3, pp. 477–506, Sep. 6, 2005. DOI: 10.1016/j.jsv.2004.10.054.
- [49] S. Moreau and M. Roger, "Back-scattering correction and further extensions of amiet's trailing-edge noise model. part II: Application," *Journal of Sound and Vibration*, vol. 323, no. 1, pp. 397–425, Jun. 5, 2009. DOI: 10.1016/j.jsv.2008.11.051.
- [50] R. Parchen, "Progress report DRAW: A prediction scheme for trailing-edge noise based on detailed boundary-layer characteristics," TNO Institute of Applied Physics, The Netherlands, TNO Report HAG-RPT-980023, 1998.

- [51] R. H. Kraichnan, "Pressure fluctuations in turbulent flow over a flat plate," *The Journal of the Acoustical Society of America*, vol. 28, no. 3, pp. 378–390, May 1956. DOI: 10.1121/1.1908336.
- [52] M. Drela, "XFOIL: An analysis and design system for low Reynolds number airfoils," in *Low Reynolds Number Aerodynamics*, T. J. Mueller, Ed., ser. Lecture Notes in Engineering, Berlin, Heidelberg: Springer, 1989, pp. 1–12. DOI: 10.1007/978-3-642-84010-4_1.
- [53] M. Kamruzzaman, T. Lutz, A. Herrig, and E. Krämer, "Semi-empirical modeling of turbulent anisotropy for airfoil self-noise predictions," *AIAA Journal*, vol. 50, no. 1, pp. 46–60, Jan. 2012. DOI: 10.2514/1.J050805.
- [54] A. Fischer, F. Bertagnolio, and H. A. Madsen, "Improvement of TNO type trailing edge noise models," *European Journal of Mechanics - B/Fluids, Rotating Flows*, vol. 61, pp. 255–262, Jan. 1, 2017. DOI: 10.1016/j.euromechflu.2016.09.005.
- [55] M. Goody, "Empirical spectral model of surface pressure fluctuations," *AIAA Journal*, vol. 42, no. 9, pp. 1788–1794, Sep. 2004. DOI: 10.2514/1.9433.
- [56] Y. Rozenberg, G. Robert, and S. Moreau, "Wall-pressure spectral model including the adverse pressure gradient effects," *AIAA Journal*, vol. 50, no. 10, pp. 2168–2179, Oct. 2012, Publisher: American Institute of Aeronautics and Astronautics. DOI: 10.2514/1.J051500.
- [57] S. Lee, "Empirical wall-pressure spectral modeling for zero and adverse pressure gradient flows," *AIAA Journal*, vol. 56, no. 5, pp. 1818–1829, May 2018, Publisher: American Institute of Aeronautics and Astronautics. DOI: 10.2514/1.J056528.
- [58] R. D. Sandberg and N. D. Sandham, "Direct numerical simulation of turbulent flow past a trailing edge and the associated noise generation," *Journal of Fluid Mechanics*, vol. 596, pp. 353–385, Jan. 2008, Publisher: Cambridge University Press. DOI: 10.1017/S0022112007009561.
- [59] R. Sandberg and L. Jones, "Reprint of: Direct numerical simulations of airfoil self-noise," *Procedia IUTAM*, vol. 1, pp. 274–282, 2010. DOI: 10.1016/j.piutam.2010.10.029.
- [60] R. Sandberg and L. Jones, "Direct numerical simulations of low Reynolds number flow over airfoils with trailing-edge serrations," *Journal of Sound and Vibration*, vol. 330, no. 16, pp. 3818–3831, Aug. 2011. DOI: 10.1016/j.jsv.2011.02.005.
- [61] M. Wang and P. Moin, "Computation of trailing-edge flow and noise using large-eddy simulation," *AIAA Journal*, vol. 38, no. 12, pp. 2201–2209, Dec. 2000. DOI: 10.2514/2.895.
- [62] W. R. Wolf and S. K. Lele, "Trailing-edge noise predictions using compressible large-eddy simulation and acoustic analogy," *AIAA Journal*, vol. 50, no. 11, pp. 2423–2434, Nov. 2012. DOI: 10.2514/1.J051638.
- [63] M. S. Howe, "Noise produced by a sawtooth trailing edge," *The Journal of the Acoustical Society of America*, vol. 90, no. 1, pp. 482–487, Jul. 1, 1991. DOI: 10.1121/1.401273.
- [64] B. Lyu, M. Azarpeyvand, and S. Sinayoko, "Prediction of noise from serrated trailing edges," *Journal of Fluid Mechanics*, vol. 793, pp. 556–588, Apr. 25, 2016. DOI: 10.1017/jfm.2016.132.
- [65] A. Rubio Carpio, R. Merino Martínez, F. Avallone, D. Ragni, M. Snellen, and S. van der Zwaag, "Experimental characterization of the turbulent boundary layer over a porous trailing edge for noise abatement," *Journal of Sound and Vibration*, vol. 443, pp. 537–558, Mar. 17, 2019. DOI: 10.1016/j.jsv.2018.12.010.
- [66] C. Teruna, F. Avallone, D. Ragni, A. Rubio-Carpio, and D. Casalino, "Numerical analysis of a 3-d printed porous trailing edge for broadband noise reduction," *Journal of Fluid Mechanics*, vol. 926, A17, Nov. 2021, Publisher: Cambridge University Press. DOI: 10.1017/jfm.2021.704.
- [67] B. Søndergaard, "Noise and low frequency noise from wind turbines," in *Proceedings of 43rd International Congress on Noise Control Engineering*, vol. 249, Melbourne, Australia: The Australian Acoustical Society, Nov. 16, 2014, pp. 6201–6212.
- [68] F. Bertagnolio, H. A. Madsen, A. Fischer, and C. Bak, "A semi-empirical airfoil stall noise model based on surface pressure measurements," *Journal of Sound and Vibration*, vol. 387, pp. 127–162, Jan. 2017. DOI: 10.1016/j.jsv.2016.09.033.

- [69] J. Christophe, J. Anthoine, and S. Moreau, "Trailing edge noise of a controlled-diffusion airfoil at moderate and high angle of attack," in *15th AIAA/CEAS Aeroacoustics Conference (30th AIAA Aeroacoustics Conference)*, Miami, Florida: American Institute of Aeronautics and Astronautics, May 11, 2009. DOI: 10.2514/6.2009-3196.
- [70] S. Nagarajan, S. Hahn, and S. Lele, "Prediction of sound generated by a pitching airfoil: A comparison of RANS and LES," in *12th AIAA/CEAS Aeroacoustics Conference (27th AIAA Aeroacoustics Conference)*, Cambridge, Massachusetts: American Institute of Aeronautics and Astronautics, May 8, 2006. DOI: 10.2514/6.2006-2516.
- [71] J. G. Kocheemoolayil, W. R. Wolf, and S. K. Lele, "Large eddy simulation of stall noise," in *20th AIAA/CEAS Aeroacoustics Conference*, Atlanta, GA: American Institute of Aeronautics and Astronautics, Jun. 16, 2014. DOI: 10.2514/6.2014-3182.
- [72] S. Moreau, M. Roger, and J. Christophe, "Flow features and self-noise of airfoils near stall or in stall," in *15th AIAA/CEAS Aeroacoustics Conference (30th AIAA Aeroacoustics Conference)*, Miami, Florida: American Institute of Aeronautics and Astronautics, May 11, 2009. DOI: 10.2514/6.2009-3198.
- [73] C. Y. Schuele and K.-S. S. Rossignol, "Trailing-edge noise modeling and validation for separated flow conditions," in *19th AIAA/CEAS Aeroacoustics Conference*, Berlin, Germany: American Institute of Aeronautics and Astronautics, May 27, 2013. DOI: 10.2514/6.2013-2008.
- [74] A. Suryadi and M. Herr, "Wall pressure spectra on a DU96-w-180 profile from low to pre-stall angles of attack," in *21st AIAA/CEAS Aeroacoustics Conference*, Dallas, TX: American Institute of Aeronautics and Astronautics, Jun. 22, 2015. DOI: 10.2514/6.2015-2688.
- [75] C. Arakawa, O. Fleig, M. Iida, and M. Shimooka, "Numerical approach for noise reduction of wind turbine blade tip with earth simulator," *Journal of the Earth Simulator*, vol. 2, no. 3, 2005.
- [76] M. Schneider, "Investigation of axial fan tip noise mechanisms by means of CAA and beamforming technique," in *INTER-NOISE and NOISE-CON Congress and Conference Proceedings*, vol. 253, Aug. 21, 2016, pp. 3866–3877.
- [77] A. George, F. Najjar, and Y. Kim, "Noise due to tip vortex formation on lifting rotors," in *6th Aeroacoustics Conference*, Hartford, CT, U.S.A.: American Institute of Aeronautics and Astronautics, Jun. 4, 1980. DOI: 10.2514/6.1980-1010.
- [78] D. J. Moreau, C. J. Doolan, W. N. Alexander, T. W. Meyers, and W. J. Devenport, "Wall-mounted finite airfoil-noise production and prediction," *AIAA Journal*, vol. 54, no. 5, pp. 1637–1651, May 2016. DOI: 10.2514/1.J054493.
- [79] M. Miller, "The multi-objective design of flatback wind turbine airfoils," Master Thesis, Carleton University, Ottawa, ON, Canada, Dec. 17, 2016. DOI: 10.13140/RG.2.2.20396.67201.
- [80] F. Yunus, D. Casalino, F. Avallone, and D. Ragni, "Efficient prediction of airborne noise propagation in a non-turbulent urban environment using gaussian beam tracing method," *The Journal of the Acoustical Society of America*, vol. 153, no. 4, p. 2362, Apr. 19, 2023. DOI: 10.1121/10.0017825.
- [81] T. F. W. Embleton, J. E. Piercy, and G. A. Daigle, "Effective flow resistivity of ground surfaces determined by acoustical measurements," *The Journal of the Acoustical Society of America*, vol. 74, no. 4, pp. 1239–1244, Oct. 1983. DOI: 10.1121/1.390029.
- [82] H. E. Bass, L. C. Sutherland, and A. J. Zuckerwar, "Atmospheric absorption of sound: Update," *The Journal of the Acoustical Society of America*, vol. 88, no. 4, pp. 2019–2021, Oct. 1990. DOI: 10.1121/1.400176.
- [83] H. E. Bass, L. C. Sutherland, A. J. Zuckerwar, D. T. Blackstock, and D. M. Hester, "Atmospheric absorption of sound: Further developments," *The Journal of the Acoustical Society of America*, vol. 97, no. 1, pp. 680–683, Jan. 1995. DOI: 10.1121/1.412989.
- [84] International Organisation for Standardisation (ISO), "Acoustics - attenuation of sound during propagation outdoors - part 1: Calculation of the absorption of sound by the atmosphere," International Standard ISO 9613-1, Aug. 1993.
- [85] F. Yunus, "Methodologies and algorithms for sound propagation in complex environments with application to urban air mobility: A ray acoustics approach," Doctoral thesis, Delft University of Technology, Delft, Netherlands, 2023. DOI: 10.4233/UUID:72D10B7A-6790-41FC-9B15-26F9CCCD77F.

- [86] M. Arntzen, "Aircraft noise calculation and synthesis in a non-standard atmosphere," Doctoral thesis, Delft University of Technology, Delft, Netherlands, Dec. 4, 2014.
- [87] R. Stull, *Practical Meteorology: An Algebra-based Survey of Atmospheric Science*. 1.02b. Vancouver, BC, Canada: University of British Columbia, 2017.
- [88] K. Attenborough, "Sound propagation in the atmosphere," in *Springer Handbook of Acoustics*, T. D. Rossing, Ed., 2nd ed., New York, NY, USA: Springer New York, Jan. 15, 2015, pp. 117–155.
- [89] A. V. Oppenheim, R. W. Schaffer, and J. R. Buck, *Discrete-time signal processing*, 2nd ed. Upper Saddle River, N.J.: Prentice Hall, 1999, 870 pp.
- [90] P. Welch, "The use of fast fourier transform for the estimation of power spectra: A method based on time averaging over short, modified periodograms," *IEEE Transactions on Audio and Electroacoustics*, vol. 15, no. 2, pp. 70–73, Jun. 1967. DOI: 10.1109/TAU.1967.1161901.
- [91] P. Virtanen, R. Gommers, T. E. Oliphant, *et al.*, "SciPy 1.0: Fundamental algorithms for scientific computing in python," *Nature Methods*, vol. 17, no. 3, pp. 261–272, Mar. 2, 2020. DOI: 10.1038/s41592-019-0686-2.
- [92] D. Griffin and J. Lim, "Signal estimation from modified short-time fourier transform," *IEEE Transactions on Acoustics, Speech, and Signal Processing*, vol. 32, no. 2, pp. 236–243, Apr. 1984. DOI: 10.1109/TASSP.1984.1164317.
- [93] R. Pieren, K. Heutschi, M. Müller, M. Manyoky, and K. Eggenschwiler, "Auralization of wind turbine noise: Emission synthesis," *Acta Acustica united with Acustica*, vol. 100, no. 1, pp. 25–33, Jan. 1, 2014. DOI: 10.3813/AAA.918683.
- [94] R. Pieren, "Auralization of environmental acoustical sceneries," Doctoral thesis, Delft University of Technology, Delft, Netherlands, 2018. DOI: 10.4233/UUID:8DBFB507-A0B0-4CCD-9772-88E213C69206.
- [95] P. Finne, E. Thysell, and C. W. Claumarch, "Auralisations for outdoor noise sources - environmental auralisations," in *Proceedings of the 23rd International Congress on Acoustics*, vol. 11 E - Environmental sound auralisation, Aachen, Germany: Deutsche Gesellschaft für Akustik, Sep. 9, 2019, pp. 1691–1696.
- [96] D. Mascarenhas, B. Cotté, and O. Doaré, "Physics-based auralization of wind turbine noise," presented at the 9th International Conference on Wind Turbine Noise, Remote from Europe, May 18, 2021.
- [97] M. Roger and S. Moreau, "Extensions and limitations of analytical airfoil broadband noise models," *International Journal of Aeroacoustics*, vol. 9, no. 3, pp. 273–305, May 2010. DOI: 10.1260/1475-472X.9.3.273.
- [98] G. M. Corcos, "The structure of the turbulent pressure field in boundary-layer flows," *Journal of Fluid Mechanics*, vol. 18, no. 3, pp. 353–378, Mar. 1964, Publisher: Cambridge University Press. DOI: 10.1017/S002211206400026X.
- [99] Siemens Digital Industries Software, *Simcenter STAR-CCM+*, version 2022.1, Siemens, 2022.
- [100] E. Salomons, D. van Maercke, J. Defrance, and F. de Roo, "The harmonoise sound propagation model," *Acta Acustica united with Acustica*, vol. 97, no. 1, pp. 62–74, Jan. 1, 2011. DOI: 10.3813/AAA.918387.
- [101] T. J. Larsen and A. M. Hansen, "How 2 HAWC2, the user's manual," DTU, Department of Wind Energy, Roskilde, Denmark, Technical Report Risø-R-1597(ver. 12.9)(EN), Oct. 2021.
- [102] W. C. van der Velden and D. Casalino, "Towards digital wind turbine noise certification," in *Proceedings of the 8th International Conference on Wind Turbine Noise*, Lisbon, Portugal, Jun. 12, 2019, pp. 12–14.
- [103] Dassault Systèmes, *SIMULIA PowerFLOW 2022*, 2022.
- [104] S. A. L. Glegg and W. Devenport, "The fflowcs williams and hawkings equation," in *Aeroacoustics of low Mach number flows: fundamentals, analysis, and measurement*, London: Academic Press, 2017, pp. 95–114.

- [105] R. Paterson and R. Amiet, "Acoustic radiation and surface pressure characteristics of an airfoil due to incident turbulence," in *3rd Aeroacoustics Conference*, Palo Alto, CA, U.S.A.: American Institute of Aeronautics and Astronautics, Jul. 20, 1976. DOI: 10.2514/6.1976-571.
- [106] J. Gershfeld, "Leading edge noise from thick foils in turbulent flows," *The Journal of the Acoustical Society of America*, vol. 116, no. 3, pp. 1416–1426, Sep. 2004. DOI: 10.1121/1.1780575.
- [107] F. Bertagnolio, A. Fischer, and W. Jun Zhu, "Tuning of turbulent boundary layer anisotropy for improved surface pressure and trailing-edge noise modeling," *Journal of Sound and Vibration*, vol. 333, no. 3, pp. 991–1010, Feb. 2014. DOI: 10.1016/j.jsv.2013.10.008.
- [108] J. A. Michelsen, "Basis3d - a platform for development of multiblock PDE solvers: Beta - release," Technical University of Denmark, Kgs. Lyngby, Denmark, Technical Report AFM 92-05, 1992.
- [109] J. A. Michelsen, "Block structured multigrid solution of 2d and 3d elliptic PDE's," Technical University of Denmark, Kgs. Lyngby, Denmark, Technical Report AFM 94-06, 1994.
- [110] N. N. Sørensen, "General purpose flow solver applied to flow over hills," Risø National Laboratory, Roskilde, Denmark, Thesis/Dissertation Risø-R-827(EN), 1995, ISBN: 87-550-2079-8.
- [111] F. Bertagnolio, "Boundary layer measurements of the NACA0015 and implications for noise modeling," DTU, Risø National Laboratory for Sustainable Energy, Wind Energy Division, Roskilde, Denmark, Technical Report Risø-R-1761(EN), Feb. 14, 2011.
- [112] M. Deserno, "How to generate equidistributed points on the surface of a sphere," Max-Planck-Institut für Polymerforschung, Mainz, Germany, Sep. 28, 2004.
- [113] S. Oerlemans and B. Méndez López, "Acoustic array measurements on a full scale wind turbine," in *11th AIAA/CEAS Aeroacoustics Conference*, Monterey, California: American Institute of Aeronautics and Astronautics, May 23, 2005. DOI: 10.2514/6.2005-2963.
- [114] S. Oerlemans, P. Sijtsma, and B. Méndez López, "Location and quantification of noise sources on a wind turbine," *Journal of Sound and Vibration*, vol. 299, no. 4, pp. 869–883, Feb. 2007. DOI: 10.1016/j.jsv.2006.07.032.
- [115] E. M. Salomons, *Computational Atmospheric Acoustics*. Dordrecht, Netherlands: Springer Netherlands : Imprint : Springer, 2001, OCLC: 840307642.
- [116] M. B. Porter and H. P. Bucker, "Gaussian beam tracing for computing ocean acoustic fields," *The Journal of the Acoustical Society of America*, vol. 82, no. 4, pp. 1349–1359, Oct. 1987. DOI: 10.1121/1.395269.
- [117] Y. Gabillet, H. Schroeder, G. A. Daigle, and A. L'Espérance, "Application of the gaussian beam approach to sound propagation in the atmosphere: Theory and experiments," *The Journal of the Acoustical Society of America*, vol. 93, no. 6, pp. 3105–3116, Jun. 1993. DOI: 10.1121/1.405722.
- [118] L. Euler, *Institutionum calculi integralis. Vol 1*. ed. alt. Petropoli: Academiae Imperialis Scientiarum, 1792.
- [119] R. Klees and R. Dwight, "Applied numerical analysis," Delft University of Technology, Delft, Netherlands, Course notes AE2220-I, Feb. 2020.
- [120] J. D. Anderson, *Fundamentals of aerodynamics* (McGraw-Hill series in aeronautical and aerospace engineering), Sixth edition. New York, NY: McGraw Hill Education, 2017, 1130 pp.
- [121] International Organisation for Standardisation (ISO), "Standard atmosphere," International Standard ISO 2533-1975, May 15, 1975.
- [122] C. R. Harris, K. J. Millman, S. J. Van Der Walt, *et al.*, "Array programming with NumPy," *Nature*, vol. 585, no. 7825, pp. 357–362, Sep. 17, 2020. DOI: 10.1038/s41586-020-2649-2.
- [123] U. Ingard, "On the reflection of a spherical sound wave from an infinite plane," *The Journal of the Acoustical Society of America*, vol. 23, no. 3, pp. 329–335, May 1951. DOI: 10.1121/1.1906767.
- [124] C. I. Chessell, "Propagation of noise along a finite impedance boundary," *The Journal of the Acoustical Society of America*, vol. 62, no. 4, pp. 825–834, Oct. 1977. DOI: 10.1121/1.381603.
- [125] H. H. Hubbard, "Aeroacoustics of flight vehicles: Theory and practice - volume 2: Noise control," NASA Langley Research Center, Hampton, VA, USA, NASA Reference Publication 1258 Vol. 2, Aug. 1991.

- [126] G. v. Rossum and F. L. Drake, *The Python language reference* (Python documentation manual / Guido van Rossum; Fred L. Drake [ed.] Pt. 2), Release 3.0.1 [Repr.] Hampton, NH, USA: Python Software Foundation, 2010, 109 pp.
- [127] M. Delany and E. Bazley, "Acoustical properties of fibrous absorbent materials," *Applied Acoustics*, vol. 3, no. 2, pp. 105–116, Apr. 1970. DOI: 10.1016/0003-682X(70)90031-9.
- [128] L. C. Sutherland and G. A. Daigle, "Atmospheric sound propagation," in *Encyclopedia of Acoustics. Volume 1*. Hoboken, NY, USA: Wiley-Interscience [Imprint] John Wiley & Sons, Incorporated, Feb. 2007, pp. 341–366, OCLC: 938479264.
- [129] J. Blauert, *Spatial Hearing: The Psychophysics of Human Sound Localization*, 2nd ed. The MIT Press, Oct. 11, 1996. DOI: 10.7551/mitpress/6391.001.0001.
- [130] S. von Hünenbein, A. King, B. Piper, and M. Cand, "Wind turbine amplitude modulation: Research to improve understanding as to its cause & effect - work package b(2): Development of an AM dose-response relationship," University of Salford Manchester - Acoustics Research Centre, 2013.
- [131] W. G. Gardner and K. D. Martin, *HRTF measurements of a KEMAR dummy-head microphone*, Database. [Online]. Available: <https://sound.media.mit.edu/resources/KEMAR.html>, May 18, 1994.
- [132] W. G. Gardner and K. D. Martin, "HRTF measurements of a KEMAR," *The Journal of the Acoustical Society of America*, vol. 97, no. 6, pp. 3907–3908, Jun. 1995. DOI: 10.1121/1.412407.
- [133] M. D. Burkhard and R. M. Sachs, "Anthropometric manikin for acoustic research," *The Journal of the Acoustical Society of America*, vol. 58, no. 1, pp. 214–222, Jul. 1975. DOI: 10.1121/1.380648.
- [134] E. Shaw, "External ear response and sound localization," in *Localization of sound: theory and applications*, W. Gatehouse, Ed., Groton: Amphora, 1982, p. 30.
- [135] A. Schmitz, *Open HRTF dataset - artificial head*, Database, Jan. 22, 2018.
- [136] R. Bomhardt, M. de la Fuente Klain, and J. Fels, *A high-resolution head-related transfer function and three-dimensional ear model database*, Proceedings of meetings on acoustics 29, 050002 (2016). Database, Nov. 28, 2019. DOI: 10.1121/2.0000467.
- [137] P. Majdak, M. Noisternig, H. Wierstorf, *et al.*, *Main SOFA repository*, Database, Dec. 2, 2022.
- [138] H. Møller, D. Hammershøi, C. B. Johnson, and M. F. Sørensen, "Evaluation of artificial heads in listening tests," *J. Audio Eng. Soc.*, vol. 47, no. 3, pp. 83–100, 1999.
- [139] D. Hammershøi and H. Møller, "Binaural technique — basic methods for recording, synthesis, and reproduction," in *Communication Acoustics*, J. Blauert, Ed., Berlin/Heidelberg: Springer-Verlag, 2005, pp. 223–254. DOI: 10.1007/3-540-27437-5_9.
- [140] P. Majdak, "Multiple exponential sweep method for fast measurement of head-related transfer functions," *J. Audio Eng. Soc.*, vol. 55, no. 7, 2007.
- [141] B. S. Masiero, M. Pollow, and J. Fels, "Design of a fast broadband individual head-related transfer function measurement system," presented at the Forum Acusticum 2011, Aalborg, Denmark: European Acoustics Association, Jul. 27, 2011.
- [142] B. S. Masiero, "Individualized binaural technology: Measurement, equalization and subjective evaluation," Doctoral thesis, RWTH Aachen, Aachen, Germany, 2013, 177 pp.
- [143] C. Moldrzyk, W. Ahnert, S. Feistel, T. Lentz, and S. Weinzierl, "Head-tracked auralization of acoustical simulation," presented at the Audio Engineering Society Convention 117, San Francisco, CA, USA: Audio Engineering Society, Oct. 28, 2004.
- [144] J. W. S. Lord Rayleigh, "XII. on our perception of sound direction," *The London, Edinburgh, and Dublin Philosophical Magazine and Journal of Science*, vol. 13, no. 74, pp. 214–232, Feb. 1907. DOI: 10.1080/14786440709463595.
- [145] R. S. Woodworth, *Experimental psychology* (Experimental psychology). Oxford, England: Holt, 1938, 889 pp.
- [146] W. E. Feddersen, T. T. Sandel, D. C. Teas, and L. A. Jeffress, "Localization of high-frequency tones," *The Journal of the Acoustical Society of America*, vol. 29, no. 9, pp. 988–991, Sep. 1957. DOI: 10.1121/1.1909356.

- [147] S. Carlile, "The physical and psychophysical basis of sound localization," in *Virtual Auditory Space: Generation and Applications*. Berlin, Heidelberg: Springer Berlin Heidelberg, 1996, pp. 27–78, Series Title: Neuroscience Intelligence Unit. DOI: 10.1007/978-3-662-22594-3_2.
- [148] J. W. H. Schnupp, J. Booth, and A. J. King, "Modeling individual differences in ferret external ear transfer functions," *The Journal of the Acoustical Society of America*, vol. 113, no. 4, pp. 2021–2030, Apr. 2003. DOI: 10.1121/1.1547460.
- [149] C. Brown and R. Duda, "A structural model for binaural sound synthesis," *IEEE Transactions on Speech and Audio Processing*, vol. 6, no. 5, pp. 476–488, Sep. 1998. DOI: 10.1109/89.709673.
- [150] J. Nam, J. S. Abel, and J. O. Smith III, "A method for estimating interaural time difference for binaural synthesis," presented at the Audio Engineering Society Convention 125, San Francisco, CA, USA: Audio Engineering Society, Oct. 2, 2008.
- [151] N. L. Aaronson and W. M. Hartmann, "Testing, correcting, and extending the woodworth model for interaural time difference," *The Journal of the Acoustical Society of America*, vol. 135, no. 2, pp. 817–823, Feb. 2014. DOI: 10.1121/1.4861243.
- [152] J. W. S. Lord Rayleigh, *The Theory Of Sound Vol.2*. New York, NY, USA: Dover Publications, 1896.
- [153] B. F. G. Katz and M. Noisternig, "A comparative study of interaural time delay estimation methods," *The Journal of the Acoustical Society of America*, vol. 135, no. 6, pp. 3530–3540, Jun. 2014. DOI: 10.1121/1.4875714.
- [154] L. A. Abbagnaro, B. B. Bauer, and E. L. Torick, "Measurements of diffraction and interaural delay of a progressive sound wave caused by the human head. II," *The Journal of the Acoustical Society of America*, vol. 58, no. 3, pp. 693–700, Sep. 1975, Publisher: Acoustical Society of America. DOI: 10.1121/1.380716.
- [155] G. F. Kuhn, "Model for the interaural time differences in the azimuthal plane," *The Journal of the Acoustical Society of America*, vol. 62, no. 1, pp. 157–167, Jul. 1977, Publisher: Acoustical Society of America. DOI: 10.1121/1.381498.
- [156] D. R. Begault and L. J. Trejo, "3-d sound for virtual reality and multimedia," NASA Ames Research Center, Moffett Field, CA, USA, NASA/TM-2000-209606, Aug. 1, 2000, NTRS Author Affiliations: NASA Ames Research Center, NTRS Document ID: 20010044352 NTRS Research Center: Ames Research Center (ARC).
- [157] R. Algazi, C. Avendano, and R. O. Duda, "Estimation of a spherical-head model from anthropometry," *J. Aud. Eng. Soc.*, vol. 49, 2001.
- [158] D. J. Kistler and F. L. Wightman, "A model of head-related transfer functions based on principal components analysis and minimum-phase reconstruction," *The Journal of the Acoustical Society of America*, vol. 91, no. 3, pp. 1637–1647, Mar. 1992, Publisher: Acoustical Society of America. DOI: 10.1121/1.402444.
- [159] J. C. Middlebrooks, "Individual differences in external-ear transfer functions reduced by scaling in frequency," *The Journal of the Acoustical Society of America*, vol. 106, no. 3, pp. 1480–1492, Sep. 1999, Publisher: Acoustical Society of America. DOI: 10.1121/1.427176.
- [160] E. A. Macpherson and J. C. Middlebrooks, "Listener weighting of cues for lateral angle: The duplex theory of sound localization revisited," *The Journal of the Acoustical Society of America*, vol. 111, no. 5, pp. 2219–2236, May 2002, Publisher: Acoustical Society of America. DOI: 10.1121/1.1471898.
- [161] E. H. A. Langendijk and A. W. Bronkhorst, "Contribution of spectral cues to human sound localization," *The Journal of the Acoustical Society of America*, vol. 112, no. 4, pp. 1583–1596, Oct. 2002, Publisher: Acoustical Society of America. DOI: 10.1121/1.1501901.
- [162] S. Kuwada, R. Batra, and D. C. Fitzpatrick, "Neural processing of binaural temporal cues," in *Binaural and spatial hearing in real and virtual environments*, R. H. Gilkey and T. R. Anderson, Eds., Mahwah, NJ, USA: Lawrence Erlbaum Associates, Inc., 1997, pp. 399–425.
- [163] J.-M. Jot, V. Larcher, and O. Warusfel, "Digital signal processing issues in the context of binaural and transaural stereophony," presented at the Audio Engineering Society Convention 98, Paris, France: Audio Engineering Society, Feb. 25, 1995.

- [164] P. Minnaar, J. Plogsties, S. K. Olesen, F. Christensen, and H. Møller, "The interaural time difference in binaural synthesis," presented at the Audio Engineering Society Convention 108, Paris, France: Audio Engineering Society, Feb. 19, 2000.
- [165] A. Pérez López, H. Helmholtz, and N. Ortega, *Pysofascoustics*, 2023.
- [166] R. V. L. Hartley and T. C. Fry, "The binaural location of pure tones.," *Physical Review*, vol. 18, no. 6, pp. 431–442, Dec. 1, 1921, Publisher: American Physical Society. DOI: 10.1103/PhysRev.18.431.
- [167] R. Abdelmalek, Z. Mnasri, and F. Benzarti, "Audio signal reconstruction using phase retrieval: Implementation and evaluation," *Multimedia Tools and Applications*, vol. 81, no. 11, pp. 15 919–15 946, May 2022. DOI: 10.1007/s11042-022-12421-1.
- [168] N. Perraudin, P. Balazs, and P. L. Søndergaard, "A fast griffin-lim algorithm," in *2013 IEEE Workshop on Applications of Signal Processing to Audio and Acoustics*, New Paltz, NY, USA: IEEE, Oct. 2013, pp. 1–4. DOI: 10.1109/WASPAA.2013.6701851.
- [169] G. T. Beauregard, X. Zhu, and L. Wyse, "An efficient algorithm for real-time spectrogram inversion," in *Proceedings of the 8th International Conference on Digital Audio Effects (DAFX-05)*, Madrid, Spain, Sep. 20, 2005, pp. 116–121.
- [170] X. Zhu, G. Beauregard, and L. Wyse, "Real-time iterative spectrum inversion with look-ahead," in *2006 IEEE International Conference on Multimedia and Expo*, Toronto, ON, Canada: IEEE, Jul. 2006, pp. 229–232. DOI: 10.1109/ICME.2006.262424.
- [171] M. Portnoff, "Magnitude-phase relationships for short-time fourier transforms based on gaussian analysis windows," in *ICASSP '79. IEEE International Conference on Acoustics, Speech, and Signal Processing*, vol. 4, Washington, DC, USA: Institute of Electrical and Electronics Engineers, 1979, pp. 186–189. DOI: 10.1109/ICASSP.1979.1170695.
- [172] S. Shimauchi, S. Kudo, Y. Koizumi, and K. Furuya, "On relationships between amplitude and phase of short-time fourier transform," in *2017 IEEE International Conference on Acoustics, Speech and Signal Processing (ICASSP)*, New Orleans, LA, USA: IEEE, Mar. 2017, pp. 676–680. DOI: 10.1109/ICASSP.2017.7952241.
- [173] Z. Prusa, P. Balazs, and P. L. Søndergaard, "A noniterative method for reconstruction of phase from STFT magnitude," *IEEE/ACM Transactions on Audio, Speech, and Language Processing*, vol. 25, no. 5, pp. 1154–1164, May 2017. DOI: 10.1109/TASLP.2017.2678166.
- [174] J. Williams, "Algorithm 232: Heapsort," *Communications of the ACM*, vol. 7, no. 6, pp. 347–348, Feb. 15, 1964. DOI: 10.1145/512274.512284.
- [175] Z. Prusa and P. L. Søndergaard, "Real-time spectrogram inversion using phase gradient heap integration," in *Proceedings of the 19th International Conference on Digital Audio Effects (DAFx-16)*, Brno, Czech Republic, Sep. 5, 2016, pp. 17–21.
- [176] R. Decorsière, P. L. Søndergaard, J. Buchholz, and T. Dau, "Modulation filtering using an optimization approach to spectrogram reconstruction," in *Proceedings of Forum Acusticum 2011*, Aalborg, Denmark: European Acoustics Association, Jul. 27, 2011.
- [177] R. Decorsiere, P. Søndergaard, E. MacDonald, and T. Dau, "Inversion of auditory spectrograms, traditional spectrograms, and other envelope representations," *IEEE/ACM Transactions on Audio, Speech, and Language Processing*, vol. 23, no. 1, pp. 46–56, 2015. DOI: 10.1109/TASLP.2014.2367821.
- [178] D. C. Liu and J. Nocedal, "On the limited memory BFGS method for large scale optimization," *Mathematical Programming*, vol. 45, no. 1, pp. 503–528, Aug. 1989. DOI: 10.1007/BF01589116.
- [179] I. Waldspurger, A. d'Aspremont, and S. Mallat, "Phase recovery, MaxCut and complex semidefinite programming," *Mathematical Programming*, vol. 149, no. 1, pp. 47–81, Feb. 2015. DOI: 10.1007/s10107-013-0738-9.
- [180] E. J. Candès, Y. C. Eldar, T. Strohmer, and V. Voroninski, "Phase retrieval via matrix completion," *SIAM Review*, vol. 57, no. 2, pp. 225–251, Jan. 2015. DOI: 10.1137/151005099.
- [181] D. L. Sun and J. O. Smith III, "Estimating a signal from a magnitude spectrogram via convex optimization," presented at the Audio Engineering Society Convention 133, Audio Engineering Society, Oct. 25, 2012, p. 8785.

- [182] R. Balan, "On signal reconstruction from its spectrogram," in *2010 44th Annual Conference on Information Sciences and Systems (CISS)*, Princeton, NJ, USA: IEEE, Mar. 2010, pp. 1–4. DOI: 10.1109/CISS.2010.5464828.
- [183] J. Bouvrie and T. Ezzat, "An incremental algorithm for signal reconstruction from short-time fourier transform magnitude," in *INTERSPEECH 2006 and 9th International Conference on Spoken Language Processing*, Pittsburgh, PA, USA: International Speech Communication Association (ISCA), Sep. 17, 2006, pp. 2510–2513. DOI: 10.21437/Interspeech.2006.
- [184] G. T. Beauregard, M. Harish, and L. Wyse, "Single pass spectrogram inversion," in *2015 IEEE International Conference on Digital Signal Processing (DSP)*, Singapore, Singapore: IEEE, Jul. 2015, pp. 427–431. DOI: 10.1109/ICDSP.2015.7251907.
- [185] J. Laroche and M. Dolson, "Phase-vocoder: About this phasiness business," in *Proceedings of 1997 Workshop on Applications of Signal Processing to Audio and Acoustics*, New Paltz, NY, USA: IEEE, 1997, p. 4. DOI: 10.1109/ASPAA.1997.625603.
- [186] M. Puckette, "Phase-locked vocoder," in *Proceedings of 1995 Workshop on Applications of Signal Processing to Audio and Acoustics*, New Paltz, NY, USA: IEEE, 1995, pp. 222–225. DOI: 10.1109/ASPAA.1995.482995.
- [187] M. Abe and J. O. Smith III, "Design criteria for the quadratically interpolated FFT method (i): Bias due to interpolation," Center for computer research in music and acoustics, Department of Music, Stanford University, Stanford, CA, USA, Technical Report STAN-M-114, Oct. 13, 2004.
- [188] P. Magron, R. Badeau, and B. David, "Phase reconstruction of spectrograms with linear unwrapping: Application to audio signal restoration," in *2015 23rd European Signal Processing Conference (EUSIPCO)*, Nice: IEEE, Aug. 2015, pp. 1–5. DOI: 10.1109/EUSIPCO.2015.7362333.
- [189] Y. C. Eldar, P. Sidorenko, D. G. Mixon, S. Barel, and O. Cohen, "Sparse phase retrieval from short-time fourier measurements," *IEEE Signal Processing Letters*, vol. 22, no. 5, pp. 638–642, May 2015. DOI: 10.1109/LSP.2014.2364225.
- [190] A. Oppenheim and J. Lim, "The importance of phase in signals," *Proceedings of the IEEE*, vol. 69, no. 5, pp. 529–541, 1981. DOI: 10.1109/PROC.1981.12022.
- [191] S. A. Rizzi, A. R. Aumann, L. V. Lopes, and C. L. Burley, "Auralization of hybrid wing–body aircraft flyover noise from system noise predictions," *Journal of Aircraft*, vol. 51, no. 6, pp. 1914–1926, Nov. 2014. DOI: 10.2514/1.C032572.
- [192] S. A. Rizzi and A. K. Sahai, "Auralization of air vehicle noise for community noise assessment," *CEAS Aeronautical Journal*, vol. 10, no. 1, pp. 313–334, Mar. 2019. DOI: 10.1007/s13272-019-00373-6.
- [193] S. A. Rizzi, I. LeGriffon, R. Pieren, and L. Bertsch, "A comparison of aircraft flyover auralizations by the aircraft noise simulation working group," in *AIAA AVIATION 2020 FORUM, VIRTUAL EVENT: American Institute of Aeronautics and Astronautics*, Jun. 15, 2020. DOI: 10.2514/6.2020-2582.
- [194] The pandas development team, *Pandas-dev/pandas: Pandas*, Jun. 28, 2023. DOI: 10.5281/zenodo.8092754.
- [195] DTU Wind Energy, *Wetb: Wind energy toolbox*, version 0.1.0, Feb. 15, 2022.
- [196] L. Paz, *Compress-pickle: Standard pickle, wrapped with standard compression libraries*, version 2.1.0, Sep. 21, 2021.
- [197] P. Vølund and S. M. Petersen, "Validation of aeroelastic model of nordtank 500/37," Risø National Laboratory, Roskilde, Denmark, Technical Report Risø-R-1006(EN), 1997.
- [198] U. S. Paulsen, "Verification of long-term load measurement technique: Work package 1b.2 under the european commission, integrated wind turbine design (UPWIND).," DTU, Risø National Laboratory for Sustainable Energy, Wind Energy Division, Roskilde, Denmark, Technical Report Risø-R-1782(EN), 2011.
- [199] F. Bertagnolio, H. Madsen, A. Fischer, and C. Bak, "Validation of an aero-acoustic wind turbine noise model using advanced noise source measurements of a 500kw turbine," presented at the 16th International Symposium on Transport Phenomena and Dynamics of Rotating Machinery, Apr. 10, 2016.

- [200] Danmarks Meteorologiske Institut. "Observationer," DMI. (2023), [Online]. Available: <http://www.dmi.dk/friedata/observationer/> (visited on Aug. 1, 2023).
- [201] G. F. Greco, R. Merino-Martínez, and A. Osses, *SQAT: A sound quality analysis toolbox for MATLAB*, version v1.0, May 14, 2023. DOI: 10.5281/ZENODO.7934709.
- [202] G. Felix Greco, R. Merino-Martínez, A. Osses, and S. Langer, "SQAT: A MATLAB-based toolbox for quantitative sound quality analysis," presented at the *Internoise 2023*, Chiba, Tokyo, Japan, Aug. 22, 2023.
- [203] A. Osses, G. F. Greco, and R. Merino-Martínez, "Considerations for the perceptual evaluation of steady-state and time-varying sounds using psychoacoustic metrics," presented at the *Forum Acusticum 2023*, Turin, Italy, Sep. 2023.
- [204] G. P. van den Berg, "Effects of the wind profile at night on wind turbine sound," *Journal of Sound and Vibration*, vol. 277, no. 4, pp. 955–970, Nov. 5, 2004. DOI: 10.1016/j.jsv.2003.09.050.
- [205] M. Cand, A. Bullmore, M. Smith, S. Von-Hunerbein, and R. Davis, "Wind turbine amplitude modulation: Research to improve understanding as to its cause & effect," in *Acoustics 2012*, S. F. d'Acoustique, Ed., Nantes, France, Apr. 2012.
- [206] C. Ioannidou, S. Santurette, and C.-H. Jeong, "Effect of modulation depth, frequency, and intermittence on wind turbine noise annoyance," *The Journal of the Acoustical Society of America*, vol. 139, no. 3, pp. 1241–1251, Mar. 1, 2016. DOI: 10.1121/1.4944570.
- [207] R. Makarewicz and R. Golebiewski, "The influence of a low level jet on the thumps generated by a wind turbine," *Renewable and Sustainable Energy Reviews*, vol. 104, pp. 337–342, Apr. 1, 2019. DOI: 10.1016/j.rser.2019.01.022.
- [208] G.-Q. Di, X.-W. Chen, K. Song, B. Zhou, and C.-M. Pei, "Improvement of zwicker's psychoacoustic annoyance model aiming at tonal noises," *Applied Acoustics*, vol. 105, pp. 164–170, Apr. 1, 2016. DOI: 10.1016/j.apacoust.2015.12.006.
- [209] P. Susini, S. McAdams, and S. Winsberg, "A multidimensional technique for sound quality assessment," *Acta Acustica united with Acustica*, vol. 85, no. 5, pp. 650–656, Sep. 1, 1999.
- [210] E. Parizet and V. N. Nosulenko, "Multi-dimensional listening test: Selection of sound descriptors and design of the experiment," *Noise Control Engineering Journal*, vol. 47, no. 6, p. 227, 1999. DOI: 10.3397/1.599319.
- [211] E. Parizet, N. Hamzaoui, and G. Sabatié, "Comparison of some listening test methods : A case study," *Acta Acustica united with Acustica*, 2005.
- [212] G. B. Rossi, F. Crenna, and M. Codda, "Measurement of quantities depending upon perception by jury-test methods," *Measurement*, vol. 34, no. 1, pp. 57–66, Jul. 2003. DOI: 10.1016/S0263-2241(03)00020-4.
- [213] M. A. Alamir, K. L. Hansen, B. Zajamsek, and P. Catcheside, "Subjective responses to wind farm noise: A review of laboratory listening test methods," *Renewable and Sustainable Energy Reviews*, vol. 114, p. 109317, Oct. 2019. DOI: 10.1016/j.rser.2019.109317.
- [214] R. Merino-Martínez, B. von den Hoff, and D. G. Simons, "Design and acoustic characterization of a psycho-acoustic listening facility," in *Proceedings of the 29th international congress on sound and vibration*, E. Carletti, Ed., Prague, Czech Republic: IIAV CZECH s.r.o., Jul. 9, 2023, pp. 274–281.
- [215] Sonova Consumer Hearing GmbH. "Sennheiser HD 559," Sennheiser. (2023), [Online]. Available: <https://www.sennheiser-hearing.com/en-BE/p/hd-559/> (visited on Jul. 26, 2023).
- [216] HP Development Company, L.P. "HP EliteBook 850 g1 notebook PC product specifications," HP Customer Support - Knowledge Base. (2023), [Online]. Available: <https://support.hp.com/us-en/product/hp-elitebook-850-g1-notebook-pc/5405368/document/c03963889> (visited on Jul. 26, 2023).
- [217] M. Virbel, G. Pettier, A. Arora, *et al.*, *Kivy: The open source python app development framework*, in collab. with I. Cassina, J. Bradley, N. Lécaudé, *et al.*, version 2.2.1, Jun. 17, 2023.
- [218] I. Boulet, A. Minard, N. Pellegrin, and P. Boussard, "Optimized tools and process for a better prediction of future aircraft noise perception," presented at the *Internoise 2023*, Chiba, Tokyo, Japan, Aug. 2023.

-
- [219] Delft University of Technology. "TU delft facts and figures." (Sep. 1, 2023), [Online]. Available: <https://www.tudelft.nl/en/about-tu-delft/facts-and-figures> (visited on Sep. 28, 2023).